Fall 2023

Shared Roots: A geochemical investigation of basaltic andesites to understand magmatic cogenesis at the Middle Sister and South Sister volcanoes, central Oregon

Sean Francis Halstead

Shared Roots:
A geochemical investigation of basaltic andesites to understand magmatic cogenesis at the Middle Sister and South Sister volcanoes, central Oregon

Sean Francis Halstead

Senior Thesis
Department of Geology
Western Washington University
Advisor: Dr. Mai Sas

June, 2023

SHARED ROOTS: A GEOCHEMICAL INVESTIGATION OF BASALTIC ANDESITES TO UNDERSTAND MAGMATIC COGENESIS AT THE MIDDLE SISTER AND SOUTH SISTER VOLCANOES, CENTRAL OREGON

Halstead, Sean Francis, Department of Geology, Western Washington University

Abstract

The Middle Sister and South Sister volcanoes, near Bend, Oregon, are overlapping, active Cascade Arc stratovolcanoes which share a complex, contemporaneous eruptive history. This history is characterized by an extreme compositional diversity of lavas erupted in alternating phases of high activity from one neighboring volcano to the other, with both vents producing material ranging from basaltic andesite to rhyolite. This system is understood to be predominantly fed by basaltic andesites fractionated from partial mantle melts within the lower crust, but magma compositions are additionally impacted by mixing, assimilation, and crustal contamination while in transit to the surface. Thus, the subterranean relationship between these volcanoes is, at present, poorly understood, with relatively little work having been done to identify and constrain the extent of reservoir interconnectivity and magma sharing which may influence eruptive behaviors in the past and inform understandings of present-day activity.

Here, we investigate chemical zoning in minerals from three basaltic andesite lavas–two from Middle Sister and one from South Sister–as a record of magmatic interactions impacting the more primitive, mafic material supplied to each vent. By identifying and correlating similar mineral populations found in each lava, we identify interactions between three discrete magmatic components, recorded as distinctive chemical bands in plagioclase, olivine, and pyroxene phenocrysts. Two of these magmatic components are observed in all three units of study, shown to represent consistent recharge of basaltic andesite magma via a two-part mixing process during the interval from 48 ka to 21 ka. At Middle Sister, the studied basaltic andesites are interpreted as chemically consistent eruptions of this two-part hybrid magma from 48 ka to 22 ka. At South Sister, mineral zones record a mixing event between a similar hybrid magma and a third, chemically distinct magmatic component, suggestive of independent processes and discrete crustal reservoirs beneath Middle Sister and South Sister around 22 to 21 ka. Future work is proposed to investigate the origins of each of these components via trace element analysis and thermobarometry, in order to assess the similarities and differences in melt sourcing, magma transit, and crustal contamination at Middle Sister and South Sister.

Acknowledgements

The Three Sisters Volcanic Complex is a facet of the traditional lands of the Molalla and the Confederated Tribes of Warm Springs, to whom the Three Sisters are known as “Klah Klahnee” or “Three Points.” Any and all present-day research in the region is indebted to the long-standing stewardship and observation of the landscape by its traditional inhabitants. Additionally, Western Washington University occupies the lands and waters of the Lummi Nation and the Nooksack Tribe, who have called the Salish Sea and North Cascades watershed home since time immemorial. This investigation represents a western scientific perspective on the history of the land, which does not encompass its whole history.

This research is possible thanks to the support of the WWU Pilot Project Grant, the Central Oregon Geoscience Society Student Research Grant, the Jack Kleinman Memorial Fund for Volcano Research, the WWU Research and Sponsored Programs Grant, the WWU Geology Department Advance for Research, and the Mount Baker Rock and Gem Club Geology Student Scholarship. Finally, I would like to extend my heartfelt gratitude to my advisor Dr. Mai Sas, as well as Dr. Nathan Andersen and Dr. Michael Kraft, whose mentorship, guidance, and hard work have enabled me to realize this project to its fullest potential.

Table of Contents

1: Introduction

Investigating magmatic processes and understanding magma storage conditions plays an important role in identifying potential volcanic hazards. In order to improve forecasting of eruptive behavior at a given volcano, there must exist a thorough basis of research interpreting and deciphering the mantle and crustal processes impacting the associated magmatic system. Although volcanic complexes do exhibit a certain degree of natural variability which inherently clouds precise predictions of future eruptions, our ability to accurately and quantitatively forecast volcanic behaviors is equally impeded by uncertainty in our understanding of how any one volcanic system functions and evolves, creating potential for certain volcanic behaviors and processes to go overlooked (Marzocchi *et al.,* 2021). For this reason, petrological studies investigating past magmatism play a crucial role in interpreting the history and evolution of a volcanic system. Although such studies may not directly relate to present-day hazards, they nonetheless serve as important building blocks in refining our understanding of these important and complex systems.

This study takes a petrologic approach to interpreting past magmatism at the Middle Sister and South Sister volcanoes, located in central Oregon. Not only do these neighboring stratovolcanoes stand out in their extreme compositional variance, but they are also largely contemporaneous with one another, alternating in activity for much of their shared eruptive history (Hildreth, 2007; Hildreth *et al.,* 2012). This raises a number of key questions regarding the magmatic system beneath them, each leading into the next: what processes govern the diverse compositional outputs observed at each vent? Have magma sources changed and evolved over the course of known magmatic activity? Do components such as liquids, cumulates, and wall rocks mix within the crust, resulting in hybrid magmas? Are the main vents fed by shared or discrete magma reservoirs? How might this inform our present-day interpretations of more recent signs of magmatic activity? As of yet, the web of interrelationships governing these volcanoes has not been disentangled; thus, any meaningful interpretation of present-day activity is greatly served by investigations into the magmatic background of past eruptions.

Importantly, recent workers (e.g., Wicks *et al.,* 2002) have detected semiregular, episodic uplift events ~6 km west of the South Sister summit, beginning in 1998 and continuing to this day. These inflation episodes are interpreted as periodic pulses of fresh magma intruding into the upper crust at depths of ~7 km (Riddick and Schmidt, 2011; Lisowski *et al.,* 2021), with a United States Geological Survey (USGS) information statement issued in January 2022 describing an increase in rates of uplift between late 2021 and early 2022 (Major, 2022). Although an eruption in the near future is deemed unlikely, the inflation observed near South Sister has renewed public attention regarding the Three Sisters region, illustrating that the peaks–although quiescent–are far from dormant, with a magmatic system that is changing in real time. This illustrates the need for more detailed work which focuses on discrete eruptive episodes within the region's volcanic history.

At present, the area has been well mapped by Hildreth and others (2012), and the broad eruptive histories of Middle Sister and South Sister have been described by Calvert and others (2018) and Fierstein and others (2011), respectively. Furthermore, Parker and others (2023) expand systematic interpretations based on trends in whole rock data for all three Sisters, with an

emphasis on the evolution of the system's more silicic products. With regards to mineral-specific investigations, several studies have attempted to disentangle the magmatic origins of dacites and rhyolites at South Sister through crystal zoning histories (e.g., Brophy and Dreher, 2000; Stelten and Cooper, 2012; Waters *et al.*, 2021), but few focus explicitly on mafic products from South Sister. At present, little detailed mineral work has been published for Middle Sister. Thus, detailed petrologic studies of mineral chemistry at Middle Sister and South Sister are, at the time of writing, far from comprehensive and few investigations use crystal zoning to examine potential reservoir connectivity between them.

This contribution seeks to provide meaningful, comparative interpretations of crystal evidence recording magmatic conditions beneath Middle Sister and South Sister for three basaltic andesite lavas–two from Middle Sister and one from South Sister. By conducting parallel, in-depth comparative studies of strategically chosen eruptions, we aim to piece together a more robust understanding of the genetic relationships that underpin the joint magmatic history of the Middle Sister and South Sister volcanoes. Through analysis of textural and chemical indicators preserved within mineral populations, we describe the relationships between these lavas and speculate as to the subterranean processes that may explain their formation. This work aims to serve as a starting point for further investigation into melt origins, magmatic interactions, and compositional alterations for some of the mafic end-member products of these historically complex volcanoes.

2: Background

2.1: Geologic Setting

2.1.1: Geographic Context

The Three Sisters Volcanic Complex (TSVC) is an extensive system of volcanic vents making up a 20-km reach of the Oregon Cascades. It is presently dominated by three contiguous, neighboring stratovolcanoes, known as North Sister, Middle Sister, and South Sister, along with the far older Broken Top stratovolcano and numerous smaller, peripheral vents (Hildreth *et al.*, 2012). Located approximately 35 km west of Bend, Oregon, the TSVC occupies the traditional lands of the Molalla and the Confederated Tribes of Warm Springs. This location lies at the intersection of several complex tectonic and magmatic regimes, leading to an incredible diversity of volcanic products within the region.

2.1.2: Tectonomagmatic Regime

Most notably, the TSVC is part of the Cascade Arc, resulting from the roughly 30–45 mm/yr convergence of the Juan de Fuca Plate with continental North America (Wilson, 2002). The Cascadia subduction complex represents a relatively young, hot, and buoyant end member among subduction zones worldwide, with sub-arc slab ages of approximately 17–16 Ma beneath the Sisters Reach (Green and Harry, 1999). Consequently, volatile contents in Cascade magmas are relatively low, with the majority of slab dehydration taking place before reaching sub-arc depths (Ruscitto *et al.*, 2010). Northwards motion of the neighboring Pacific Plate means the downgoing Juan de Fuca slab is underthrust oblique to the arc at a relatively shallow dip, resulting in strong

basal traction with the overriding North American Plate (Hildreth *et al.*, 2012). Additionally, along the southern margin of the Cascades, proximity to the slab edge promotes rollback, resulting in mantle buoyancy and extension in the adjacent back-arc region. These factors culminate in an overall clockwise rotation of the forearc block by as much as 2.0°/Ma (Wells and McCaffrey, 2013). This block rotation (*Figure 1*) is accommodated inboard of the arc by compression within the Yakima Fold Belt of southern Washington, and the pronounced crustal extension of the Basin and Range Province of the American Southwest (Hammond, 1979).

The Basin and Range Province covers an area of ~1 million km² stretching from Arizona to Oregon, and is characterized by crustal thinning and associated upwelling of hot mantle material (Eaton, 1982). Its northwestern margin (occupying southeastern Oregon) comprises a region known as the High Lava Plains, one of the largest intraplate magmatic systems on Earth (Eagar *et al.*, 2011). Magmatism at the High Lava Plains exhibits a distinctive bimodal distribution of independent pulses of basalts and high-silica rhyolites, with the onset of the latter propagating in a time-dependent westerly path (*Figure 1*) from Harney Basin–well within the back-arc–towards the Sisters Reach of the Oregon Cascades over the last ~10 Ma (Jordan *et al.*, 2004; Ford *et al.*, 2013). Although interpretations of this trend vary, the favored explanation holds that the westerly progression of rhyolites is attributable to the progressive steepening of the Juan de Fuca slab in concert with trench rollback, shifting the locus of upwelling brought on by counterflow in the mantle wedge closer and closer to the arc (Long *et al.*, 2012). Generation of crustal melts in the region would be strongly enhanced by the local regime of crustal thinning; furthermore, exceptionally high Poisson's ratios measured in the closing region between the advancing rhyolitic front and the Sisters Reach potentially support the presence of such melts within the crust (Eagar *et al.*, 2011). Given that the crustal melting anomaly of the High Lava Plains appears to be penetrating the Cascade Arc directly beneath the Sisters Reach, it can be speculated that recent magmatism at the TSVC may be additionally influenced by enhanced crustal melting, potentially impacting the compositions and origins of its younger eruptive products (Hildreth *et al.*, 2012).

Within the central Oregon Cascades, the location of the active volcanic front has migrated eastwards from the Western Cascades (active from ~40 - 10 Ma) to the High Cascades (~10 Ma to recent), as the rotation of the forearc block continually shifts arc crust westward relative to a fixed melt source parallel to the trench (Hammond, 1979; Taylor, 1990). The High Cascades occupy a large graben that is bounded by arc-parallel normal faults (See *Figure 1*) which result from intra-arc extension (Taylor, 1978). Consequently, subsidence of the High Cascades block allows deep-sourced mafic magmas to penetrate to the surface, partially filling the basin and giving rise to unusually high rates of true basaltic volcanism (Taylor, 1978, 1990; Hughes and Taylor, 1986). Relative to arcs worldwide, the Central Oregon Cascades exhibit a uniquely high density of Quaternary volcanic activity, with thousands of small monogenetic mafic vents producing a diverse range of near-primary basalts–unusual in arc settings (Hughes and Taylor, 1986; Schmidt *et al.*, 2008). Considering the complex tectonic regime which governs magmatism at the TSVC, the tremendous diversity observed in its eruptive products is hardly surprising.

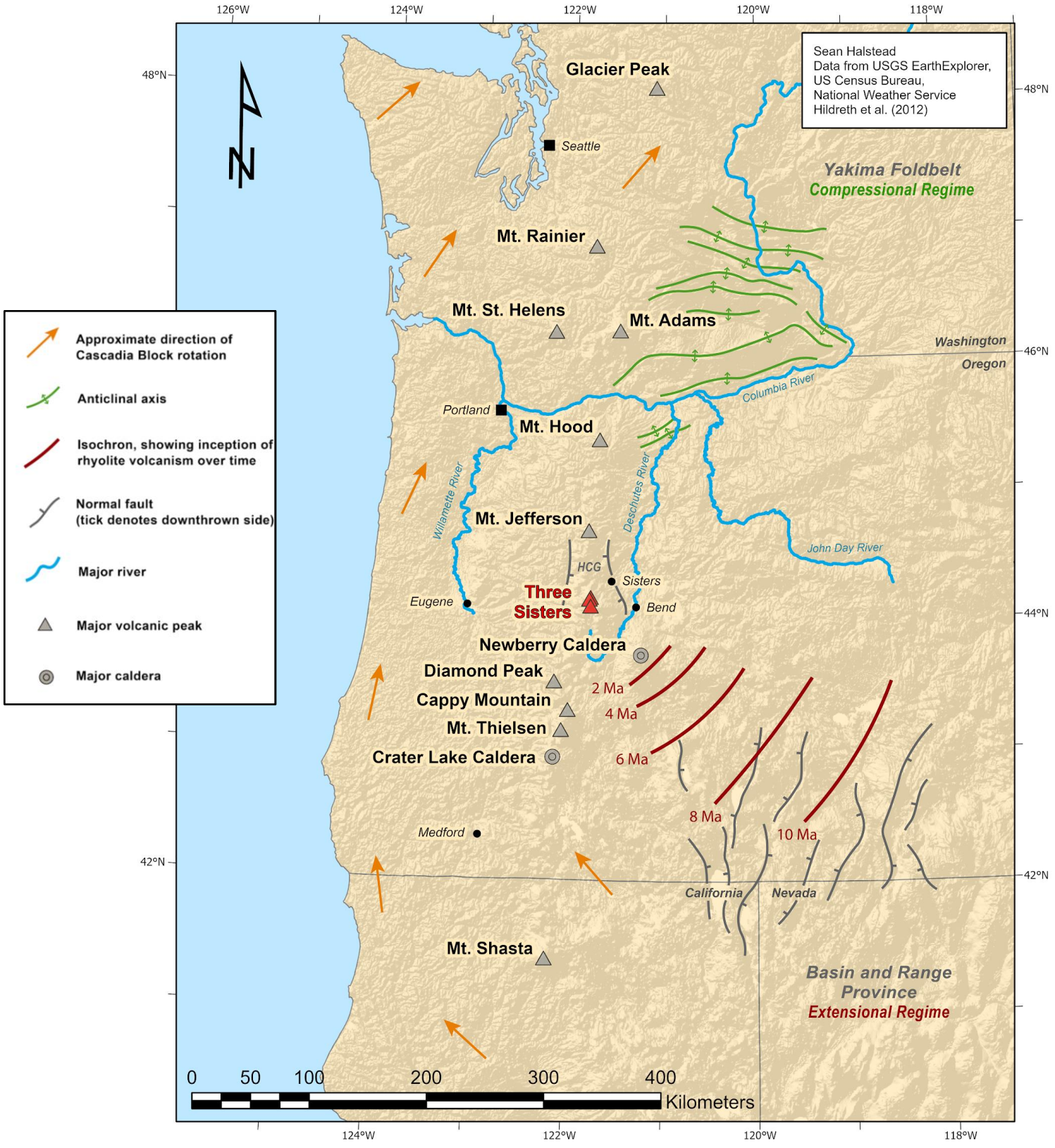

Figure 1: Map of the Oregon Cascades and adjacent reaches, illustrating the impacts of clockwise rotation of the Cascadia Block on regional tectonics and volcanic activity. Rotation is compensated for by compression in the Yakima Foldbelt and the extension of the NW Basin and Range Province, leading to the age-progressive genesis of the High Lava Plains rhyolites towards the Sisters Reach. Note the position of the Three Sisters within the High Cascades Graben (HCG), a subsided and infilled region of the present-day arc–a product of the very same tectonic forces.

2.2: Eruptive History

2.2.1: Early Stages

The TSVC has a long and dynamic history, encompassing volcanic activity spanning the full compositional spectrum typical of arc volcanoes. Even so, the eruptive history of the Three Sisters has only been established relatively recently. Early expeditions to the region by Hodge (1925) laid the fundamental groundwork for future study, but incorrectly concluded that the peaks were the eroded remains of a single far older, far larger edifice. Later expeditions continued to refine the progression of eruptive activity, establishing a pattern of exclusively mafic volcanism throughout the low-lying periphery, with more evolved silicic lavas only erupting at discrete point sources to build towering intermediate to silicic stratovolcanoes (Williams, 1944). Peripheral mafic vents far outnumber the larger shield volcanoes and stratovolcanoes, giving rise to a relatively poorly defined volcanic front, and many such vents share a conspicuous north-south alignment reflective of the local stress field (Hildreth, 2007; Hildreth *et al.*, 2012). This "mafic periphery" observed by early workers has since been attributed to the subsidence of the High Cascades Graben, as discussed above. On the whole, these lavas predate the more evolved volcanic centers which make up the main peaks, comprising a landscape of monogenetic basalt and basaltic andesite lava flows and scoria cones, as well as a scattering of longer-lived mafic shield volcanoes (Hildreth, 2007; Hildreth *et al.*, 2012).

Although peripheral activity has continued throughout the history of the TSVC, construction of the main stratovolcanoes of the reach encompass the vast majority of intermediate to silicic volcanism, producing 30–40 km^3 of compositionally diverse eruptive products (Sherrod *et al.*, 2004; Hildreth, 2007). Older studies have consistently tended to overestimate the ages of the major peaks, which have only relatively recently been correlated through more advanced geochronology techniques by Hildreth and others (2012). Evidence of more evolved volcanism within the TSVC begins with the construction of the Broken Top Volcano in the Middle Pleistocene. It was active from 300 ka - 150 ka, erupting primarily basaltic andesites alongside a handful of andesite, dacite, and rhyodacite domes and lava flows which represent the oldest intermediate to silicic eruptive products at the TSVC (Taylor, 1978, 1990; Sherrod *et al.*, 2004).

Following Broken Top, North Sister is the oldest of the Three Sisters, constructed in four primary eruptive stages between 120 ka and 45 ka, although today its edifice is heavily eroded (Schmidt and Grunder, 2009; Hildreth *et al.*, 2012). Genetically speaking, it is understood to be closer related to the magmas of the mafic periphery than those found at either of its sisters, with compositions restricted to a remarkably monotonous suite of basaltic andesites (Hildreth *et al.*, 2012). Petrologic studies by Schmidt and Grunder (2011) suggest that North Sister magmas were consistently fed via two-part mixing of low-K tholeiites (typical, mantle-derived primary arc melts) with partial melts derived from mafic crustal rocks deep beneath the arc, suggesting a relatively simple, stable magmatic system for the duration of its construction. Although relevant to a broader understanding of the TSVC, North Sister is not the focus of this investigation. Middle Sister and South Sister, by contrast, bear relatively little resemblance to their older sibling.

2.2.2: Building the Foundations of Middle Sister and South Sister (51 ka - 27 ka)

South Sister produced the earliest discernable lavas, yielding several early rhyolite domes (now mostly covered by younger flows) between approximately 51 ka and 45 ka (Fierstein *et al.*, 2011). At roughly the same time, Middle Sister saw its first identifiable eruption (the basaltic andesite of North Fork Whychus Creek; unit mnf), a series of lava flows dated to ~48 ka, closely correlating with the waning of activity at North Sister. During the ensuing 12,000 years, Middle Sister experienced an initial eruptive pulse ranging from basaltic andesites to rhyolite, concluding at ~37 ka (Calvert *et al.,* 2018).

Just as Middle Sister lapsed into a state of temporary inactivity, South Sister began an intense phase of silicic eruptions. From 37 ka to 30 ka, South Sister produced numerous, volumetrically predominant rhyolite domes and flows, while several subordinate dacite and andesite flows periodically draped the accumulating summit cone. During this period, activity was predominantly centered around the central vent area, with only four small rhyolite domes developing around the periphery (Fierstein *et al.*, 2011). Then, at ~30 ka, South Sister experienced a violent, explosive eruption producing a thick layer of andesite fallout; at this point, activity on the peak intensified, producing a series of progressively intermediate lava flows (initially dacites, tapering into andesites) from the central vent area, which spread radially from the summit and into the peripheral apron until 27 ka (Fierstein *et al.*, 2011).

2.2.3: Shifting Activity from South Sister to Middle Sister (27 ka - 22 ka)

The sequence of radial construction on the South Sister apron from 30 ka - 27 ka was closely followed by a period of rapid construction of a more steeply-dipping summit cone of andesite agglutinates, forming a 700 m wide central crater near the present-day Hodge Crest (Fierstein *et al.*, 2011, Hildreth *et al.*, 2012). Meanwhile, a variety of peripheral eruptions, spanning the full compositional range of the peak, erupted about its flanks (Fierstein *et al.*, 2011). During this time, the shift in activity back towards Middle Sister continued. At ~26 ka, two silicic lavas erupted from within the saddle between Middle Sister and South Sister (Calvert *et al.*, 2018). Soon thereafter, a series of lavas erupted from the eastern and western flanks of Middle Sister from 25–22 ka; predominantly andesites, with a scattering of dacites and basaltic andesites (Calvert *et al.*, 2018). Meanwhile, South Sister exhibited one final summit-building pulse. Several focused eruptions of dacite lava filled the original summit crater, constructing a higher summit with a new, smaller crater located ~400 m west of the original from 25 ka - 22 ka. The final eruption from the South Sister summit complex produced the basaltic andesite of Teardrop Pool (unit mtp) at ~22 ka, the only mafic material to have erupted from the South Sister central vent throughout its entire history (Fierstein *et al.*, 2011, Hildreth *et al.*, 2012).

2.2.4: Final Middle Sister Eruptive Pulse (22 - 15 ka) and Beyond

During the final, dacite-dominated summit sequence at South Sister, Middle Sister began a stark compositional transition, which would ultimately produce the predominant cone-building lavas which make up much of the present-day edifice (Calvert *et al.*, 2018). While earlier (25 - 22

ka) lavas were dominated by andesites, Middle Sister began erupting an extensive suite of exclusively dacites and basaltic andesites from 22 ka until the conclusion of the summit building sequence at ~14.5 ka (Hildreth *et al.*, 2012, Calvert *et al.*, 2018). Among these was the basaltic andesite north of Hayden Glacier (unit mnh). Erupted at ~21 ka and roughly coeval with mtp, this lava flow was quickly buried by successive flows (Hildreth *et al.*, 2012). Much of the current Middle Sister edifice is covered in a single, voluminous eruption of thin basaltic andesite flows, with an age constrained to ~20.5 ka. Finally, a handful of dacite flows overtopped and capped the edifice, completing the final summit sequence at Middle Sister (Calvert *et al.*, 2018).

Although two small rhyolite flows erupted from the apron of South Sister around 2.2 - 2.0 ka, the main summit vents have been inactive since then (Fierstein *et al.*, 2011). However, the TSVC itself is far from dormant, as the mafic periphery has produced numerous lava flows, scoria cones, and shield volcanoes in recent (post-glacial) time (Hildreth, 2007; Hildreth et al., 2012). Furthermore, the uplift detected by Wicks and others (2002) suggests that new magma is actively intruding within the crust, although the likelihood of an eruption at this location remains relatively low (Lisowski *et al.*, 2021). Nevertheless, the TSVC has shown itself to be a complex and highly varied system, with a magmatic regime that is still evolving to this day.

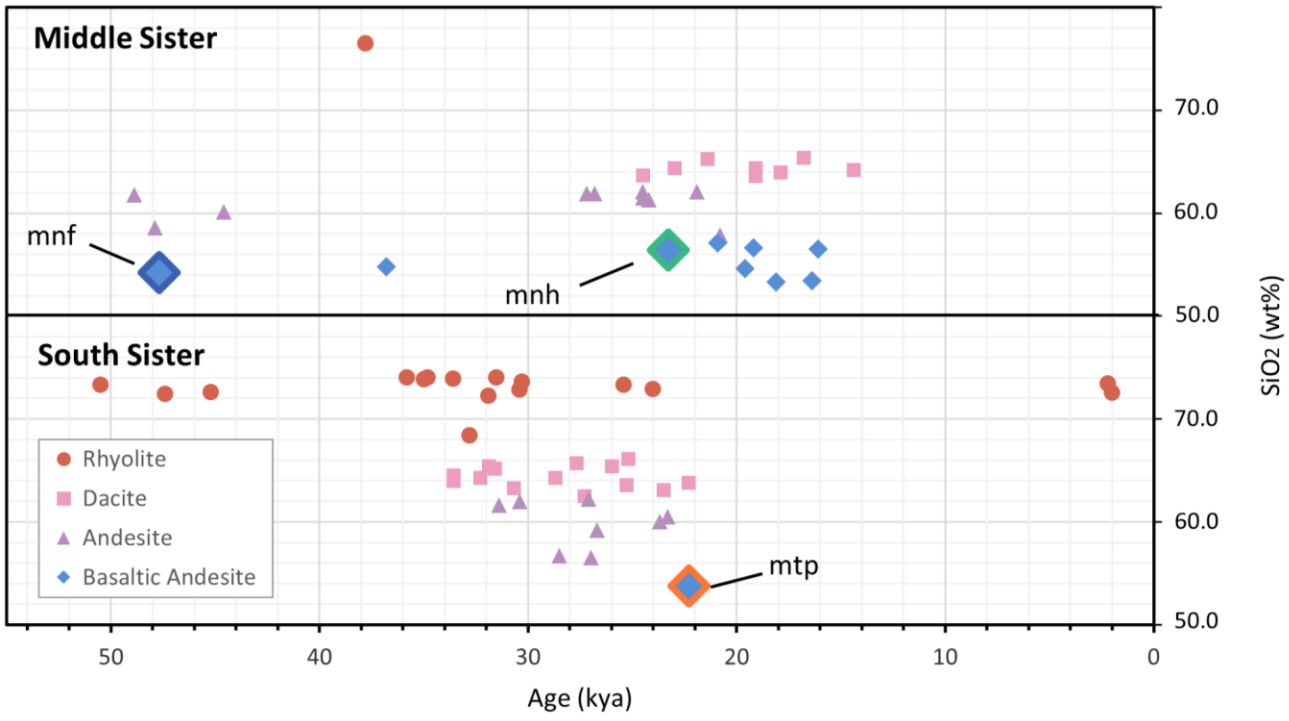

Figure 2: Timeline of eruptive activity at the Middle Sister and South Sister volcanoes. Eruptive products range from mafic to felsic, with both volcanoes producing basaltic andesites (blue diamonds), andesites (purple triangles), dacites (pink squares), and rhyolites (red circles) at some point in their eruptive history. Units of interest to this investigation are labeled, enlarged, and highlighted. Unit mnf (blue) erupted early during Middle Sister's first constructive phase, unit mnh (green) erupted at the beginning of Middle Sister's final, bimodal summit-building pulse, and coeval unit mtp (orange) erupted at the very conclusion of South Sister's main constructive episode.

2.3: Units of Interest and Investigative Approach

This study aims to interpret and understand magmatic processes impacting the final stages in the period of shifting activity between Middle Sister and South Sister, focusing on units mnf and mnh from Middle Sister, and unit mtp from South Sister (*Figure 3*). These represent three compositionally similar landmark eruptions which each mark a key turning point in the behavior of the volcanic system between 48 ka and 21 ka.

Unit mnf erupted from near the Middle Sister central vent, although the exact location of its source has since been buried. This stack of at least ten thin, similar lava flows presently outcrops roughly 2 km southeast of the Middle Sister summit, and is dated to 47.7±9.5 ka with a bulk silica content of 53.6–54.4% SiO_2 (Hildreth *et al.*, 2012). This mafic eruption marks the first known eruption from the Middle Sister central vent complex, and is overlain by a series of andesites (Calvert *et al.*, 2018). Both compositionally and temporally, this eruption also coincides well with the final stages of waning activity on North Sister.

Unit mnh erupted near the saddle between Middle and North Sisters at 20.9±5.5 ka (Hildreth *et al.*, 2012). Today, glacial erosion and accumulation of talus has obscured much of the unit, which only outcrops at two small cliff faces. It is a stack of eight thin, separate glassy to devitrified lava flows, the youngest of which was used to produce the $^{40}Ar/^{39}Ar$ date provided by Hildreth and others (2012). With the exception of the fifth exposed flow, which outcrops along the upper edge of the lower exposure, these are compositionally identical, with a bulk silica content of 53.4–54.4% SiO_2 (Hildreth *et al.*, 2012). These flows are among the first in the bimodal series of basaltic andesites and dacites which make up the latter half of the summit- building stage on Middle Sister, a notable deviation from the preceding intermediate, andesite- dominated activity (Calvert *et al.*, 2018). As such, mnh marks an important turning point in the eruptive history of Middle Sister. Additionally, it is noted by Hildreth and others (2012) to be compositionally identical to unit mnf, although separated by nearly 30,000 years.

Unit mtp is a welded agglutinate and scoria-fall deposit which drapes the peak of South Sister about its prominent summit crater, with one lobe dipping southwards to an elevation of roughly 2800 m. It has been dated by Hildreth and others (2012) to 22.3±12.9 ka, with a bulk silica content of 53.8–56.1% SiO_2. As such, this lava represents the only known mafic unit to have erupted from the South Sister edifice throughout its entire history (Hildreth *et al.*, 2012). Given its distinct composition and temporal significance as the final product from South Sister's main central vent, mtp presents a valuable opportunity to gain insight into the processes impacting the conclusion of the primary summit cone-building sequence at the volcano.

Thus, studying units mnf, mnh, and mtp in conjunction presents an opportunity to investigate the extent of any reservoir interconnectivity or magmatic cogenesis within Middle Sister from 48–21 ka, as well as between Middle Sister and South Sister during the period from 22–21 ka. This study provides a snapshot into primitive material erupted at both volcanoes, granting an opportunity to study their magmatic roots as well as any shallower reservoir processes which may impact magmatic pathways to the surface.

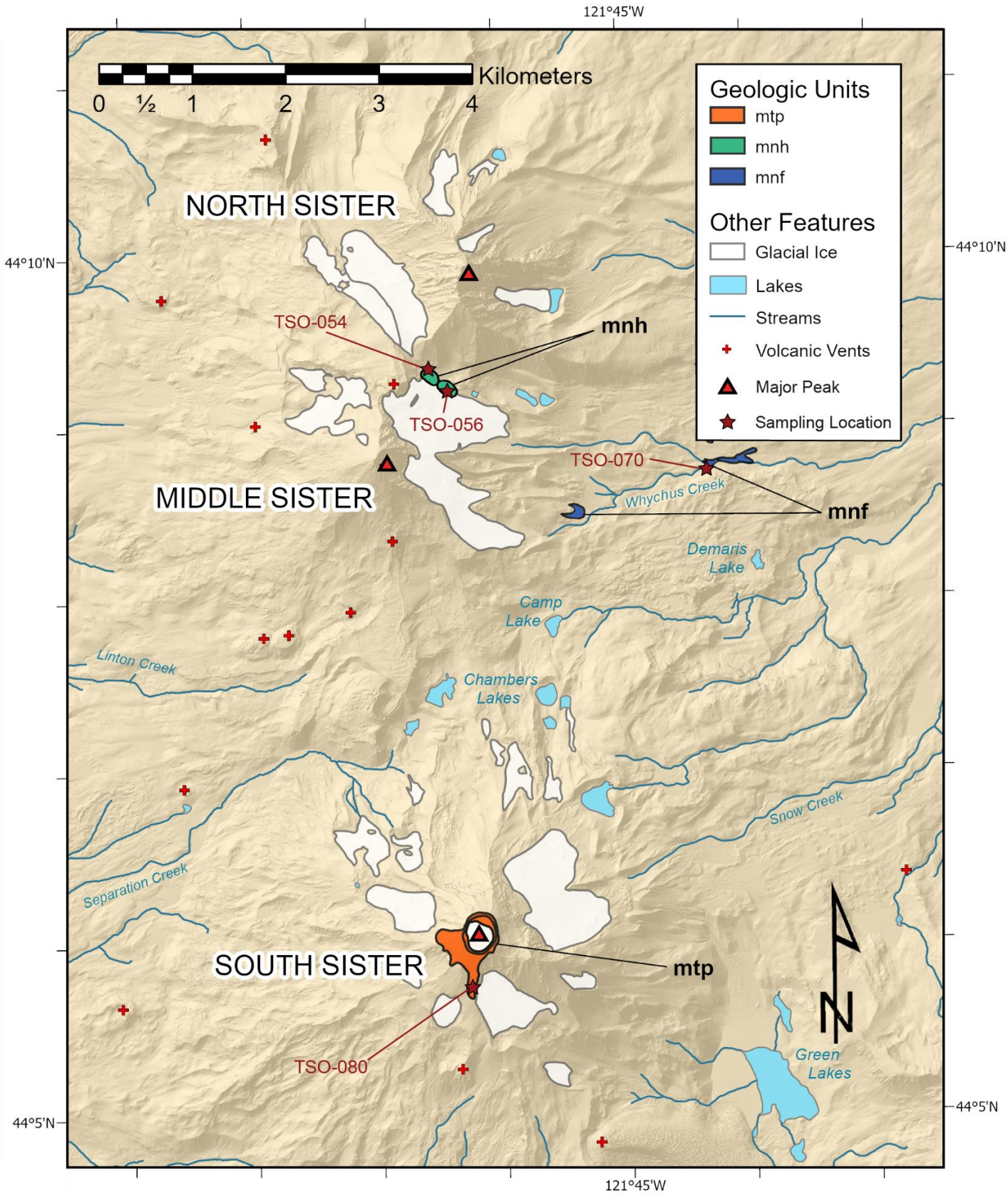

Figure 3: Map of the study area, highlighting the locations of each of the units sampled. The basaltic andesite north of Hayden Glacier (unit mnh) sits just below Black Hump in the saddle between North Sister and Middle Sister, the basaltic andesite of North Fork Whychus Creek (unit mnf) outcrops primarily along the banks of its namesake, and the basaltic andesite of Teardrop Pool (unit mtp) caps the South Sister Summit. Sampling locations are marked with red stars. Note the conspicuous north-south alignment of certain vent complexes, indicative of the local stress field.

3: Methods

3.1: Petrography

Units of interest were selected based on whole rock compositions, $^{40}Ar/^{39}Ar$ ages, and inferred eruption from the main conduit by Hildreth and others (2012). For more information on field methods, sample selection/preparation, and outcrop and hand sample descriptions, see *Appendix 1: Field Notes and Analytical Preparations*. Following sample collection, thin and thick sections were prepared for each unit of interest and examined using a Leica DM750P petrographic microscope. Thin sections were employed to make detailed petrographic observations regarding mineral identities, distributions, and textures. Additional thin sections were prepared for select sub-flows of unit mnh and varying suites of mtp fallout debris in order to compare petrography across different stages of each eruption, and the most representative and least weathered material of each unit was selected to serve as the sample (thick section) to be used for chemical analysis. The thick sections were compared against petrographic observations for their associated thin section to ensure consistency.

3.2: Whole Rock Analysis

Whole rock analyses were performed in two batches due to delayed sample collection of unit mtp. The first batch included mnf and mnh samples TSO-054.1b, TSO-056b, and TSO-070b (collected for this investigation) as well as sample TS-217 (collected by Hildreth et al., 2012). These were analyzed by the Hamilton Analytical Lab at Hamilton College following their standard analytical procedure, using a combination of X-ray fluorescence (XRF) and laser ablation inductively coupled plasma mass spectrometry (LA-ICP-MS). XRF was conducted on homogenized and double-fused glass disks. First, samples were ground to a ~3.5 gm powder in a steel chipmunk with a Rocklabs tungsten carbide ring mill, then combined in a 2:1 ratio with a Li-tetraborate flux (Merck Spectromelt A-10) in a vortex mixer. This mixture was fused in a Mersen grade UF-4S graphite crucible at 1000°C, then cleaned, re-ground, and re-fused under the same procedure. After a final diamond lap flattening and ethanol rinse, XRF analysis was conducted on the disks using the Thermo ARL Perform'X spectrometer at an accelerating voltage of 45 kV and a current of 45 mA. The instrument is recalibrated roughly every 10 months using a suite of ~70 reference standards, and an international standard was run alongside samples and independently validated by the Hamilton lab. Small chips roughly 3 mm by 8 mm were cut from the XRF disks and mounted in epoxy, then polished in 1 µm steps to be used for laser ablation analysis. This was done via the Photon Machines Analyte 193 (G1) ablation station at 7 Hz with a spot size of 150 μm^2, and data collection was conducted on the Varian 820 ICP-MS system, following the detailed methods of Conrey *et al.*, (2019). An in-house 2:1 Li-tet glass drift monitor was analyzed 15–20 times, alternately with sample tracks and reference materials to ensure a stable signal, and signal processing and drift correction were calculated using the Iolite (Paton *et al.*, 2011) and HALite (Conrey *et al.*, 2023) software packages.

The second batch of whole rock analyses included mtp samples TSO-080 (collected for this study), and TS-47 and TS-48 (collected by Hildreth *et al.*, 2012). This was performed by the

Washington State University GeoAnalytical Lab, using a similar combined XRF and ICP-MS approach. XRF analysis followed the detailed sample preparation and analytical procedures of Johnson and others (1999), with analyses being performed on 2:1 Li-tetraborate fused beads by the Rigaku 3370 XRF Spectrometer, operating at an accelerating voltage of 50 kV and a current of 50 mA. ICP-MS analyses were conducted on mixed-acid digested samples, rather than laser-ablated solid samples. After powdering, samples were mixed with an equal part Spectromelt A10 di-Lithium-tetraborate flux, then fused, reground, and dissolved using a high-purity reagent mix of HNO_3 (69–70%), HF (48–52%), $HClO_4$ (67–71%), and H_2O_2. Liquid ICP-MS analyses were performed using an Agilent model 7700 ICP-MS, with drift correction being done using internal Ru, In, and Re standards.

3.3: Scanning Electron Microscopy (SEM)

Electron microscopy was conducted using the TESCAN Vega 3 Thermionic SEM, located at Western Washington University. The instrument was operated at an accelerating voltage of 20 kV to collect back-scattered electron (BSE) images of target crystals using the instrument's built-in Yttrium-Aluminum Garnet (YAG) type backscatter detector, operating with a nitrogen atmosphere at a Univac pressure of 20 Pa on an uncoated sample. While operating under medium vacuum does reduce data and image quality, it allowed for carbon-coating to be done later, aiding with petrography and ensuring that the resultant coating was consistent with the calibration of the electron microprobe, discussed below. Preliminary BSE imaging was employed to identify mineral phases, select ideal crystals for chemical analysis, and make broad-scale observations on crystal zoning, in preparation for future quantitative analysis.

Additionally, electron-dispersive spectroscopy (EDS) was employed using an Oxford Instruments X-Max silicon-drift 80 mm^2 EDS detector to obtain semi-quantitative chemical data for select crystals. Specifically, EDS data were employed to distinguish orthopyroxene and clinopyroxene prior to quantitative chemical analysis. After samples had been carbon coated and underwent quantitative analysis on the electron microprobe, target crystals were re-imaged using the same SEM-BSE, this time operating at high vacuum to produce high-quality images.

3.4: Electron Microprobe Analysis (EMPA)

After ideal crystals were selected for analysis, quantitative chemical data for select major and minor elements were collected using the Cameca SX-100 electron microprobe, located at Oregon State University. Carbon coating was done in-house at OSU prior to analysis to ensure consistency with the analytical standards used for calibration. Plagioclase analyses were conducted at an accelerating voltage of 15 kV, a beam current of 30 nA, and a spot size of 5 μm, targeting the following elements (with the specified collection time in parentheses): Na (10 s), Mg (60 s), Si (10 s), Al (10 s), K (30 s), Ca (10 s), Ti (30 s), and Fe (60 s). Olivine analyses operated at an accelerating voltage of 15 kV, a beam current of 50 nA, and a spot size of 1 μm; analysis targeted the following: Si (10 s), Al (60 s), Mg (10 s), Na (30 s), Cr (60 s), Ni (60 s), Fe (10 s), Mn (20 s), and Ca (60 s). Orthopyroxene and clinopyroxene analyses were conducted under the same

instrument procedure, then recalculated separately on the basis of stoichiometry. Pyroxene analyses operated at an accelerating voltage of 15 kV, a beam current of 30 nA, and a spot size of 1 µm, targeting Si (10 s), Al (30 s), K (30 s), Mn (30 s), Fe (20 s), Na (20 s), Mg (20 s), Ti (30 s), Cr (30 s), and Ca (30 s).

Instrument calibration was compared against standards available from the Smithsonian microbeam standards collection. Plagioclase calibration was compared against the NMNH 115900 labradorite standard (Stewart *et al*. 1966, Jarosewich *et al.* 1980), olivine calibration was compared against the USNM 2566 Springwater olivine standard (Jarosewich *et al.* 1980), and pyroxene calibration was compared against the NMNH 122142 Kakanui augite standard (Jarosewich *et al.* 1980, Mason 1966, Mason and Allen 1973). For a detailed comparison of accepted and reported standards data, see *Supplementary Data* under *Appendix 2: EMPA Standards Calibration*. During data processing, any analyses with an oxide total <98.00% or >102.00% were rejected from consideration. In cases where low-concentration elements were measured as a negative value, the individual datum was rejected and the oxide total for that data point was recalculated with the errant value considered as zero.

4: Results

4.1: Petrographic Observations

Outcrop-scale observations (*Figure 4*) prove generally consistent with the descriptions of Hildreth and others (2012). Detailed field notes including outcrop descriptions and sampling locations, as well as in-depth hand sample descriptions, selection criteria, and observed internal variations between redundant samples at each location can be found in *Appendix 1*. Petrographically, each unit of interest exhibits mineral distributions consistent with basaltic andesites, with certain important deviations between one another, summarized below.

4.1.1: Unit mnf

The basaltic andesite of North Fork Whychus Creek contains uncommon irregular, jagged-edged vesicles (2%; up to 2 mm in length) within a fine, holocrystalline groundmass. Groundmass crystals are predominantly microlitic, needle-like plagioclase (~80%; <50 µm) oriented in a weakly directional fabric alongside abundant, equant to square oxide flecks (~4%; <10 µm) and minor anhedral olivine and pyroxene grains (<1%; <50 µm). The remaining ~13% comprises phenocrysts, mostly solitary, ranging from 0.1 to 1.5 mm in diameter. Occasional monomineralic plagioclase clots range up to 2 mm. Smaller clots containing olivine, plagioclase, and occasional heavily reacting pyroxenes are present, albeit rare.

Plagioclase represents 9% of the sample, ranging in length from 0.1 to 1.5 mm. Smaller phenocrysts are euhedral to subhedral, elongate laths, and larger phenocrysts have a subhedral, boxy habit. Plagioclase phenocrysts typically exhibit complex polysynthetic twinning and occasional pericline twinning. Roughly 60% (normalized) of mnf plagioclase phenocrysts have unzoned to patchy zoned cores bearing occasional moderate, coarse sieving, thick, unsieved, oscillatory-zoned mantles, and thin, unsieved rims. The remaining ~40% of phenocrystic

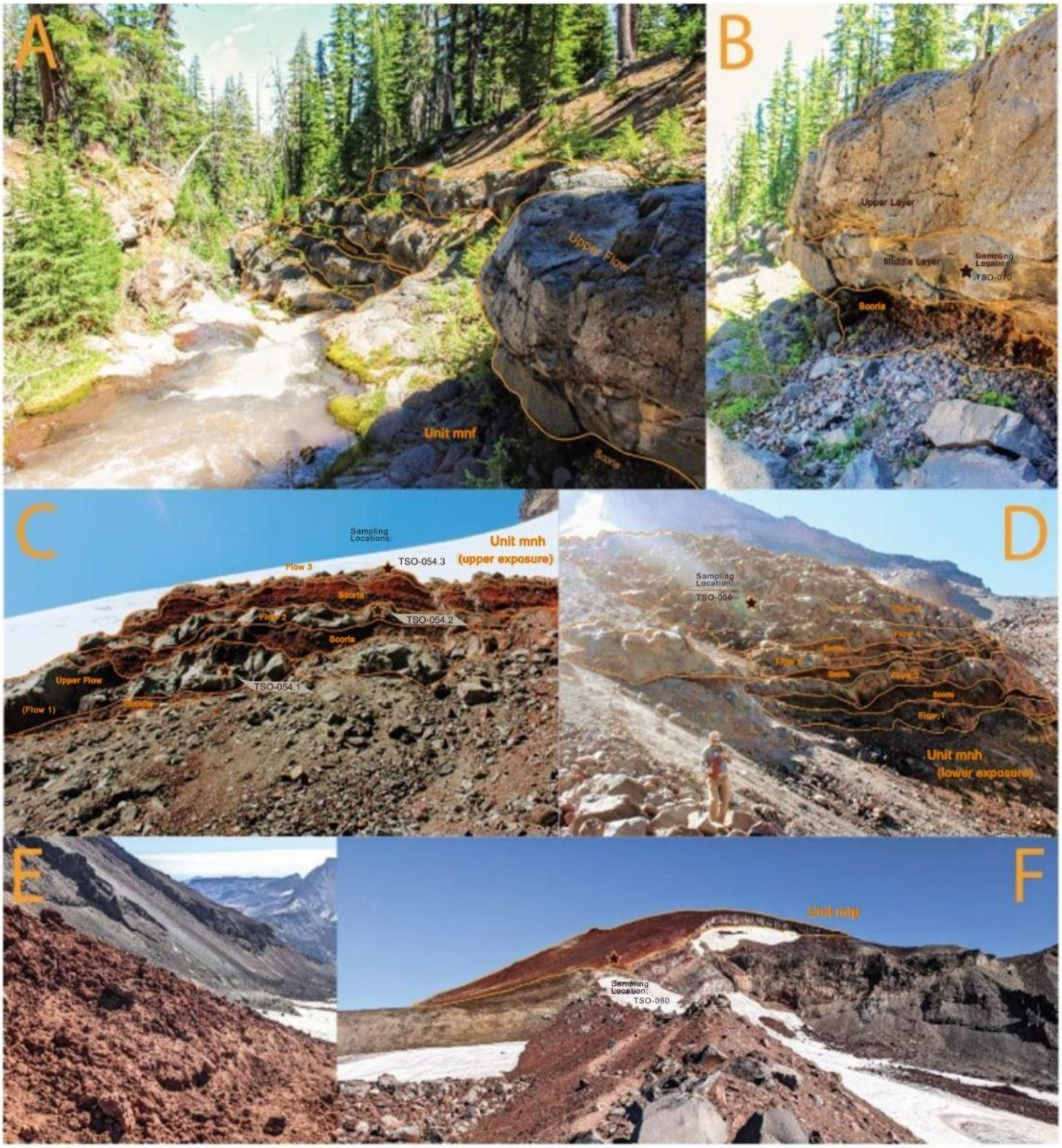

Figure 4: Field photos of relevant outcrops with star icons indicating sampling locations. **A)** Terraced canyon of unit mnf, illustrating stratigraphy of successive flows underlain by scoria deposits. **B)** Sampling site for mnf (TSO-070), showing three distinct layers of the uppermost flow. **C)** Upper exposure of unit mnh showing three separate, scoria-bounded flows: the uppermost being highly weathered, the middle flow being thin and moderately vesicular, and the lowermost (TSO-054.1) being vesicle-free and dense. **D)** lower exposure of mnh, showing four similar, thin flows (flow 4: TSO-056) overlain by a thicker, blocky flow (flow 5: chemically distinct). **E)** Representative fallout from near mtp (TSO-080) collection site. **F)** Unit mtp, capping the South Sister summit.

plagioclase have large, homogeneous core zones typically bearing pervasive fine sieving, followed by a thin, normal-zoned rim. Clinopyroxene is rare (<<1%), ranging up to 0.3 mm in diameter. Clinopyroxene phenocrysts are subhedral, heavily embayed, and elongate columnar in habit. These exhibit occasional simple polysynthetic twinning, and are typically found as solitary crystals. Orthopyroxene is uncommon (~1%), ranging up to 0.5 mm in diameter. Orthopyroxene phenocrysts have a columnar prismatic habit and highly embayed exteriors. Some orthopyroxene crystals are uncommonly seen reacting into clinopyroxene from the rim inwards. Others occasionally contain small relict olivine cores, reacting into irregular and highly resorbed orthopyroxene. Unreacted olivine is more abundant (3%), ranging from 0.1 to 0.6 mm. Olivine phenocrysts are euhedral to subhedral, equant hexagonal or granular, lightly fractured and untwinned. Roughly half of mnf olivine crystals are normally zoned, while the remainder are indistinct to reversely zoned. Olivine is found commonly as solitary crystals, in olivine-dominated clots, or clotted with plagioclase. Some larger olivine phenocrysts are also seen overgrowing and fully or partially enclosing smaller (~0.1 mm) plagioclase.

4.1.2: Unit mnh

Although mineralogically similar, different sampled flows of mnh bear differing groundmass textures, vesicularity, and crystallinity (*Appendix 1*); the following describes sample TSO-054.1, selected as the most broadly representative mnh sample. Unit mnh contains scant, rounded vesicles (~1%; up to 1.2 mm in diameter) within a very finely microcrystalline groundmass. Groundmass crystals are predominantly microlitic plagioclase laths (~60%; <20 µm), along with abundant, anhedral olivine (~15%; ~10 µm) and miniscule flecks of Fe-Ti oxides (14%; ~10 µm). The remaining ~10% comprises phenocrysts in a seriate distribution ranging from 0.1 to 2.4 mm. Complex, multi-mineralic clots are found up to 2.0 mm across, containing predominantly plagioclase with subordinate olivine. Additionally, the unit contains rare clots that range up to 5.5 mm in diameter, which resemble mafic cumulate material. These clots are dominated by exceptionally large olivine (up to 2.4 mm each) with small interstitial plagioclase.

Plagioclase phenocrysts represent approximately 8% of the sample, ranging in length from 0.1 to 2.0 mm. Smaller crystals are euhedral, elongate laths and larger crystals exhibit a subhedral, boxy to stubby habit. Plagioclase phenocrysts exhibit complex polysynthetic to pericline twinning, and are normally zoned with a thick core region, a subtly curved resorption surface, and a thinner, distinct rim. Crystal cores range from unsieved to finely sieved. Roughly 30% of mnh plagioclase crystals exhibit an additional mantle zone before the rim, representing abrupt normal step-zoning, often with very fine oscillations appearing in mantles and rims. These step-zoned crystals often have an additional, separate ring of fine sieving just before the rim. Olivine is found occasionally (~2%) and in two distinct populations. Roughly 70% of olivine phenocrysts are larger (0.5–1.2 mm), typically equant, euhedral to subhedral, and untwinned. These larger phenocrysts are normally zoned, appearing either as solitary crystals or in large cumulate clots, and occasionally overgrowing and enclosing small plagioclase laths. The remaining 30% are smaller (0.1 to 0.4

mm) anhedral to subhedral and highly fractured crystals with indistinct zoning, typically observed solo or in clots dominated by plagioclase.

4.1.3: Unit mtp

Unit mtp is far more complex. The chosen sample, TSO-080, is highly vesicular, with irregular vesicles representing ~30% by volume, ranging from 0.05 mm rounded bubbles to 4.8 mm irregular, elongate vesicles. Some vesicles are mantled or filled with secondary and/or accessory minerals. The groundmass is finely microcrystalline, comprising abundant microlitic plagioclase laths (40%; 20–80 µm), common, tiny flecks of Fe-Ti oxides (10%; ~10 µm), and occasional equant, anhedral fragments of olivine and clinopyroxene (3%; ~30 µm). It bears roughly 16% phenocrysts in a seriate distribution with no discernable grain arrangement. Complex crystal clots are abundant, containing combinations of all minerals present. Most clots comprise primarily plagioclase, although some are olivine- or pyroxene-dominated. Clots dominated by ferromagnesian minerals contain interstitial glass which is absent elsewhere in the sample.

Plagioclase phenocrysts make up roughly 12% of the sample, ranging from 0.1 to 3.0 mm in length. These vary from elongate, euhedral laths to boxy, subhedral crystals, sometimes with complex composite morphologies. Twinning ranges from occasional simple twinning to complex polysynthetic or pericline twinning. Plagioclase textures fall into two distinctive categories alongside a high proportion of miscellaneous textures: roughly 30% of mtp plagioclase phenocrysts exhibit simple normal zoning from a homogeneous, occasionally sieved core to a thin, stable rim. Another 30% of plagioclase phenocrysts feature a patchy to normal-zoned, coarsely sieved core followed by a prominent, curved, and abrupt resorption surface, then a final mantle and rim zone with gradational normal zoning. The remaining ~40% of mtp plagioclase phenocrysts exhibit miscellaneous, highly variable textures ranging from patchy-zoned in cores with thick oscillatory rims to extensively sieved and indistinctly zoned. Olivine is found occasionally (~2%), with phenocrysts ranging from 0.2 to 0.5 mm in diameter. These are typically equant, subhedral, phenocrysts bearing common melt inclusions and occasionally found overgrowing small plagioclase laths. Clinopyroxene phenocrysts are uncommon (~1%), ranging from 0.1 to 0.6 mm in length. Clinopyroxene phenocrysts are subhedral to anhedral and elongate columnar in habit, with common simple polysynthetic twinning. Roughly half of mtp clinopyroxene phenocrysts exhibit normal zoning with a resorbed core and a distinct rim, while the remainder are indistinctly zoned in thin section. Some clinopyroxene phenocrysts bear large oxide inclusions, and clot alongside orthopyroxenes and plagioclase in some clots. Orthopyroxene crystals are similarly uncommon (~1%), ranging from 0.1–0.5 mm in diameter. These are boxy to columnar, euhedral to subhedral crystals that lack twinning or evident zoning. Larger orthopyroxene phenocrysts are sometimes found reacting into an irregular mantle of clinopyroxene, and they commonly clot alongside plagioclase and clinopyroxene.

4.2: Bulk Rock Geochemistry

Complete whole rock data can be found in *Appendix 3: Bulk Chemical Data* (see *Supplementary Data*). In addition to bulk data collected by Hildreth and others (2012), independently collected bulk chemical data are used to illustrate general relationships between related units of study, using a combination of new samples gathered for this investigation as well as re-analyses of select original samples from Hildreth and others (2012). Generally, new whole rock findings agree with the data of Hildreth and others (2012). Unit mnf contains 53.8–54.6 wt% SiO_2 with FeO = 7.2–7.7 wt%, Al_2O_3 = 18.3–19.2 wt %, MgO = 4.6–5.6 wt% (Mg# = molar Mg/(Mg+Fe*0.85) = 57–60), CaO = 8.6–8.8 wt%, MnO = 0.12–0.13 wt %, TiO_2 = 1.0–1.1 wt%, P_2O_5 = 0.2–0.3 wt%, K_2O = 0.7–0.8 wt%, and Na_2O = 3.2–3.9 wt% (*Figure 5*). Notably, one mnh sample (TS-217)–collected by Hildreth and others from the uppermost flow of the lower mnh exposure (flow 5; *Figure 4D*)–is compositionally distinct from the other adjacent mnh flows, although too small to be mapped as its own unit. By silica content, this outlier plots within the compositional range of an andesite (*Figure 6*), following both the original whole rock dataset of Hildreth and others (2012) and this investigation's re-analysis of the same sample. As such, this outlier is not fully representative of mnh bulk chemistry and is not included in detailed whole-rock descriptions. The majority of mnh bulk analyses, however, plot identically to mnf, ranging from 53.3 to 54.6 wt% SiO_2 with FeO = 7.4–7.7 wt%, Al_2O_3 = 18.2–19.0 wt%, MgO = 5.1–5.5 wt%

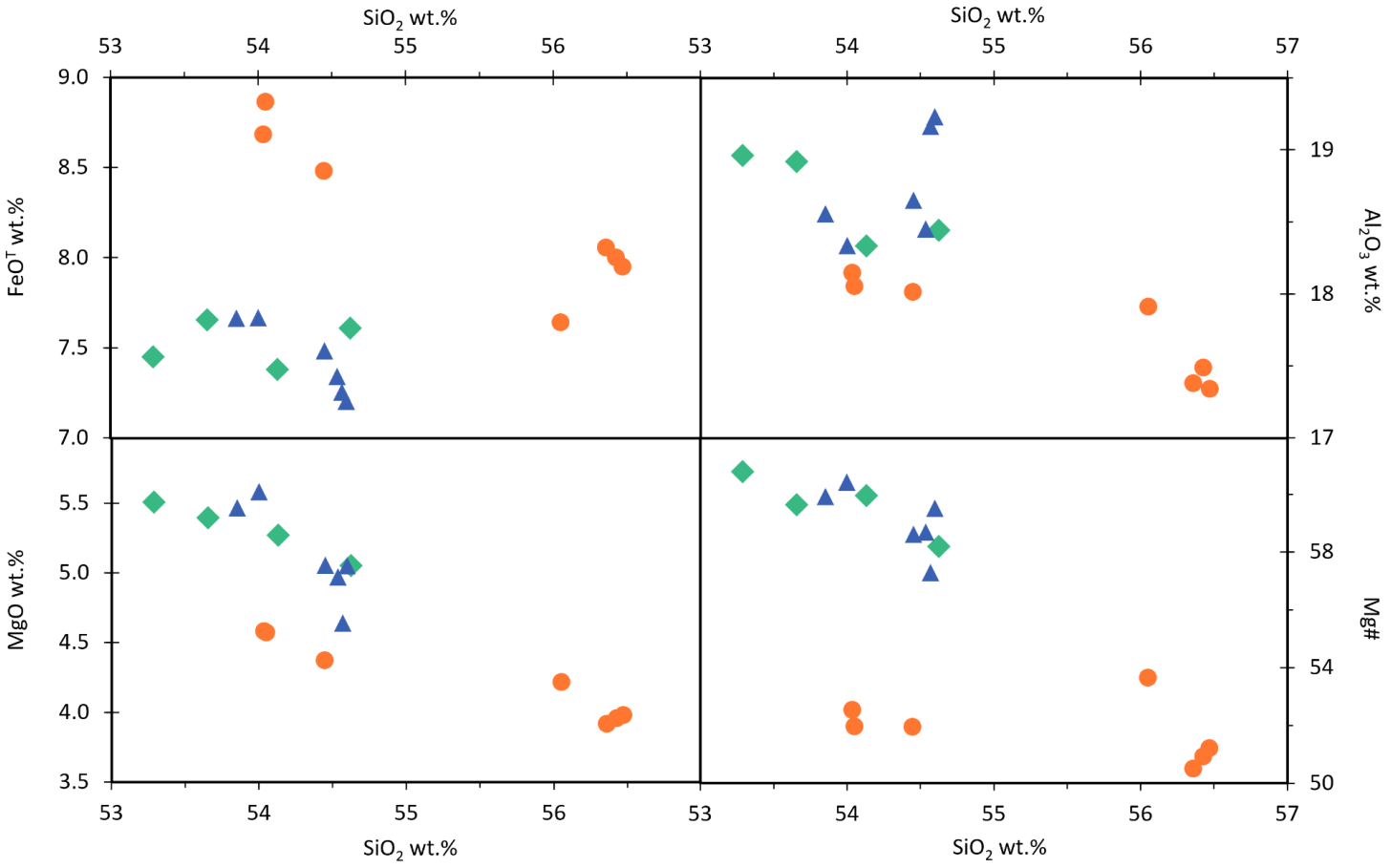

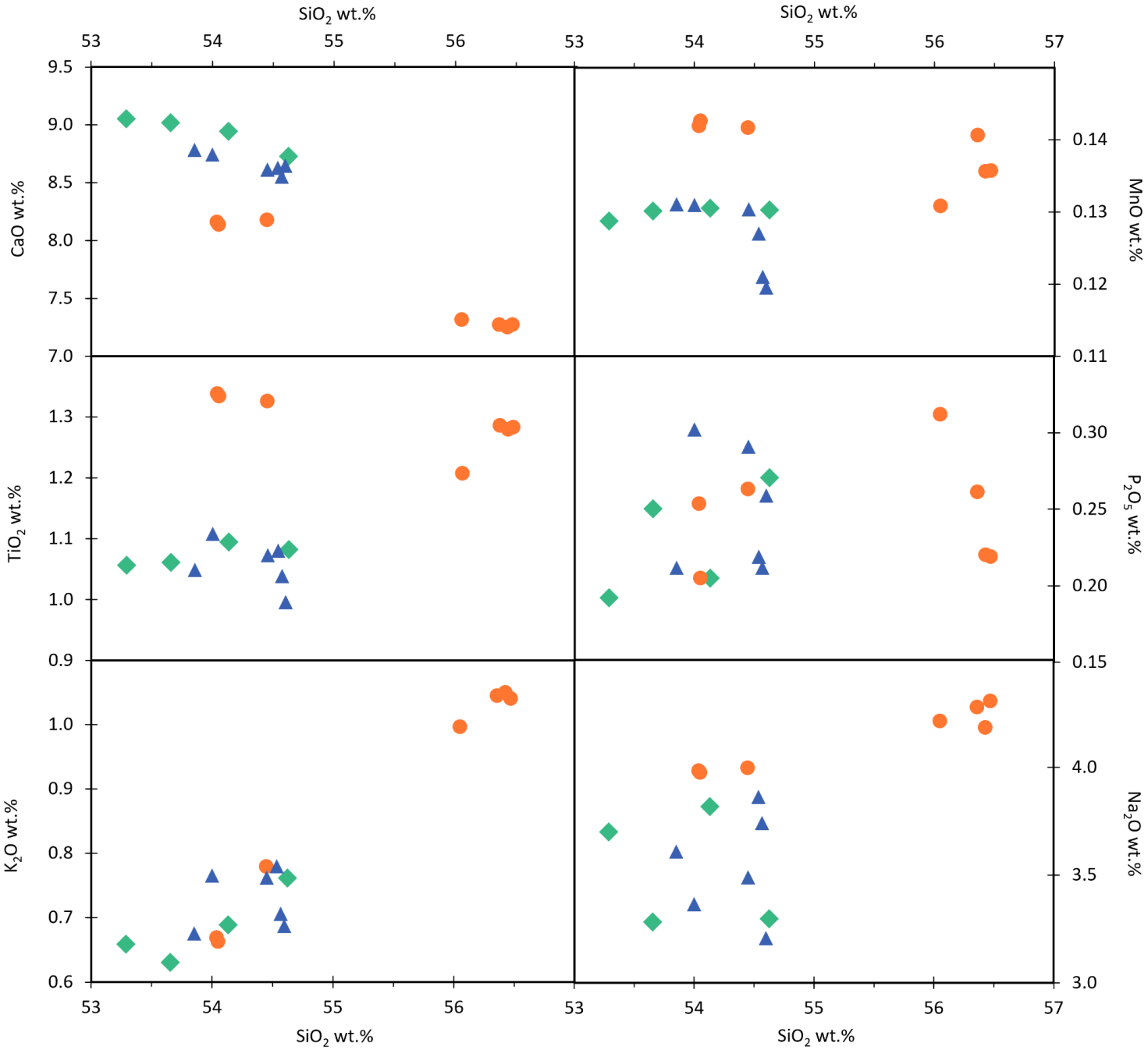

Figure 5 (this page and previous page): Harker diagrams illustrating compositional trends in whole rock chemical data. Units of interest to this investigation are marked with larger symbols and solid colors (mnh: teal diamonds, mnf: blue triangles, mtp; orange circles; includes data from Hildreth *et al.*, 2012). Note the depletion trend in Fe, Al, Mg, Ca, Mn, Ti, and P at increasing silica contents, while incompatible elements K and Na become enriched as compositions evolve. Units mnf and mnh are nearly compositionally identical, while mtp is distinctly enriched or depleted in certain elements relative to mnf and mnh.

(Mg# = 58–61), CaO = 8.7–9.1 wt%, MnO = 0.13 wt%, TiO_2 = 1.1 wt%, P_2O_5 = 0.2–0.3 wt%, K_2O = 0.6–0.8 wt%, and Na_2O = 3.3–3.8 wt% (*Figure 5*).

Finally, unit mtp plots in two distinct compositional clusters: the first ranges from 54.0 to 54.5 wt% SiO_2 with FeO = 8.5–8.9 wt%, Al_2O_3 = 18.0–18.2 wt%, MgO = 4.4–4.6 wt% (Mg# = 52–53), CaO = 8.1–8.2 wt%, MnO = 0.14 wt%, TiO_2 = 1.3 wt%, P_2O_5 = 0.2–0.3 wt%, K_2O = 0.7–0.8 wt%, and Na_2O = 4.0 wt%. The second cluster ranges from 56 to 56.5 wt% SiO_2 with FeO = 7.6–8.1 wt%, Al_2O_3 = 17.3–17.9 wt%, MgO = 3.9–4.2 wt% (Mg# = 50–54), CaO = 7.3 wt%, MnO = 0.13–0.14, TiO_2 = 1.2–1.3 wt%, P_2O_5 = 0.2–0.3 wt%, K_2O = 1.0–1.1 wt%, and Na_2O = 4.2–4.3 wt%. Although the lower-SiO_2 group overlaps with the range of silica contents for units mnf and mnh, unit mtp is distinctly higher in FeO, MnO, and TiO_2 and lower in CaO and Mg# relative to mnh and mnf at similar silica contents (*Figure 5*).

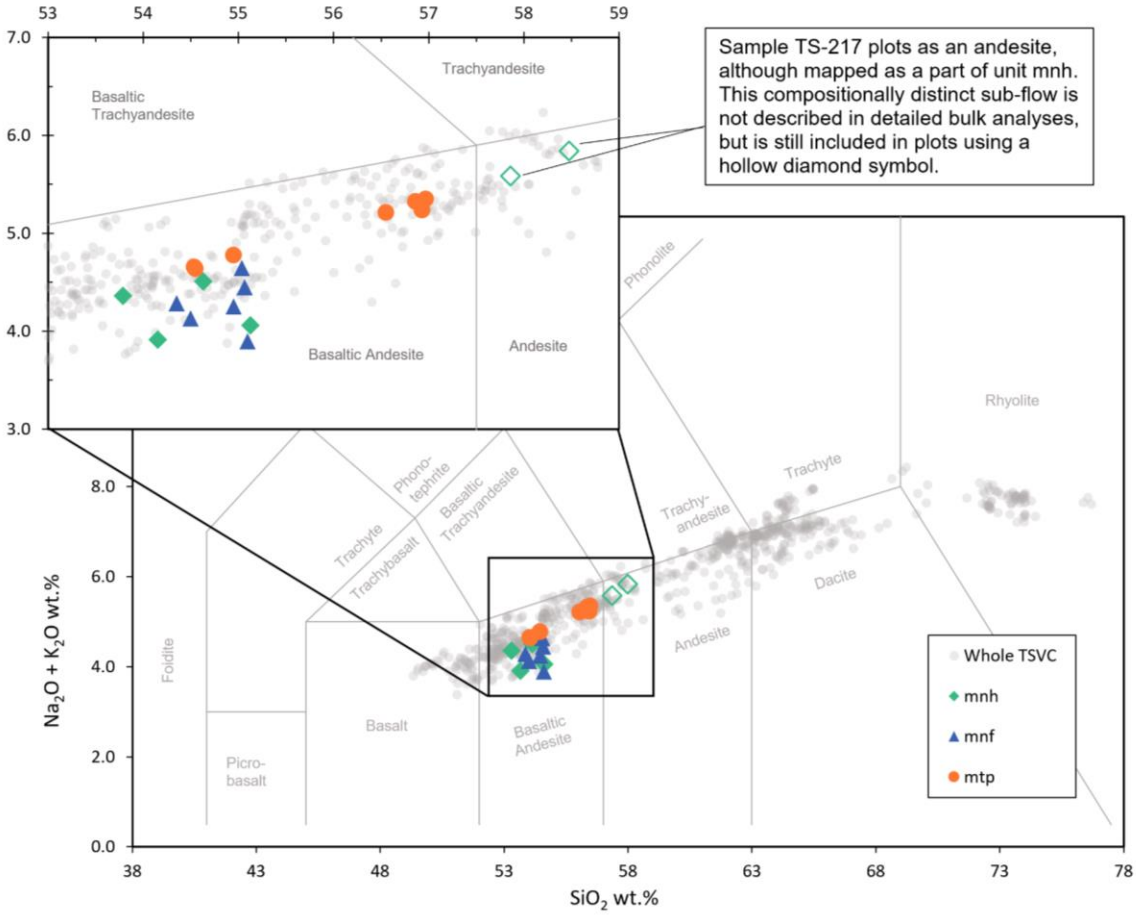

Figure 6: Total alkali-silica (TAS) diagram for TSVC eruptive products, illustrating a general enrichment in alkali elements at increasing SiO_2 across the TSVC. Symbology for main units of interest follows *Figure 5*, with the addition of grey circles indicating whole rock data for all analyses by Hildreth *et al.* (2012). As noted, one sub-flow of unit mnh (sample TS-217, marked with hollow teal diamonds) is chemically distinct and is not considered representative of unit mnh. Thus, these analyses are not considered in further whole rock interpretations.

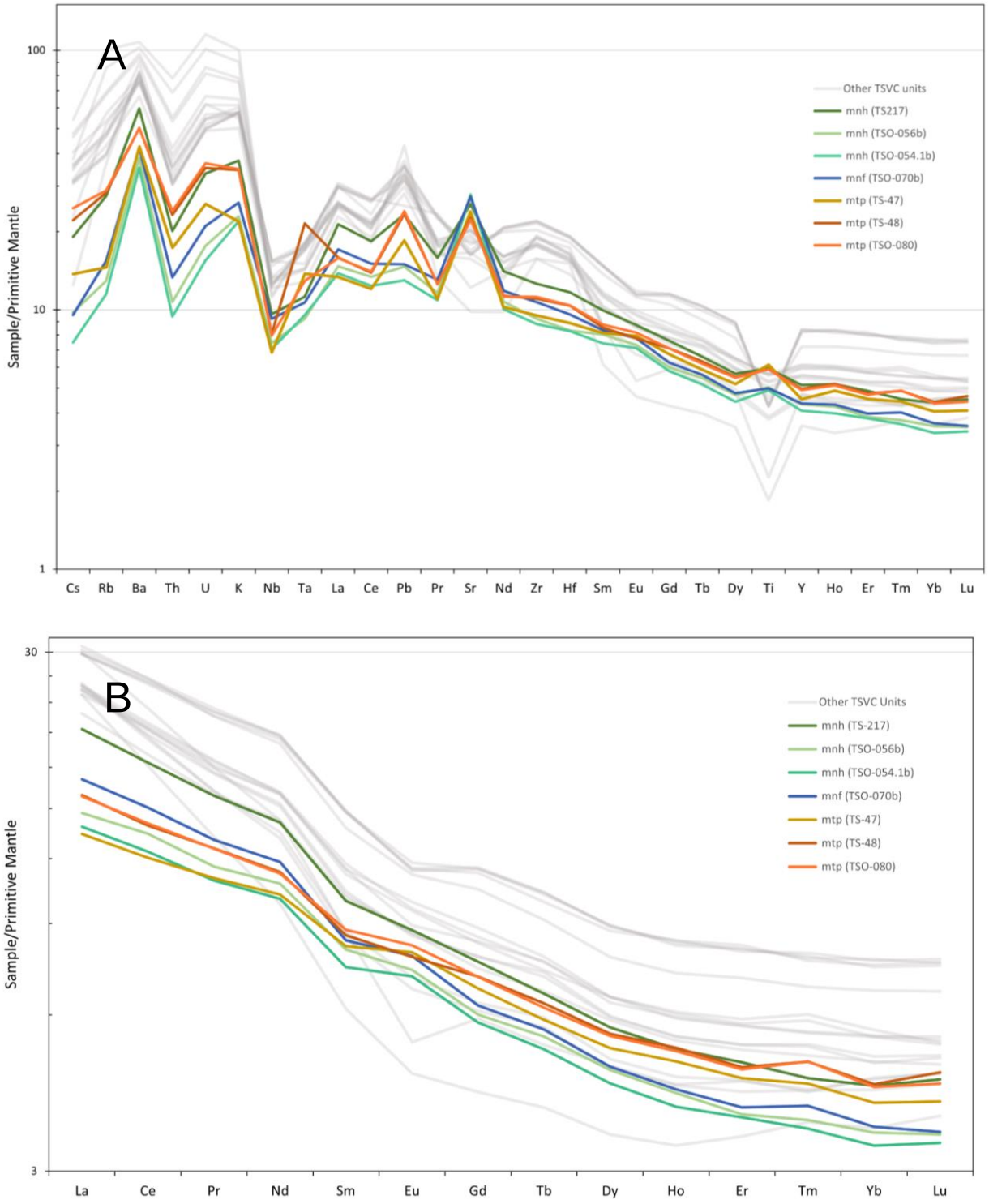

Figure 7: Whole rock trace element data for select TSVC units. Basaltic andesites of interest are highlighted in color, while several more silicic lavas from the TSVC are plotted in grey for comparison. All plots are normalized to the primitive mantle values of Sun and McDonough (1989). **A)** Spider diagram illustrating the enrichment in Sr and Ti in units mnf, mnh, or mtp. **B)** Rare earth element (REE) plot, showing a depletion in Eu for more silicic lavas which is not observed in units of interest.

Whole rock trace element data are, for the most part, internally similar between all three units of interest. Compared to more silicic material erupted at the TSVC (several rhyolites, dacites, and andesites, for which data were available), units mnf, mnh, and mtp are strongly enriched in Sr and Ti, while being comparatively low in Rb, Ba, Th, U, K, La, Ce, Zr, and Hf (*Figure 7A*). Additionally, rare earth element (REE) analysis reveals that these units lack a significant depletion in Eu, characteristic of other more silicic lavas (Figure 7B). However, compared with units mnf and mnh, unit mtp is elevated in U, Ta, and Pb relative to neighboring elements (*Figure 7A*). Additionally, there is a slight depletion in Ni and Sr at similar silica contents, while other important trace elements such as Y and Zr are consistent between all three units of study (*Figure 8*).

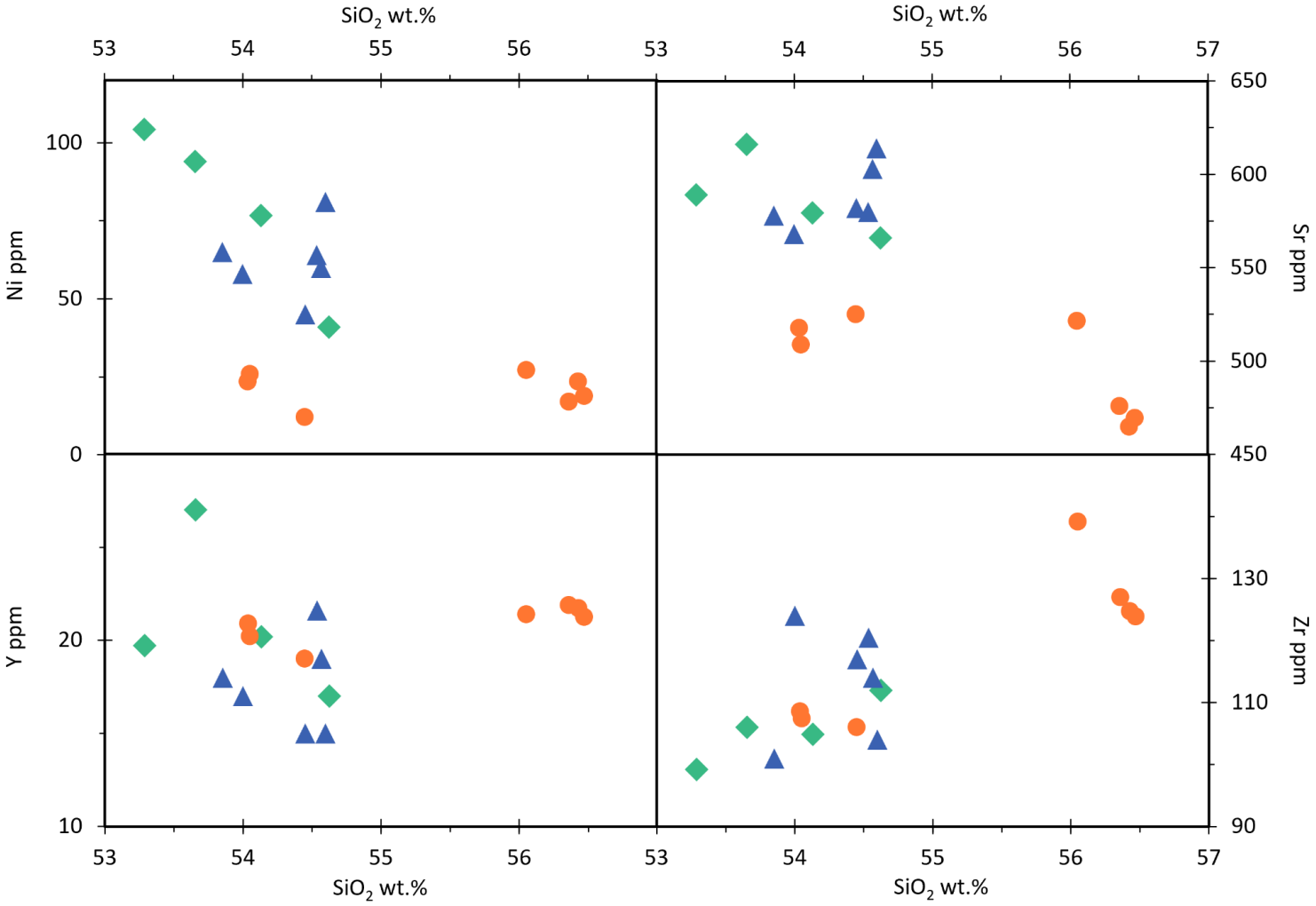

Figure 8: Bivariate plots showing whole rock compositions for select trace elements against silica content. Units mnf and mnh share near-identical compositions. Although unit mtp partially overlaps with units mnf and mnh in terms of SiO_2 wt%, it has distinctly lower Ni and Sr than either middle sister lava. Some trace elements such as Y show no observable difference between any of the units of interest, and other trace elements such as Zr increase roughly proportionally with increasing SiO_2.

4.3: Major Element Mineral Chemistry

Complete chemical data for major elements can be found in *Supplementary Data* under *Appendix 4: Major Element Geochemistry*. Crystal specific chemical observations and BSE images are compiled in *Appendix 5: Crystals Analyzed* and summarized in *Figures 9–12*. The following overview describes observed correlations between mineral chemistry and textures.

4.3.1: Unit mnf

Plagioclase compositions can be found in *Table A4.1*. Unit mnf contains two plagioclase populations. The first plagioclase population (mnf-PL1) has core $An_{78–85}$, FeO = 0.37–0.66 wt%, MgO = 0.07–0.11 wt%, and TiO_2 = 0.00–0.03 wt% and rim $An_{54–62,}$ FeO = 0.72–1.83 wt%, MgO = 0.14–0.96 wt%, and TiO_2 = 0.00–0.03 wt%. These are texturally simple, with normal zoning from a large, homogeneous, and occasionally sieved core to a thin, well-defined rim. Crystals resembling this population are found in all three units studied. The second mnf plagioclase population (mnf-PL2) is divided into two subgroups, texturally distinct but compositionally similar. The first subgroup (mnf-PL2A) has core $An_{76–85}$, FeO = 0.38–0.88 wt%, MgO = 0.06–0.30 wt%, and TiO_2 = 0.00–0.06 wt%, followed by two separate mantle zones and a distinct rim. The first mantle (M1) has $An_{55–70,}$ FeO = 0.47–0.76 wt%, MgO = 0.10–0.16 wt%, and TiO_2 = 0.01–0.08 wt%; the second mantle (M2) has $An_{71–82}$, FeO = 0.57–0.64 wt%, MgO = 0.09–0.13 wt%, and TiO_2 = 0.00–0.04 wt%; and the rim has $An_{58–64}$, FeO = 0.69–1.85 wt%, MgO =

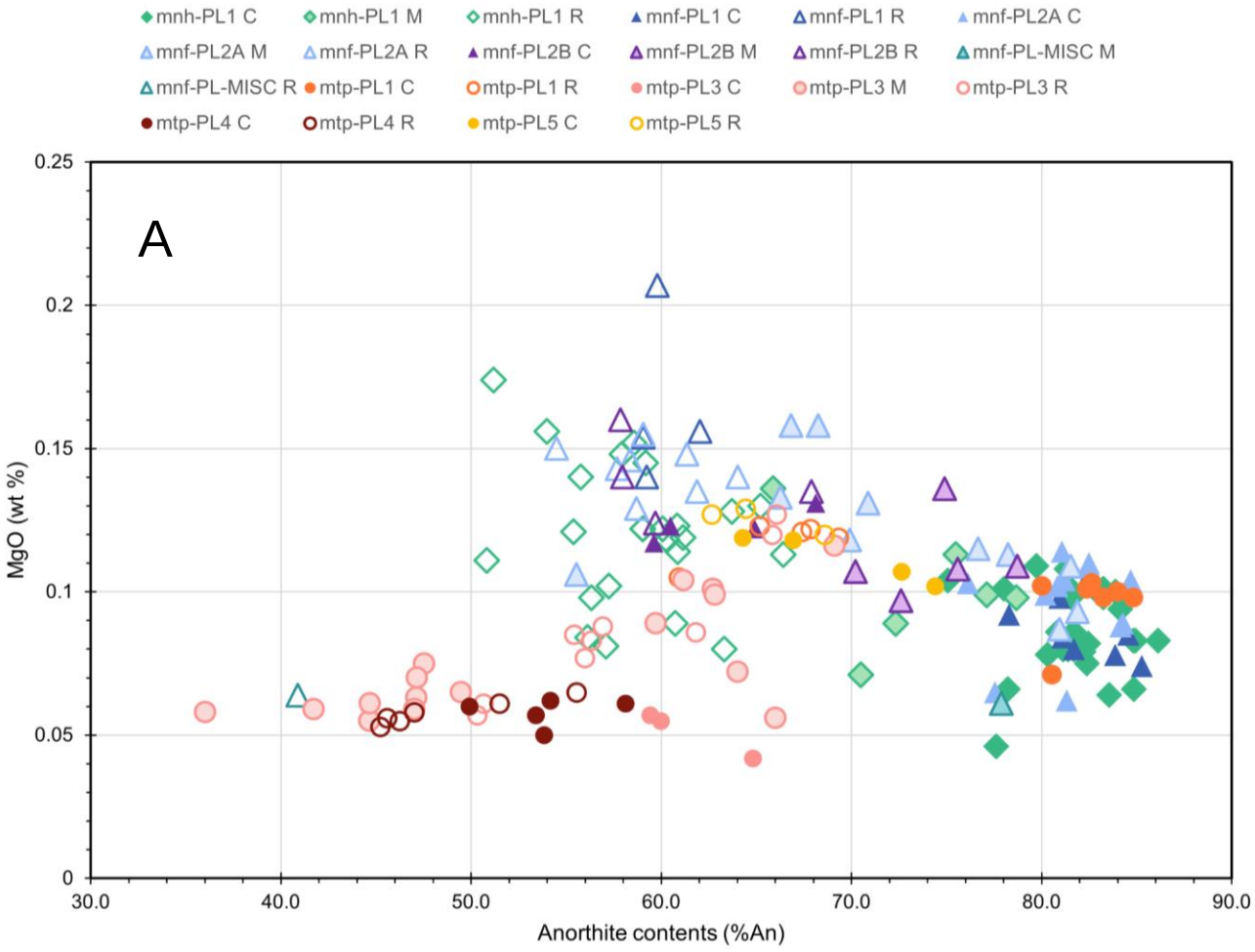

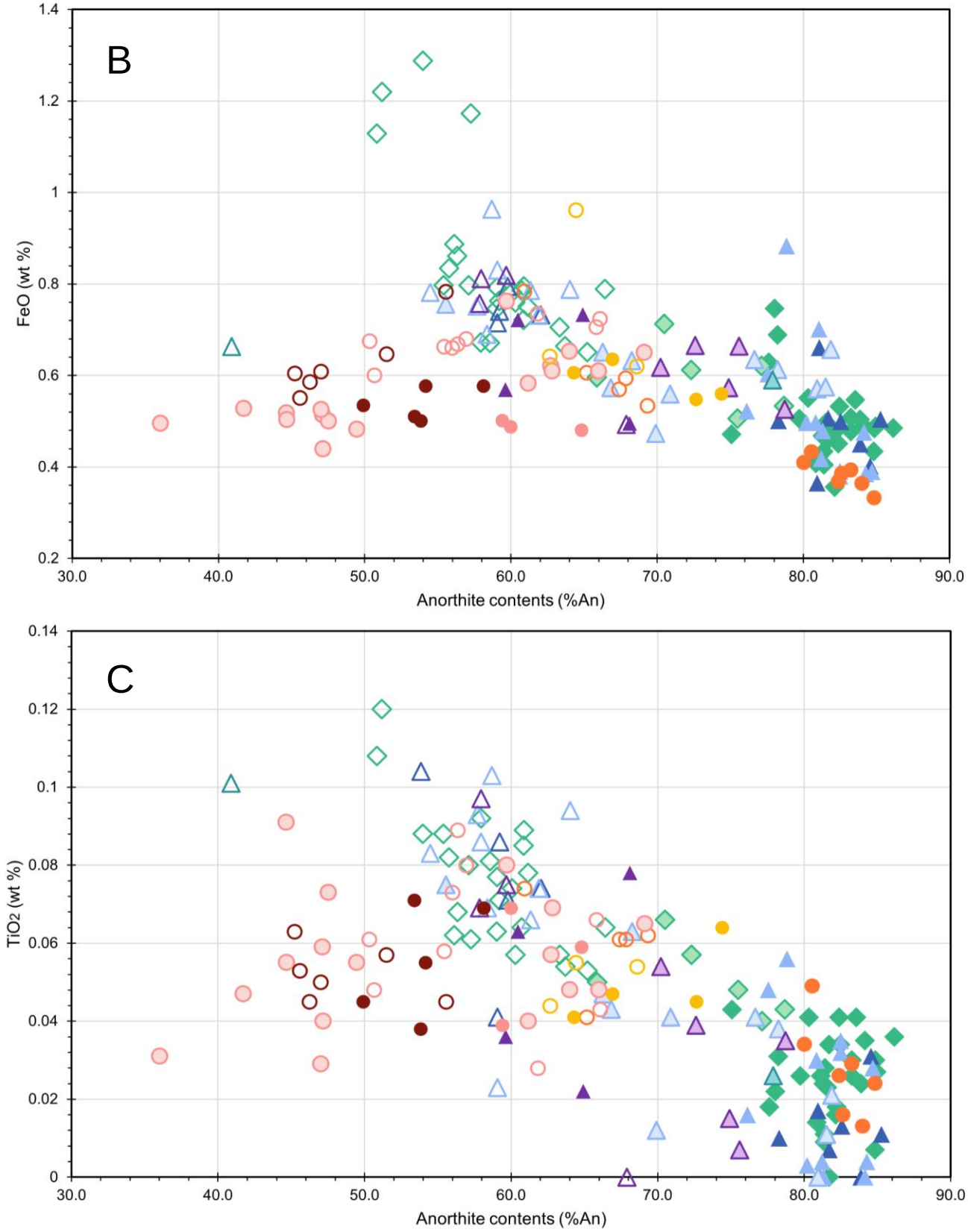

Figure 9: Compositional diagrams showing chemical trends in **A)** MgO, **B)** FeO^T, and **C)** TiO_2 for plagioclase from all three units of interest. Plagioclase analyses are symbolized by population, with blue to purple triangles for mnf, teal diamonds for mnh, and red to orange circles for mtp. Filled symbols indicate core (C) analyses, two-tone symbols indicate mantle (M) analyses, and hollow symbols indicate rim (R) analyses.

0.13–0.16 wt%, and TiO_2 = 0.02–0.10 wt%. The high-An cores in this textural subgroup have fine oscillatory zoning and are slightly resorbed in ~50% of crystals. The second textural subgroup (mnf-PL2B) has core $An_{60–68}$, FeO = 0.50–0.73 wt%, MgO = 0.12–0.13 wt%, and TiO_2 = 0.02–0.08 wt%; a single mantle with $An_{70–79}$, FeO = 0.57–0.67 wt%, MgO = 0.06–0.14 wt%, and TiO_2 = 0.01–0.05 wt%; and rim $An_{41–68}$, FeO = 0.49–0.82 wt%, MgO = 0.06–0.16 wt%, and TiO_2 = 0.00–0.10 wt%. Plagioclase in group mnf-PL2A often show substantial disequilibrium textures, including pervasive fine sieving in cores and resorbed mantles. In mnf-PL2B plagioclase, compositional and textural patterns from the core outwards are identical to those in mnf-PL2A plagioclase measured from M1 outwards, leading to the correlation within the same overall population. A single plagioclase crystal (mnf-PL-MISC) is compositionally unique (*Figure 9*), with mantle An_{78}, FeO = 0.59 wt%, MgO = 0.06 wt%, and TiO_2 = 0.03 wt% and far lower rim An_{41}, FeO = 0.66 wt%, MgO = 0.06 wt%, and TiO_2 = 0.10 wt%. This outlier is highly depleted in FeO and MgO, and exhibits complex resorption textures in its mantle and rim.

Olivine compositions are given in *Table A4.2*. Unit mnf contains two distinct olivine populations, plus an additional subgroup of reacted orthopyroxene with remnant olivine cores. These remnant cores (mnf-OLVC) have highly variable compositions of $Fo_{60–67}$; it is unclear whether measured forsterite contents are representative of their original composition, and they are therefore not considered in depth in this project. Crystals in the first distinct olivine population (mnf-OLV1) have core $Fo_{80–83}$ with NiO = 0.19–0.29 wt% and rim $Fo_{68–77}$ with NiO = 0.10–0.23 wt%. Population mnh-OLV1 olivine crystals show gradual normal zoning and are commonly clotted with plagioclase. Crystals in the second olivine population (mnf-OLV2) have core $Fo_{74–79}$ with NiO = 0.13–0.24 wt%, and rim $Fo_{68–72}$ with NiO = 0.10–0.21 wt%. Cores are mostly unzoned with a normal rim, while three out of nine have reverse-zoned cores, followed by a thin, normal rim. Population mnf-OLV2 olivine are highly embayed and degraded.

Pyroxene compositions are found in *Table A4.3*. In thin section, unit mnf contains predominantly orthopyroxenes as well as rare clinopyroxenes. However, only orthopyroxenes were sufficiently abundant and unreacted to undergo chemical analysis within the TSO-070 thick section. Unit mnf contains only one population of orthopyroxene (mnf-OPX1A-C). In general, this has core $Mg\#_{77–78}$, Wo_4, $En_{74–75}$, $Fs_{21–22}$, and Cr_2O_3 = 0.10–0.40 wt% and mantle $Mg\#_{65–72}$, Wo_4, $En_{62–69}$, $Fs_{28–34}$, and Cr_2O_3 = 0.00–0.05 wt%. Rim values diverge, with roughly half of crystals (mnf-OPX1A) returning to rim $Mg\#_{74–77}$, Wo_4, $En_{71–74}$, $Fs_{22–25}$, and Cr_2O_3 = 0.07–0.12 wt%. These exhibit gradational normal zoning from patchy cores to mantles, followed by an abrupt, thin, and reverse-zoned rim, chemically similar to cores. These crystals are moderately to heavily embayed but retain a recognizable subhedral columnar form. The remainder of mnf orthopyroxene crystals (mnf-OPX1B; those reacted from relict olivine cores) diverge to a higher-Ca outer mantle or rim (*Figure 10*) with $Mg\#_{64–66}$, $Wo_{7–13}$, $En_{57–65}$, $Fs_{30–34}$ and Cr_2O_3 = 0.00–0.08 wt%. These are extremely heavily embayed and entirely anhedral, making accurate rim sampling difficult. Both subgroups appear alongside one another in the same clot, hence their designation within the same general population. Data for Cr_2O_3 cluster poorly and are not considered in distinguishing populations.

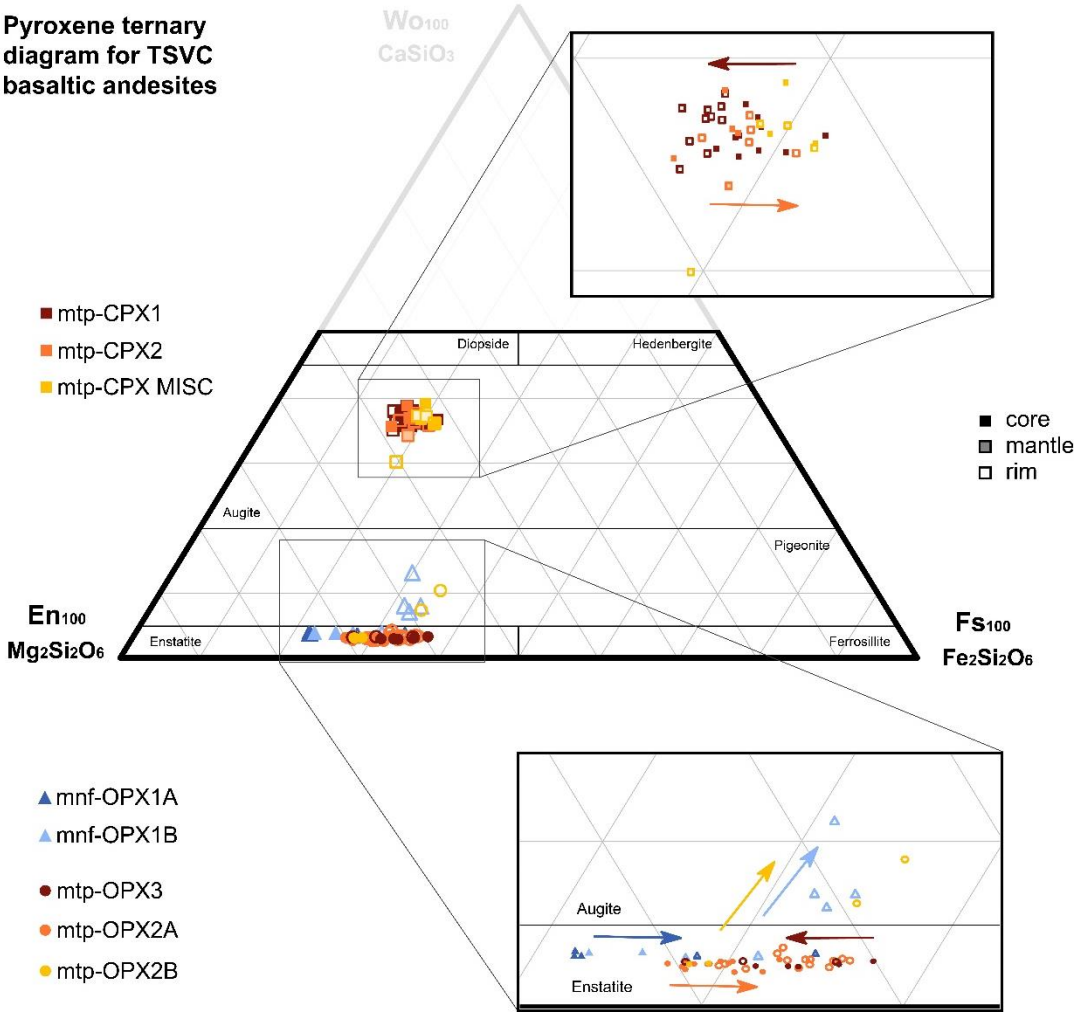

Figure 10: Ternary diagram giving pyroxene compositions for units mnf and mtp as percentages of En, Fs, and Wo. Symbology follows the same color scheme as *Figure 9*, with triangles representing mnf orthopyroxene, circles representing mtp orthopyroxene, and squares representing mtp clinopyroxene. Colored arrows correspond with their matching populations and are used to illustrate the simple compositional trends used to distinguish each population.

4.3.2: Unit mnh

Unit mnh contains only one plagioclase population (mnh-PL1), texturally similar to mnf-PL1. These crystals have core $An_{75–85}$, FeO = 0.37–0.75 wt%, MgO = 0.05–0.11 wt%, and TiO_2 = 0.01–0.04 wt%; and rim $An_{51–65}$, FeO = 0.65–1.29 wt%, MgO = 0.07–0.17 wt%, and TiO_2 = 0.05–0.12 wt%. All plagioclase crystals have homogenous cores and a distinct, clearly defined rim, although in some crystals (2 out of 28) this rim was too thin to reliably analyze. Additionally, some crystals (5 out of 48) exhibit a distinct, intermediate mantle zone between the core and rim, representing normal step-zoning with $An_{66–79}$, FeO = 0.51–0.62 wt%, MgO = 0.09–0.14 wt%, and TiO_2 = 0.04–0.06 wt%. One crystal analyzed (TSO-054.1_plg048) is chemically similar but texturally unique, with fine, repeating resorption surfaces in the rim, although this is not significant enough to constitute a separate population.

Additionally, unit mnh contains two distinct olivine populations, with similar forsterite compositions to mnf olivine. The first (mnh-OLV1) has core $Fo_{81–84}$ with NiO = 0.29–0.38 wt% and rim Fo_{72-76} with NiO = 0.14–0.34 wt%. Population mnh-OLV1 olivine have a large,

homogeneous core and a thin, normal-zoned rim. These commonly contain melt inclusions, and sometimes overgrow and enclose small plagioclase. The second olivine population (mnh-OLV2) is lower in Fo and Ni, having core $Fo_{74–79}$ with NiO = 0.14–0.22 wt%, and rim $Fo_{68–72}$ with NiO = 0.12–0.17 wt%. Cores are unzoned to subtly reverse-zoned, followed by a thin band of pronounced normal gradation to the rim. These are typically smaller and more fragmental than mnh-OLV1 olivine. Although otherwise largely similar in appearance, there is a clear compositional discontinuity between these two populations in both Fo and NiO (*Figure 11)*.

4.3.3: Unit mtp

Plagioclase textures in unit mtp are quite diverse and are sorted into four distinct populations. The first of these (mtp-PL1) has core $An_{80–85}$, FeO = 0.33–0.43 wt%, MgO = 0.07–0.10 wt%, and TiO_2 = 0.01–0.05 wt% and rim $An_{61–69}$, FeO = 0.53–0.78 wt%, MgO = 0.10–0.12 wt%, and TiO_2 = 0.04–0.07 wt%. These exhibit simple normal zoning from a homogeneous core to a substantial rim, with a prominent, rounded resorption surface between them. Two out of seven phenocrysts bear a subtle intermediate-An mantle zone between the core and rim, although data could not be obtained. Overall, mtp-PL1 plagioclase share a close resemblance in texture and composition to population 1 plagioclase in mnf and mnh (*Figure 9*). The next plagioclase population (mtp-PL3) is far more texturally complex, having core $An_{59–64}$, FeO = 0.48–0.50 wt%, MgO = 0.04–0.06 wt%, and TiO_2 = 0.04–0.07 wt%; a resorbed primary mantle (M1) with $An_{36–50}$, FeO = 0.44–0.53 wt%, MgO = 0.06–0.07 wt%, and TiO_2 = 0.03–0.09 wt%; a secondary mantle (M2) with $An_{60–69}$, FeO = 0.58–0.76 wt%, MgO = 0.06–0.10 wt%, and TiO_2 = 0.04–0.08 wt%; and a final rim with $An_{50–66}$, FeO = 0.60–0.74 wt%, MgO = 0.06–0.13 wt%, and TiO_2 = 0.04–0.07 wt%. Cores are extremely patchy with boxy/cellular reaction textures, such that suitable data could only be collected for three out of nine crystals. These cores zone normally/gradationally to the primary mantle, which is interrupted by an extremely rounded, abrupt resorption surface and overlain by another band of gradational zoning from the secondary mantle to the rim. This population is substantially depleted in Mg when compared to mtp-PL1 plagioclase (*Figure 9*). The next plagioclase population (mtp-PL4) has core $An_{50–58}$, FeO = 0.50–0.58 wt%, MgO = 0.05–0.06 wt%, and TiO_2 = 0.04–0.07 wt%; mantle An_{62}, FeO = 0.51 wt%, MgO = 0.06 wt%, and TiO_2 = 0.07 wt%; and rim $An_{45–56}$, FeO = 0.50–0.58 wt%, MgO = 0.05–0.06 wt%, and TiO_2 = 0.04–0.07 wt%. Crystals in this population are texturally variable, typically exhibiting a patchy, coarsely sieved core, an oscillatory-zoned mantle, and a distinct rim. Although somewhat differently zoned, these crystals share similar low Mg concentrations with mtp-PL3 plagioclase. The final mtp plagioclase population (mtp-PL5) includes four miscellaneous crystals occupying a generally similar range of compositions, with core $An_{64–74}$, FeO = 0.55–0.64 wt%, MgO = 0.10–0.12 wt%, and TiO_2 = 0.04–0.06 wt% and rim $An_{63–59}$, FeO = 0.62–0.96 wt%, MgO = 0.12–0.13 wt%, and TiO_2 = 0.04–0.06 wt%. Population mtp-PL5 plagioclase crystals are coarsely oscillatory-zoned throughout or indistinctly zoned, and are the only plagioclase found clotted with olivine in mtp.

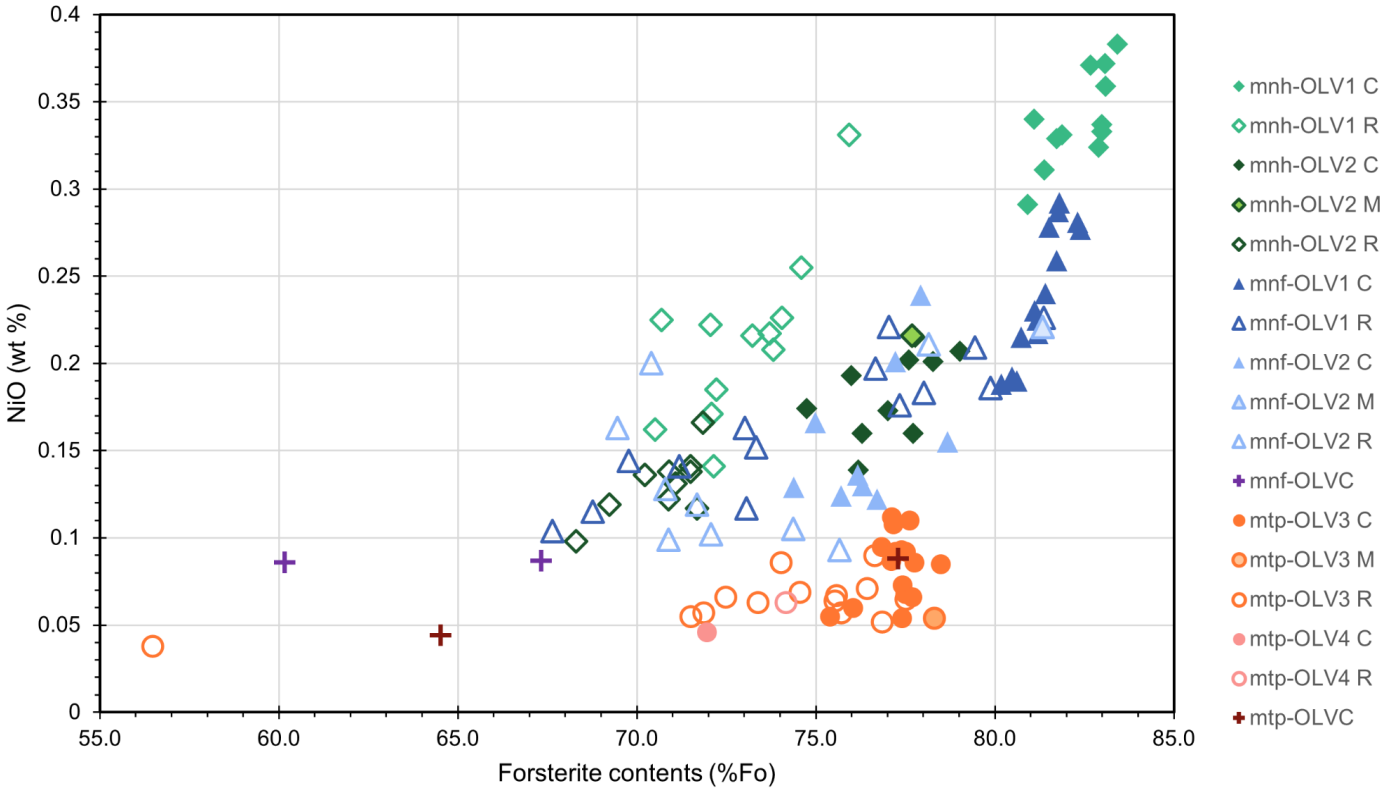

Figure 11: Compositional diagram showing trends in NiO for olivine from all three units of interest. Olivine analyses are symbolized by population following the same color scheme as *Figure 9*. Additionally, cross symbols are used to indicate analyses of relict olivine cores, observed reacting into pyroxene in units mnf and mtp.

Unit mtp contains one predominant olivine population, plus an additional subgroup of remnant olivine cores in reacted pyroxene crystals similar to those in unit mnf. The remnant olivine cores (mtp-OLVC) have $Fo_{65–77}$, and, as with mnf-OLVC, it is unclear whether measured forsterite contents are representative of their original composition; only one of the two remnant cores clusters well with other olivine phenocrysts in the sample. The predominant olivine population (mtp-OLV3) has core Fo_{75-79} with NiO = 0.05–0.11 wt% and variable rim $Fo_{56–78}$ with NiO = 0.03–0.09 wt%. Population mtp-OLV2 olivine crystals consistently show gradual normal zoning and are commonly clotted in association with plagioclase, although not with orthopyroxene or clinopyroxene. Population mtp-OLV3 is significantly lower in Ni than olivine in mnf and mnh, even at similar forsterite contents (*Figure 11*). Additionally, a single olivine phenocryst analyzed has significantly lower core Fo_{72}, and is reversely zoned with rim Fo_{74}. Without additional data, it is unclear whether this crystal constitutes a separate population.

Orthopyroxene phenocrysts in mtp are divided into two populations, characterized by normal and reverse zoning, although there is much compositional overlap between these groups. The first (mtp_OPX2) has core $Mg\#_{68–73}$, $Wo_{2–3}$, $En_{64–70}$, $Fs_{27–32}$, and Cr_2O_3 = 0.00–0.02 wt% and rim $Mg\#_{64–70}$, $Wo_{3–4}$, $En_{61–67}$, $Fs_{29–36}$, and Cr_2O_3 = 0.00–0.04 wt%. These are unzoned to subtly reverse zoned in cores, followed by prominent normal zoning to rims. In two out of sixteen crystals (mtp-OPX2B), rims diverge towards higher Ca with Wo_{7-10}, $En_{55–59}$, $Fs_{34–35}$, plotting similarly to mnf-OPX1B rims (*Figure 10*). The remainder of mtp orthopyroxene crystals (mtp-OPX3) have

core $Mg\#_{62–68}$, Wo_{3}, $En_{60–66}$, $Fs_{31–37}$, and Cr_2O_3 = 0.00–0.02 wt% and rim $Mg\#_{64–72}$, Wo_{3}, $En_{62–69}$, $Fs_{28–35}$, and Cr_2O_3 = 0.02 wt%. These are reversely zoned, and in two cases are observed reacting into clinopyroxene.

Clinopyroxene phenocrysts are divided similarly between overlapping normal- and reverse-zoned populations, with the addition of several miscellaneous crystals. The first population (mtp-CPX1) has core $Mg\#_{67–73}$, $Wo_{36–38}$, $En_{42–46}$, $Fs_{18–22}$, and Cr_2O_3 = 0.00–0.04 wt% and rim $Mg\#_{73–76}$, $Wo_{35–39}$, $En_{45–48}$, $Fs_{15–18}$, and Cr_2O_3 = 0.00–0.02 wt%. These have homogeneous to patchy and subtly normal-zoned cores, followed by a prominent, rounded resorption surface and a distinct, reversely zoned rim. An additional population (mtp-CPX2) has core $Mg\#_{72–75}$, $Wo_{36–39}$, $En_{45–48}$, $Fs_{16–18}$, and Cr_2O_3 = 0.01–0.07 wt%; mantle $Mg\#_{72}$, Wo_{34}, En_{47}, Fs_{19}, and Cr_2O_3 = 0.02 wt%; and rim $Mg\#_{68–74}$, $Wo_{36–38}$, $En_{43–47}$, $Fs_{17–21}$, and Cr_2O_3 = 0.00–0.02 wt%. These are reversely zoned from a patchy, irregular core to a wide, homogeneous rim. Finally, several miscellaneous and highly variable clinopyroxene crystals (mtp-CPX-MISC) range from $Mg\#_{69–73}$, $Wo_{30–39}$, $En_{42–50}$, $Fs_{19–22}$, and Cr_2O_3 = 0.00–0.31. These include an orthopyroxene reaction rim and several other phenocrysts that cannot be confidently classified.

4.4: Mineral Clotting Relationships

Clots are described only for cases containing at least one phenocryst for which suitable chemical data could be collected, to aid in identification of constituent populations. Unit mnf contains eleven described clots, of which nine contain only olivine and plagioclase. Olivine from both mnf-OLV1 and mnf-OLV2 are found interchangeably with plagioclase from mnf-PL1 and mnf-PL2, in variable proportions and combinations. One clot contains only small, subhedral (~0.2 mm) mnf-OLV2 olivine crystals. A single clot contains highly reacted orthopyroxene phenocrysts (mnf-OPX1) with relict olivine cores and a single plagioclase phenocryst (crystal 070_plg036; population mnf-PL-MISC) which is compositionally unique and cannot be classified in either existing mnf population. All crystals present in this clot show significant disequilibrium textures, and no other mnf clot bears pyroxene.

In unit mnh, the majority of clots are similar to those in mnf. Four out of seven clots contain olivine and plagioclase, ranging from roughly equal in proportions to plagioclase- predominant. These clots contain olivine from both populations mnh-OLV1 and mnh-OLV2, alongside mnh-PL1 plagioclase. In two clots, mnh-OLV1 olivine overgrows and partially encloses small plagioclase laths, and in one clot, exceptionally large mnh-OLV1 olivine phenocrysts are by far the predominant component. These large, coarsely granular, olivine-dominated clots are visible in hand sample.

In unit mtp, clotting relationships are far more complex. Out of fourteen clots in total, only four contain mtp-OLV3 olivine, found exclusively alongside mtp-PL5 plagioclase. Plagioclase from the low-Mg group (mtp-PL3 and mtp-PL4) are occasionally found in monomineralic clots with themselves but are more commonly associated with pyroxenes. In three clots, reversely zoned orthopyroxene and clinopyroxene crystals (mtp-OPX3 and mtp-CPX1) are found clotted with

Population					Composition	Units Observed		
Mineral	*ID*	*Texture*	*Description*	*Profile*	*%An, %Fo, Mg#*	*mnf*	*mnh*	*mtp*
Plagioclase	PL1	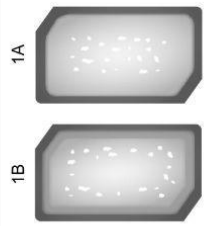	Normally zoned with high-An core and abrupt, lower-An rim. Variably sieved within core. In mtp, rim is typically thicker, with a prominent resorption surface after the core. Small subset contain an additional intermediate- An mantle zone. Sieving commonly found as a concentric band just before mantle. - 100% of mnh PL - ~30% in mnf & mtp	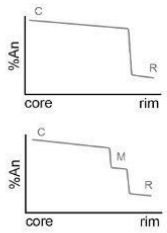	C: 75–86 R: 51–70 C: 75–86 M: 66–78 R: 51–63	X 	X X	X
	PL2	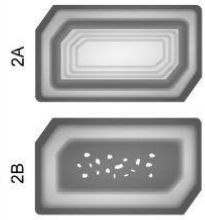	High-An, normally zoned, finely oscillatory core followed by one intermediate-An mantle (M_1), one higher-An mantle (M_2), and final low-An rim. Roughly 50% lack the high-An core; instead, core zone closely resembles M_1 described above, with occasional patchy sieving. - ~70% of mnf PL	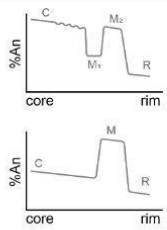	C: 76–85 M_1: 67–69 M_2: 77–82 R: 55–64 C: 59–68 M: 70–79 R: 41–60	X X	 	
	PL3		Intermediate-An, patchy-zoned, resorbed core, extreme low-An mantle terminating in highly rounded resorption surface, final intermediate-An, normally-zoned rim. - ~30% of mtp PL	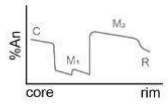	C: 59–64 M_1: 36–49 M_2: 60–69 R: 50–56			X
	PL4		Normally zoned with intermediate-An, patchy-zoned, resorbed core, finely oscillatory mantle, and slightly lower-An rim. - ~25% of mtp PL	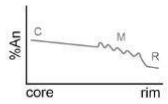	C: 50–58 M: 55–56 R: 45–51			X
	PL5	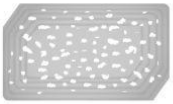	Miscellaneous PL (texturally variable); typically intermediate to high-An, finely oscillatory zoned, with pervasive hazy sieving. - ~15% of mtp PL	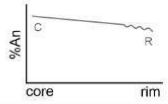	C: 64–74 R: 63–69			X
Olivine	OLV1		Normally zoned with high-Fo core, grading towards lower-Fo rim. Melt inclusions common, strongly enriched in Ni - 60–70% in mnf, mnh	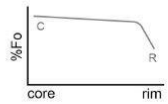	C: 80–83 R: 68–80	X	X	
	OLV2		Subtle reverse zoning from intermediate/high-Fo core to mantle, normal lower-Fo rim. Commonly embayed, with intermediate to high Ni. - 30-40% in mnf, mnh	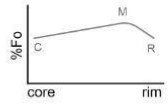	C: 75–78 M: 79–81 R: 68–73	X	X	
	OLV3		Unzoned to subtly reverse-zoned, intermediate-Fo core followed by sudden low-Fo rim. Often lightly fractured, depleted in Ni. - ~100% of mtp OLV	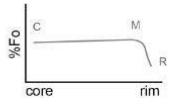	C: 75–78 M: 78 R: 68–73			X
Orthopyroxene	OPX1	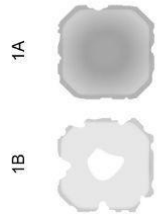	Intermediate/high-Mg, normally zoned core grading into lower/intermediate-Mg mantle, abrupt higher-Mg rim, sometimes including CPX reaction rim. Small subset has reacted from OLV, containing relict OLV core instead of high-Mg zone. These are typically slightly lower in Mg overall and heavily embayed/resorbed. - 100% of mnf OPX	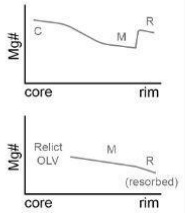	C: 77–78 M: 65–71 R: 74–77 C: Relict OLV M: 68–66 R: 64–66	X X	 	
	OPX2		Subtle reverse zoning from intermediate-Mg core to high-Mg mantle, followed by lower-Mg, normal zoned rim - ~70% of mtp OPX	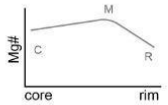	C: 68–70 M: 71–73 R: 64–69			X
	OPX3		Subtle normal zoning from an intermediate-low Mg core to a low-Mg rim, followed by abrupt reverse zoning to a high Mg rim - ~30% of mtp OPX	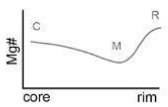	C: 62–68 R: 64–72			X
Clinopyroxene	CPX1		Normally zoned from high-Mg, patchy-zoned, slightly sieved core to low-Mg mantle, followed by prominent resorption surface and reverse-zoned, high-Mg rim - 70% of mtp CPX	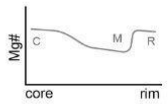	C: 72–75 M: 69–71 R: 73–75			X
	CPX2		Normally zoned with intermediate/high-Mg, resorbed core followed by low-Mg rim. Occasionally found reacting with OPX. - 30% of mtp CPX	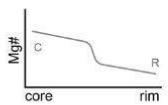	C: 70–73 R: 68–71			X

Figure 12 (previous page): Summary figure showing mineral types found in all three units of study, organized by population. A simple cartoon is used to depict the textural relationship between each chemical zone, and an approximated chemical profile is plotted based on EMPA data and textural observations of BSE images. Checked and shaded boxes in the "Units Observed" column indicate that population occurs in the unit for that column.

mtp-PL3 plagioclase, while in four clots, normally zoned orthopyroxene and clinopyroxene crystals (mtp-OPX2 and mtp-CPX2) are consistently found clotted with mtp-PL4 plagioclase. The latter group includes one exceptionally large clot (~4 mm in diameter), visible with the naked eye, which contains interstitial glass. Most commonly, pyroxene-bearing clots contain either orthopyroxene or clinopyroxene, although in three cases orthopyroxene and clinopyroxene phenocrysts of the same zoning style are found clotted alongside one another, including one case where both phenocrysts contain relict olivine cores.

5: Discussion

5.1: Evaluating Mineral Populations

Textural observations within mineral populations, combined with changes in mineral chemistry, can serve as a detailed record of magmatic changes experienced by each crystal throughout its growth history. Drawing these distinct growth histories together through comparative analysis of each of each mineral population and their relationships with one another allows for broader interpretations regarding the open-system magmatic processes responsible for the formation of each lava (Streck, 2008).

5.1.1: Plagioclase

Plagioclase is especially useful in evaluating magmatic processes because it is abundant and clearly records and displays zoning patterns associated with changes in temperature, pressure, water contents, and chemistry of magmatic systems (Ginibre *et al.,* 2007). With regards to plagioclase, the most striking observation between the three units of study is the presence of a single, chemically similar population present in all three lavas. Among plagioclase studied, population PL1 plagioclase phenocrysts are texturally and compositionally simplest in all units, exhibiting normal step-zoning alongside a progressive enrichment in minor elements Mg, Fe, and Ti at decreasing anorthite contents (*Figure 9*). A typical fractionation trend should produce a depletion in these mafic-compatible elements at decreasing anorthite contents (e.g., Shane, 2015), so the observed zoning may result from mixing or contamination of the original mafic melt (Component 1) by a more evolved, Mg-, Fe-, and Ti-enriched melt, producing a hybrid magma (Component 2) in later stages of crystallization. This hypothesis agrees with the presence of an abrupt step-zoned boundary between cores and rims, indicative of a sudden change in magmatic conditions rather than a gradual one.

In both mnf and mnh, all plagioclase crystals studied (with the exception of a single outlier in mnf) fall along this chemical trend, constituting a single compositional suite. Crystal zones group in two discrete compositional clusters, reflective of the two hypothesized original

components (*Figure 13*). Component 1 is characterized by plagioclase with high anorthite contents ($An_{70–86}$) and intermediate to low abundances of mafic elements (MgO = 0.04–0.12 wt%, FeO = 0.3–0.8 wt%, TiO_2 = 0.00–0.05). This chemical group is interpreted to record the most primitive melt preserved in crystal zones and includes cores of all PL1 plagioclase as well as all high-An zones in mnf-PL2 phenocrysts. Rims for both populations, as well as all lower-An zones in mnf-PL2 occur in a secondary chemical group associated with Component 2, with intermediate anorthite contents ($An_{50–74}$) and high abundances of mafic elements (MgO = 0.08–0.21 wt%, FeO = 0.5–1.3 wt%, TiO_2 = 0.02–0.12). While PL1 plagioclase from both units apparently record a single mixing event from cores (Component 1) to rims (Component 2), plagioclase in mnf-PL2 may record several repeated cycles of mixing, based on the observed morphology of alternating high- and low-An bands.

In mtp, two distinct compositional suites of plagioclase are observed, each containing two distinct populations (*Figure 13B*). The first suite, termed the enriching suite, abides by identical chemical trends to Middle Sister plagioclase, with an increasing trend in Mg, Fe, and Ti at more evolved (lower-An) compositions. This suite includes both population mtp-PL1 and mtp-PL5. Plagioclase in population mtp-PL1 is texturally and compositionally similar to PL1 plagioclase from Middle Sister, with the exception of a more pronounced resorption surface separating the core from a slightly thicker rim. However, mtp-PL5 plagioclase are oscillatory-zoned with a range of core compositions falling roughly in between the fields for Components 1 and 2, shifting gradually towards Component 2 rimwards. These have identical rim compositions to population mtp-PL1 and may represent crystals nucleated and grown at some point during a cyclical mixing process between Components 1 and 2, or may potentially derive from a separate, unidentified magmatic component which mixed and homogenized with the enriching suite. Given that olivine in mtp clot exclusively with mtp-PL5 plagioclase, future investigation into olivine chemistry may shed light on these possibilities.

The second compositional suite in mtp, termed the low-Mg suite, represents a third magmatic member (Member 3), unique to mtp and characterized by plagioclase with low anorthite contents ($An_{36–66}$) and low Mg relative to Fe and Ti (MgO = 0.04–0.08 wt%, FeO = 0.4–0.7 wt%, TiO_2 = 0.03–0.08). The low-Mg suite contains populations mtp-PL3 and mtp-PL4. Both populations have roughly similar core compositions and initially abide by similar chemical trends, with both populations decreasing in anorthite contents via normal gradational zoning from the core outwards. This is interpreted to represent simple fractionation in a relatively closed system. However, in population mtp-PL3, this normally zoned core to inner mantle region is interrupted by an abrupt, prominent, and highly rounded resorption surface. Beyond this resorption surface, compositions shift onto the trajectory of the enriching suite, with outer mantles and rims being comparatively elevated in MgO, ultimately converging in most crystals to similar rim compositions as mtp-PL1 and mtp-PL5 plagioclase. This provides strong evidence for mixing between magmas of the low-Mg and enriching suites, resulting in the observed resorption and eventual overgrowth of plagioclase in mtp-PL3 from a newly homogenized melt. This two-part mixing may also explain the presence of a much more prominent resorption surface

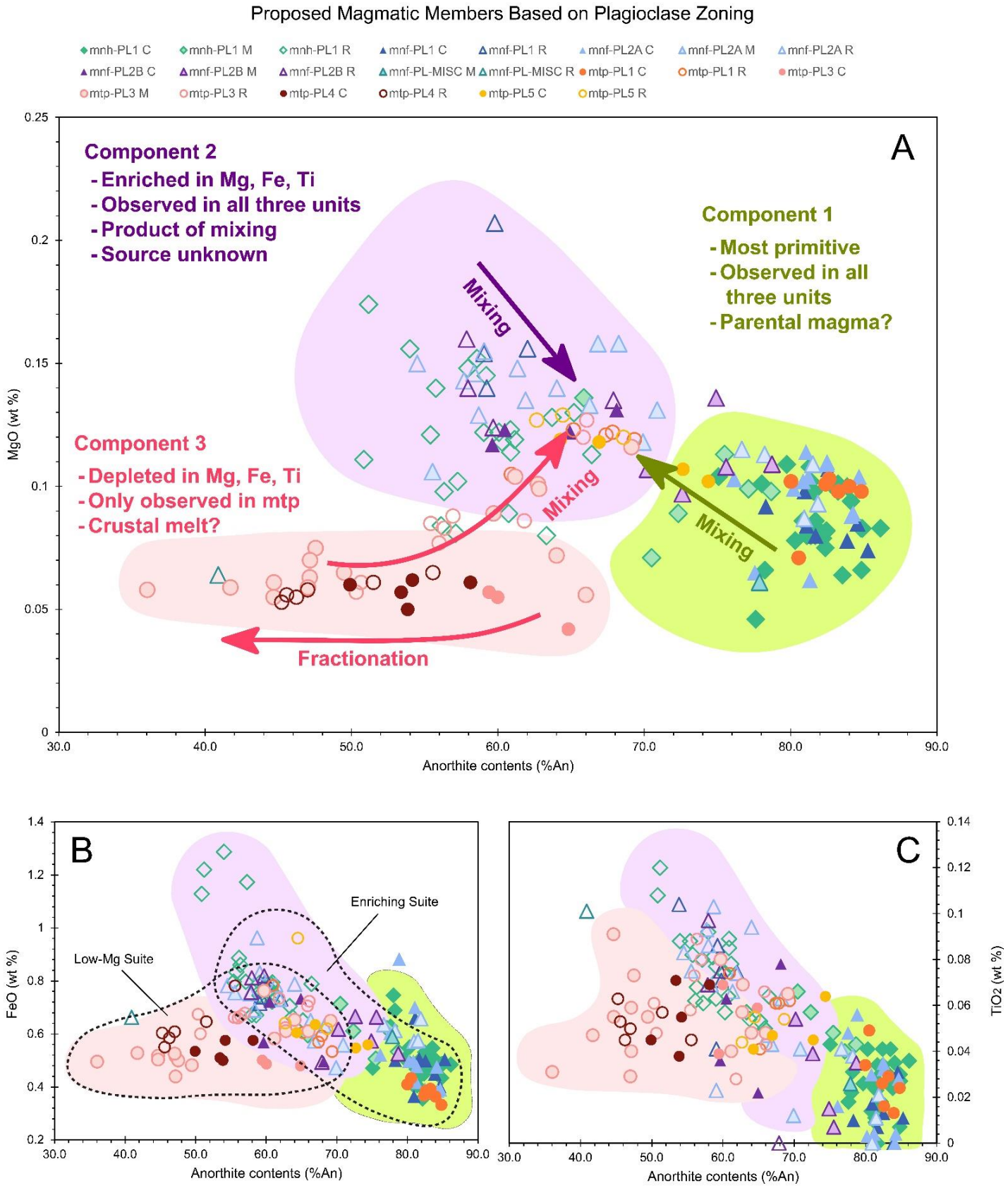

Figure 13: Illustration of proposed magmatic components based on zoning in plagioclase from units of study for **A)** MgO, **B)** FeO, and **C)** TiO_2. Symbology matches that of *Figure 9*, with the addition of arrows showing compositional pathways and green, purple, and pink fields to indicate the compositional distributions of Components 1, 2, and 3, respectively. Components 1 and 2 combine via mixing in all three units of study, while Component 3 is unique to mtp.

from core to rim in mtp-PL1 plagioclase compared to those from either Middle Sister unit. By contrast, population mtp-PL4 plagioclase phenocrysts lack a strong resorption surface and subsequent chemical homogenization, abiding by the low-Mg chemical suite from core to rim. This suggests these crystals remained isolated from the process of mixing and homogenization responsible for disequilibrium textures in mtp-PL3.

5.1.2: Olivine

Olivine is particularly useful in identifying different constituent magmas, as variations in Ni concentrations can be used to identify mantle source regions (e.g., Straub *et al.*, 2008, 2011). However, at present, genetic relationships between olivine in all three units require further investigation to comprehensively understand. Broadly speaking, units mnh and mnf have similar distributions of olivine, classified under two shared populations in each. These populations comprise crystals with high-forsterite ($Fo_{80–84}$) cores (OLV1) and those with lower-forsterite ($Fo_{74–79}$) cores (OLV2). Although a discontinuity in core forsterite contents exists for both units, serving as the basis for the distinction in populations, members of populations OLV1 and OLV2 in both units are found interchangeably in clots with PL1 plagioclase. Thus, it appears that both olivine populations are cognate with the same magmatic system involving the mixing of Components 1 and 2. However, the relationships between the respective olivine populations and the different compositional components have not yet been disentangled, and thus interpretations regarding the Ni contents of different olivine populations cannot be meaningfully extended to the context of magmatic processes. Furthermore, there is a slight discrepancy in Ni contents between populations mnh-OLV1 and mnf-OLV1 (*Figure 11*). Whether this constitutes natural compositional variability among genetically similar olivine, or if they in fact constitute distinct populations which happen to overlap in terms of forsterite contents, remains to be determined. By contrast, olivines in population OLV2 are compositionally identical in both mnf and mnh, and likely share similar origins. Further illustrating the distinction in magmatic processes between Middle Sister and South Sister, the olivine population found in unit mtp (mtp-OLV3) is chemically distinct from either population found in mnf and mnh. These phenocrysts have similar core forsterite to population OLV2, but are substantially lower in Ni. They are only found clotted with mtp-PL5 plagioclase, which suggests they may be able to shed light on the increase in Mg, Fe, and Ti in the enriching suite.

5.1.3: Pyroxenes

Compared with plagioclase and olivine, pyroxene phenocrysts are less abundant, but they help to highlight the compositional differences between units from Middle Sister and those from South Sister. First, orthopyroxene in unit mnf must be addressed. The presence of orthopyroxene in unit mnf constitutes the only significant mineralogical difference between mnf and the younger mnh, which is otherwise extraordinarily similar in terms of bulk chemistry and mineral textures. In mnf, orthopyroxene phenocrysts are rare and universally exhibit extensive reaction textures, with some crystals having grown as a reaction rim over relict olivine cores and others being

extensively embayed with traces of a high-Mg overgrowth. Both varieties are interpreted to be cogenetic, as they are found within the same clots alongside one miscellaneous plagioclase phenocryst which has substantially lower rim anorthite contents than any other crystal in the sample. The association between relict olivine cores and thick orthopyroxene reaction rims is suggestive of the peritectic reaction of $Fo+SiO_2$ into En, a process typically indicative of magma mixing or xenocrystic assimilation (Zellmer *et al.*, 2016). Furthermore, contamination experiments by Erdmann and others (2010) show that anhydrous phases like olivine and orthopyroxene either decompose or develop overgrowths in equilibrium with the host melt when introduced as xenocrysts. This is largely consistent with the pervasive embayment and reaction textures observed in orthopyroxene-bearing clots in mnf, suggesting these likely originated as xenolithic material containing plagioclase, olivine, and orthopyroxene, which subsequently experienced breakdown and overgrowth upon assimilation with the host melt. This process does not appear to have significantly altered the bulk chemistry of unit mnf, as whole rock data are identical to unit mnh, which lacks evident xenocrystic interactions and is otherwise mineralogically similar.

In mtp, pyroxene is far more abundant, and is evidently associated with a major magmatic component rather than xenocrystic material. Both orthopyroxene and clinopyroxene occur in two main textural varieties. Some (mtp-OPX2 and mtp-CPX2) are predominantly normally zoned, with relatively little evidence of chemical disequilibrium. This aligns with the compositional and textural trends of mtp-PL4 plagioclase, which commonly forms large, well-preserved clots with mtp-OPX2 and mtp-CPX2. Others (mtp-OPX3 and mtp-CPX1) exhibit gradational normal zoning from cores to mantles, then an abrupt, reversely zoned resorption surface. This too aligns well with the zoning and disequilibrium textures exhibited in mtp-PL3, which clots with mtp-OPX3 and mtp-CPX1. Thus, orthopyroxene and clinopyroxene are closely associated with the low-Mg compositional suite, and likely derive from Component 3. This agrees with the mixing hypothesis for mtp, and indicates the presence of a more evolved, pyroxene-bearing magma beneath South Sister which is not tapped at Middle Sister. Furthermore, the population divisions in pyroxene reinforce the hypothesis that mixing processes impacted mtp-PL3 and mtp-PL4 differently.

5.2: Tentative Systematic Interpretations

Parker and others (2023) propose a crustal model for the Three Sisters where abundant basaltic andesite magmas are initially generated in the lower crust via fractionation and assimilation then extracted to the shallow crust beneath North and Middle Sisters, further arguing for the formation of a large, distinct, subadjacent reservoir beneath South Sister where evolving silicic silicic mush periodically interacts with fresh pulses of basaltic andesite. This provides a valuable starting point from which to assess observations regarding mineral crystallization histories and to begin speculating as to the broader systematic processes indicated by those histories.

5.2.1: Middle Sister - Sustained Magma Recharge

The extreme compositional and textural similarity between units mnf and mnh suggests a relatively stable, consistent magmatic system supplying mafic magma to Middle Sister from 48 ka to 22 ka. The Mg, Fe, and Ti enrichment trend observed in these units is suggestive of two- part mixing between Components 1 and 2, but trace element analysis of mineral zones and thermobarometry will be necessary in order to constrain the origins of these components and evaluate the storage conditions experienced by them before and during mixing. Based on oscillatory textures in mnf-PL2, it appears this mixing process was not a one-time event, but a sustained process between consistent inputs. Furthermore, because this chemical trend is observed in all studied lavas (from Middle Sister and South Sister alike), it appears that this two-part mixing was an enduring process, resulting in the formation of a mutual hybrid magma which supplied these eruptions and was responsible for the crystallization and transport of PL1 plagioclase. This mixing process could have occurred at depth in a larger, long-lived, shared reservoir *before* discrete batches of resultant hybridized magma were extracted to separate magmatic systems beneath each vent, or it may represent a similar process which was repeated *in isolation* before each eruption. Further investigation is required to evaluate these possibilities.

Whole-rock investigations by Schmidt and Grunder (2011) have shown that basaltic andesites at the neighboring North Sister volcano were consistently generated via a two-part mixing of mantle-derived low-K tholeiitic magmas accumulating in the lower crust and minor partial melts of local basement rocks. In line with the lower crustal "hot zone" model of Annen and others (2006), late stage eruptions at North Sister are evidently characterized by trace element and isotopic signatures suggestive of mixing with a basalt-like crustal melt, possibly derived from heated cumulate piles in the lower crust (Schmidt and Grunder, 2011). Since the late eruptive stages at North Sister overlap temporally and compositionally with the eruption of mnf from Middle Sister, this model may provide a basis for understanding mixing processes in mnf and mnh. At present, detailed investigations of mineral chemistry are unavailable for North Sister, but this offers a potential avenue for future work investigating the transition in activity from North Sister to Middle Sister, and the assessing the possibility of a common genetic process linking the production of basaltic andesites at all three Sisters.

5.2.2: South Sister - Secondary Mixing and Crustal Contamination

At South Sister, there is strong evidence of an additional, secondary mixing process between the hybrid magma formed from Components 1 and 2, and an additional, compositionally distinct Component 3. Given that this secondary mixing process is not observed at Middle Sister, understanding the depth and origins of Component 3 may aid in constraining the degree of separation between reservoirs for Middle Sister and South Sister, as well as assessing the differences in magmatic processes impacting eruptions at both vents. Previous workers have concluded that basaltic andesites at South Sister are indeed products of mixing between mafic and intermediate components prior to eruption, citing heterogeneous, "swirled" groundmass textures, relatively high pre-eruptive temperatures (1015–1034°C), and phenocrysts which are out of

equilibrium with the host melt (Brophy and Dreher, 2000). The particular mtp sample studied by this investigation appears largely homogeneous, and neither temperatures nor mineral equilibria have been calculated at this time. However, the hypothesis of pre-eruptive mixing of hot, chemically distinct components provides a plausible model for interpretations of plagioclase chemistry and observed disequilibrium textures among Component 3 minerals. Still, the origins of this intermediate-composition third component remain a mystery.

Brophy and Dreher (2000) propose a crustal model for South Sister where discrete, independently fractionating bodies of basalt, andesite, and rhyolite magmas stall and occasionally mix to produce basaltic andesites and dacites. However, Waters and others (2021) find that dacite magmas at South Sister are likely generated as a primary partial melt of local mafic crust, rather than a mixture of end-member compositions. They describe the predominant plagioclase population in these dacites as having anorthite contents between roughly An_{35} and An_{65}, with phenocrysts ranging from roughly An_{45} to An_{55}. This aligns well with the range of compositions observed in mtp plagioclase from the low-Mg suite. Furthermore, the predominant texture for plagioclase phenocrysts is described as weakly zoned with abundant melt inclusions and irregular zone boundaries associated with rapid growth (Waters *et al.*, 2021). This matches the description for mtp-PL4 plagioclase very closely.

The preservation of mtp-PL4 plagioclase and their clotted pyroxene associates, which lack disequilibrium textures indicative of mixing and homogenization, does potentially pose an issue. These phenocrysts are found in large, well-preserved clots containing interstitial glass; the only quenched material found in any of the three units studied. One hypothesis explaining these observations is that populations mtp-PL4, mtp-OPX2, and mtp-CPX2 could represent antecrystic material belonging to the same body of magma as mtp-PL3, but located in an isolated, shallower reservoir which was cut off from the mixing processes that are clearly indicated by textural and chemical changes in mtp-PL3. These preserved relicts of the low-Mg suite could then have become entrained within the ascending hybrid magma just before eruption, affording too little time for significant crystal decomposition and overgrowth. This could imply a relatively shallow reservoir for Component 3, rapid ascent of the final hybrid magma preceding eruption, or some combination of both. A crustal model for arc volcanoes involving stratified and segregated lenses of melt within an unstable and highly crystalline mush system is well described by Cashman and others (2017), which could potentially account for the speculated processes.

Thus, it follows that unit mtp may potentially represent mixing between an original magma (represented by the enriching suite) similar to those erupted at Middle Sister around the same time and a dacitic crustal melt (represented by the low-Mg suite) similar to those erupted during earlier stages of activity at South Sister. In this case, comparative analysis of trace elements between Middle Sister and South Sister units could help identify the presence or absence of crustal signatures in mtp. While trace element data is not available for mineral zones at this time, it is observed that whole rock rare earth element patterns for unit mtp are overall similar to those of units mnf and mnh, with the exception of a relative elevation in U, Ta, and Pb (*Figure 7A*). Green (1995) shows that Nb/Ta can serve as a marker for crustal contamination, with arc magmas which

derive directly from original mantle melt sources typically having Nb/Ta > 12.5, and those which experienced significant crustal contamination typically having Nb/Ta < 12.5. In units mnf and mnh, Nb/Ta is similar, ranging from 12.8 to 14.9, while in unit mtp, Nb/Ta ranges from 6.5 to 10.7. This may support the notion of crustal contamination in mtp, and potentially aligns with the dacite mixing hypothesis. Although crustal melting is more commonly interpreted as a process found in the lower middle crust (DeBari and Greene, 2011), Waters and others (2021) point out that South Sister and its surroundings are characterized by an elevated geothermal gradient, high pre-eruptive temperatures for peripheral basalts, and a long history of regional volcanism, which may produce conditions particularly favorable to crustal melting.

By contrast, Parker and others (2023) do not cite crustal melting–but rather fractionation–as the predominant factor in the formation of dacites in the subadjacent silicic mush system described beneath South Sister, although this model still supports the mixing of South Sister dacites and basaltic andesites. As such, hypotheses regarding mixing with partial crustal melts and mush to explain the genesis of unit mtp remain purely speculative at this time. Future work including trace element analysis in plagioclase and pyroxene thermobarometry may aid in reconciling these models and hypotheses. Nonetheless, distinct mixing processes are clearly evidenced at South Sister, providing a valuable perspective from which to consider systematic differences within the TSVC.

6: Conclusions and Future Work

At present, many of the inferred magmatic processes and source regions proposed in this contribution are speculative at best. While the evidence presented does point towards several key conclusions about the nature of the magmatic system beneath Middle Sister and South Sister, these cannot be asserted with confidence until trace element data for mineral zones support or negate the interpretations drawn from major element and whole rock data, and additional analytical techniques such as thermobarometry are applied to further constrain the plumbing of the system. Future work is planned to accomplish these aims. With that being said, this investigation has yielded several important takeaways which will guide upcoming work on the horizon:

- The original, predominant magma for mafic lavas at both volcanoes from 48 ka to 22 ka could share similar origins, as evidenced by chemically similar plagioclase found in all three units of study. Unit mnh may represent a relatively unaltered eruption of this parental magma.
    - Mg, Fe, and Ti zoning in plagioclase suggest that this initial magma experienced a similar two-part mixing process at some point prior to all three eruptions. The origins, timing, and depth of the respective components still need to be constrained.
    - Olivine chemistry may shed light on the origins of discrete magmatic components involved in mixing. Further investigation is required to determine the origins of disparate olivine populations in Middle Sister units in particular.

    - Unit mnf may have been impacted slightly by assimilation of xenolithic material. This could be evaluated by assessing crystal-melt phase equilibria for suspected xenocrysts.

- At ~21 ka, South Sister was impacted by magma mixing processes which did not occur at Middle Sister. This suggests that shallow crustal reservoirs beneath Middle and South Sisters were likely not interconnected at that time, and mafic eruptions at each vent were governed by different processes.
    - The unique mixed component at South Sister may have been a partial crustal melt, similar to those described for earlier dacite eruptions. Trace element analysis of plagioclase and pyroxene thermobarometry may aid in evaluating this possibility.

References

Annen, C., Blundy, J. D. & Sparks, R. S. J. (2006). The Genesis of Intermediate and Silicic Magmas in Deep Crustal Hot Zones. *Journal of Petrology* **47**, 505–539.

Brophy, J. G. & Dreher, S. T. (2000). The origin of composition gaps at South Sister volcano, central Oregon: implications for fractional crystallization processes beneath active calc-alkaline volcanoes. *Journal of Volcanology and Geothermal Research* **102**, 287–307.

Calvert, A. T., Fierstein, J. & Hildreth, W. (2018). Eruptive history of Middle Sister, Oregon Cascades, USA–Product of a late Pleistocene eruptive episode. *Geosphere* **14**, 2118–2139.

Cashman, K. V., Sparks, R. S. J. & Blundy, J. D. (2017). Vertically extensive and unstable magmatic systems: A unified view of igneous processes. *Science* **355**.

Conrey, R. M., Bailey, D. G., Singer, J. W., Wagoner, L. J., Parfitt, B., Hay, J., Keh, O., Chang, Z. & Huang, S. (2023). Combined use of multiple external and internal standards in LA-ICP-MS analysis of bulk geological samples using lithium borate fused glass. *Geochemistry: Exploration, Environment, Analysis* geochem2023-001.

Conrey, R. M., Bailey, D. G., Singer, J., Wagoner, L., Parfitt, B., Hay, J. & Keh, O. (2019). Combined Use of Multiple Internal and External Standards in LA-ICPMS Analysis of Geologic Samples Using Lithium Borate Fused Glass. paper presented at the AGU Fall Meeting Abstracts **2019**, V11D-0106.

DeBari, S. M. & Greene, A. R. (2011). Vertical Stratification of Composition, Density, and Inferred Magmatic Processes in Exposed Arc Crustal Sections. *Arc-Continent Collision*. Berlin, Heidelberg: Springer Berlin Heidelberg, 121–144.

Eagar, K. C., Fouch, M. J., James, D. E. & Carlson, R. W. (2011). Crustal structure beneath the High Lava Plains of eastern Oregon and surrounding regions from receiver function analysis. *Journal of Geophysical Research* **116**, B02313.

Eaton, G. P. (1982). The Basin and Range Province: Origin and Tectonic Significance. *Annual Review of Earth and Planetary Sciences* **10**, 409–440.

Erdmann, S., Scaillet, B. & Kellett, D. A. (2010). Xenocryst assimilation and formation of peritectic crystals during magma contamination: An experimental study. *Journal of Volcanology and Geothermal Research* **198**, 355–367.

Fierstein, J., Hildreth, W. & Calvert, A. T. (2011). Eruptive history of South Sister, Oregon Cascades. *Journal of Volcanology and Geothermal Research* **207**, 145–179.

Ford, M. T., Grunder, A. L. & Duncan, R. A. (2013). Bimodal volcanism of the High Lava Plains and Northwestern Basin and Range of Oregon: Distribution and tectonic implications of age-progressive rhyolites: Age-Progressive Rhyolites of Oregon. *Geochemistry, Geophysics, Geosystems* **14**, 2836–2857.

Ginibre, C., Worner, G. & Kronz, A. (2007). Crystal Zoning as an Archive for Magma Evolution. *Elements* **3**, 261–266.

Green, N. L. & Harry, D. L. (1999). On the relationship between subducted slab age and arc basalt petrogenesis, Cascadia subduction system, North America. *Earth and Planetary Science Letters* **171**, 367–381.

Green, T. H. (1995). Significance of Nb/Ta as an indicator of geochemical processes in the crust-mantle system. *Chemical Geology* **120**, 347–359.

Hammond, P. E. (1979). A Tectonic Model for Evolution of the Cascade Range. 19.

Hildreth, W. (2007). *Quaternary Magmatism in the Cascades - Geologic Perspectives*. Professional Paper. United States Geological Survey.

Hildreth, W., Calvert, A. T. & Fierstein, J. (2012). *Geologic Map of Three Sisters Volcanic Cluster, Cascade Range, Oregon*. Scientific Investigations Map. United States Geological Survey.

Hodge, E. T. (1925). *Mount Multnomah: Ancient Ancestor of the Three Sisters*. University of Oregon.

Hughes, S. S. & Taylor, E. M. (1986). Geochemistry, petrogenesis, and tectonic implications of central High Cascade mafic platform lavas. *Geological Society of America Bulletin* **97**, 1024–1036.

Jarosewich, E., Nelen, J. A. & Norberg, J. A. (1980). Reference Samples for Electron Microprobe Analysis. *Geostandards Newsletter* **4**, 43–47.

Johnson, D. M., Hooper, P. R. & Conrey, R. M. (1999). XRF Analysis of Rocks and Minerals for Major and Trace Elements on a Single Low Dilution Li-tetraborate Fused Bead. *Advances in X-ray Analysis*.

Jordan, B. T., Grunder, A. L., Duncan, R. A. & Deino, A. L. (2004). Geochronology of age-progressive volcanism of the Oregon High Lava Plains: Implications for the plume interpretation of Yellowstone. *Journal of Geophysical Research* **109**.

Lisowski, M., McCaffrey, R., Wicks, C. W. & Dzurisin, D. (2021). Geodetic Constraints on a 25-year Magmatic Inflation Episode Near Three Sisters. *Journal of Geophysical Research: Solid Earth*.

Long, M. D. *et al.* (2012). Mantle dynamics beneath the Pacific Northwest and the generation of voluminous back-arc volcanism: MANTLE DYNAMICS BENEATH THE PNW. *Geochemistry, Geophysics, Geosystems* **13**, n/a-n/a.

Major, J. (2022). *Cascades Volcano Observatory Information Statement*. Hazards Notification System for Volcanoes. United States Geological Survey.

Marzocchi, W., Selva, J. & Jordan, T. H. (2021). A unified probabilistic framework for volcanic hazard and eruption forecasting. *Natural Hazards and Earth System Sciences* **21**, 3509–3517.

Mason, B. (1966). Pyrope, augite, and hornblende from Kakanui, New Zealand. *New Zealand Journal of Geology and Geophysics* **9**, 474–480.

Mason, B. & Allen, R. O. (1973). MINOR AND TRACE ELEMENTS IN AUGITE, HORNBLENDE, AND PYROPE MEGACRYSTS FROM KAKANUI, NEW ZELAND. *New Zealand Journal of Geology and Geophysics* **16**, 935–947.

Parker, D. F., Price, J. D., Brooks, C. B. & Ren, M. (2023). Contrasting magmatic evolutions of the Three Sister Volcanoes reflect increased heat flow, crustal melting and silicic magmatism in the Central Oregon Cascade Arc. *Chemical Geology* **618**, 121294.

Paton, C., Hellstrom, J., Paul, B., Woodhead, J. & Hergt, J. (2011). Iolite: Freeware for the visualisation and processing of mass spectrometric data. *Journal of Analytical Atomic Spectrometry* **26**, 2508.

Riddick, S. N. & Schmidt, D. A. (2011). Time-dependent changes in volcanic inflation rate near Three Sisters, Oregon, revealed by InSAR: THREE SISTERS TIME-DEPENDENT INFLATION. *Geochemistry, Geophysics, Geosystems* **12**, n/a-n/a.

Ruscitto, D. M., Wallace, P. J., Johnson, E. R., Kent, A. J. R. & Bindeman, I. N. (2010). Volatile contents of mafic magmas from cinder cones in the Central Oregon High Cascades: Implications for magma formation and mantle conditions in a hot arc. *Earth and Planetary Science Letters* **298**, 153–161.

Schmidt, M. E. & Grunder, A. L. (2009). The evolution of North Sister: A volcano shaped by extension and ice in the central Oregon Cascade Arc. *Geological Society of America Bulletin* **121**, 643–662.

Schmidt, M. E. & Grunder, A. L. (2011). Deep Mafic Roots to Arc Volcanoes: Mafic Recharge and Differentiation of Basaltic Andesite at North Sister Volcano, Oregon Cascades. *Journal of Petrology* **52**, 603–641.

Schmidt, M. E., Grunder, A. L. & Rowe, M. C. (2008). Segmentation of the Cascade Arc as indicated by Sr and Nd isotopic variation among diverse primitive basalts. *Earth and Planetary Science Letters* **266**, 166–181.

Shane, P. (2015). Contrasting plagioclase textures and geochemistry in response to magma dynamics in an intra-caldera rhyolite system, Okataina volcano. *Journal of Volcanology and Geothermal Research* **297**, 1–10.

Sherrod, D. R., Taylor, E. M., Ferns, M. L., Scott, W. E., Conrey, R. M. & Smith, G. A. (2004). *Geologic Map of the Bend 30- × 60- Minute Quadrangle, Central Oregon*. Geologic Investigations Series. United States Geological Survey, 49.

Stelten, M. E. & Cooper, K. M. (2012). Constraints on the nature of the subvolcanic reservoir at South Sister volcano, Oregon from U-series dating combined with sub-crystal trace-element analysis of plagioclase and zircon. *Earth and Planetary Science Letters* **313–314**, 1–11.

Stewart, D. B., Walker, G. W., Wright, T. L. & Fahey, J. J. (1966). Physical Properties of Calcic Labradorite from Lake County, Oregon. *American Mineralogist* **51**, 177–197.

Straub, S. M., Gomez-Tuena, A., Stuart, F. M., Zellmer, G. F., Espinasa-Perena, R., Cai, Y. & Iizuka, Y. (2011). Formation of hybrid arc andesites beneath thick continental crust. *Earth and Planetary Science Letters* **303**, 337–347.

Straub, S. M., LaGatta, A. B., Martin-Del Pozzo, A. L. & Langmuir, C. H. (2008). Evidence from high-Ni olivines for a hybridized peridotite/pyroxenite source for orogenic andesites from the central Mexican Volcanic Belt: ANDESITE PETROGENESIS IN CENTRAL MVB. *Geochemistry, Geophysics, Geosystems* **9**, n/a-n/a.

Streck, M. (2008). Mineral Textures and Zoning as Evidence for Open System Processes. *Reviews in Mineralogy and Geochemistry* **69**, 545–594.

Sun, S. & McDonough, W. F. (1989). Chemical and isotopic systematics of oceanic basalts: implications for mantle composition and processes. *Geological Society, London, Special Publications* **42**, 313–345.

Taylor, E. M. (1978). *Field Geology of S.W. Broken Top Quadrangle, Oregon*. Special Paper. Oregon State Department of Geology and Mineral Industries, 56.

Taylor, E. M. (1990). Volcanic history and tectonic development of the Central High Cascade Range, Oregon. *Journal of Geophysical Research* **95**, 19611–19622.

Waters, L. E., Andrews, B. J. & Frey, H. M. (2021). Daly Gaps at South Sister, Oregon, USA, generated via partial melting. *Contributions to Mineralogy and Petrology* **176**, 52.

Wells, R. E. & McCaffrey, R. (2013). Steady rotation of the Cascade arc. *Geology* **41**, 1027–1030.

Wicks, C. W., Dzurisin, D., Ingebritsen, S., Thatcher, W., Lu, Z. & Iverson, J. (2002). Magmatic activity beneath the quiescent Three Sisters volcanic center, central Oregon Cascade Range, USA. *Geophysical Research Letters* **29**, 1122.

Williams, H. (1944). *Volcanoes of the Three Sisters Region, Oregon Cascades*. University of California Press.

Wilson, D. S. (2002). The Juan de Fuca plate and slab: Isochron structure and Cenozoic plate motions. *The Cascadia Subduction Zone and Related Subduction Systems-Seismic Structure, Intraslab Earthquakes and Processes, and Earthquake Hazards: U.S. Geological Survey Open-File Report 02-328, and Geological Survey of Canada Open File 4350* (pp. 9–12). U.S. Geological Survey.

Zellmer, G. F., Sakamoto, N., Matsuda, N., Iizuka, Y., Moebis, A. & Yurimoto, H. (2016). On progress and rate of the peritectic reaction Fo + SiO2→ En in natural andesitic arc magmas. *Geochimica et Cosmochimica Acta* **185**, 383–393.

Appendix 1: Field Notes and Analytical Preparations

A1.1: Field Notes

A1.1.1: Field Methods

Sample collection was conducted primarily in the first week of August 2022, although collection of *mtp* was delayed by lightning storms. The *mtp* samples were collected on a follow-up expedition to just below the South Sister summit in September 2022. Unit locations and identities were verified at each sampling location using GPS data in concert with the map and associated unit descriptions of Hildreth et al. (2012). Outcrop-scale observations were made, along with field sketches and photographs detailing scale, fracture patterns, flow banding, quenched margins, and any other noteworthy features. Samples were taken from in-place rock wherever possible, with fresh faces being broken off and appraised for weathering extents to ensure high quality sample collection.

A1.2: Selection Criteria and Sample Preparation

In some cases, multiple samples were collected from different flows or deposits of the same unit; these display a certain measure of textural variability, especially evident when analyzed in thin section. A single candidate sample of each unit was chosen for thick section preparation and subsequent chemical analysis on the basis of containing minimally weathered mineral cargo most closely representative of the observed mineral distributions and abundances across all samples of the same unit. Samples were cut into billets roughly two cm by three cm by one cm thick and sent for professional preparation into thin sections (30 μm) and thick sections (100 μm). In total, nine thin sections and five thick sections were prepared. Thin sections were reserved for petrographic observation and characterization, while thick sections were used for quantitative analysis. Thicker samples were necessary to ensure that signals obtained via LA-ICP-MS (a destructive technique) were long enough for processing.

A1.2: Outcrop Descriptions and Sampling Locations

A1.2.1: Unit mnf

Unit mnf outcrops as a stack of at least four distinct, related lava flows cross-cut into a narrow step canyon by the subsequent erosion of North Fork Whychus Creek. The exposed portion of each flow is roughly 3 m thick, underlain by accumulated eroded debris forming a series of parallel benches stacking upwards from the ravine floor, roughly 15 m thick at its deepest visible point. Each flow is structurally similar, with a lowermost layer of agglutinated scoria and fallout debris covered in a midlayer of phenocrystic, vesicle-free, block jointed blackish grey lava. This is overlain by a massive upper layer of similar material, containing abundant irregular vesicles averaging two centimeters, with some voids as large as 15 cm. The scoria layer is heavily undercut near each successive knickpoint in the creek and obscured by eroded debris along the parallel benches making up the walls of the canyon. Given the similarity of each individual flow, only one sample (TSO-070) was collected for this outcrop, from the block-jointed midlayer of the uppermost flow, near the contact with overlying unit adl.

A1.2.2: Unit mnh

Unit mnh outcrops at two separate cliff faces, each one composed of multiple distinct lava flows that all share common eruptive origins, as determined by Hildreth et al. (2012). These outcrop at two cliff faces (*Figure A1.2.2*) which are buried on all sides amidst a thick layer of glacial debris, sloping down from the saddle between Middle Sister and North Sister just east of Black Hump, although it is likely overlain by nearby unit dbh (Hildreth et al. 2012). The lower exposure outcrops at roughly 2550 m, forming a northeast-facing cliff face roughly 40 m wide by 20 m tall at its thickest exposure, rounded towards the top and tapering into large, loose boulders and debris as its upper flow becomes increasingly fractured. The exposure comprises five separate lava flows. The lowermost four flows are texturally similar, each between one and three meters thick, and mostly obscured by debris, forming thin bands of bluish-grey, vesicle-free, massive rock weathered to a pale beige-tan. Each is bounded by an underlying layer of rust red, easily eroded agglutinated scoria. Only one sample, TSO-056, was collected from the fourth flow upsection, near the left-hand edge where neighboring debris meets the face. The lower margin of this flow is vesicular, punctuated with ~5% elongate, round voids up to three centimeters in length. These diminish upsection. The uppermost, fifth flow extends roughly 12 m vertically,

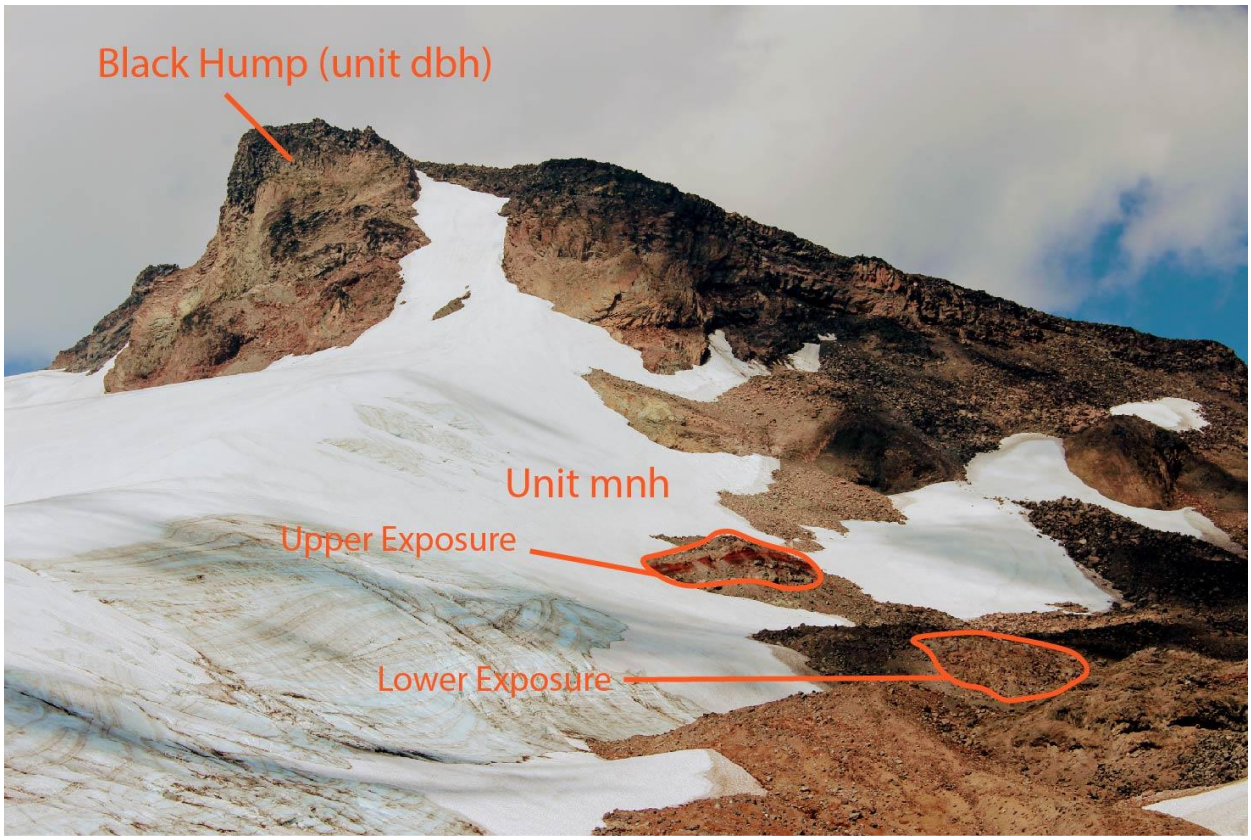

Figure A1.2.2: Location of mnh upper and lower exposures, relative to the more prominent Black Hump, between the Middle Sister and North Sister summits and immediately north of Hayden Glacier.

weathered a similar dusty tan, with blocky fracture worsening upwards up to an indistinct rubbly contact with the accumulated debris directly upslope.

The *mnh* upper exposure is located ~100 m upslope, just below the northern margin of Hayden Glacier, descending from the northeast flank of the Middle Sister summit. Roughly 35 m wide by 15 m tall, three distinct flows are exposed here, again punctuated by thick underlying layers of associated agglutinated scoria bearing a bright rusty color which makes the outcrop easy to spot from a distance. Moving upsection, the very lowest edge exposed above the apron of glacial debris is a 1 m pile of scoria, overlain by a medium grey, massive, minimally weathered lava flow (flow 1) up to five meters thick, with sparse vesicles (<1%) up to 2 mm in diameter that are often found clustered together. Sample TSO-054.1 was collected from the middle of flow 1 near its thickest point. Above this, roughly 2 m of coarse, burgundy red scoria separates the next flow. Flow 2 is 1 m thick and is similar in color and texture to the underlying flow 1, albeit with larger, more abundant vesicles (~6%; up to 8 mm; irregular). Flow 2 exhibits blocky fracture into roughly one-meter cubes, from which sample TSO-054.2 was obtained. Above flow 2, a thick pile of agglutinated tephra varies from 3 to 5 m thick, with coarse, burgundy red material at the bottom, grading upwards into finer, rust red, "popcorn" like tephra with bands of pale golden yellow. Above the banded tephra, barely preserved at the glacially rounded upper edge of the outcrop, exist remnants of a third, thin lava flow (flow 3), not noted by Hildreth et al. (2012). Flow 3 is heavily weathered with "zebra-stripe" swirls and bands of highly altered material amidst dusty medium grey, extremely fine-grained solid rock which contains scant small (~5 cm) lithic inclusions. Although far too weathered for chemical analysis, sample TSO-054.3 was collected for the sake of comparison from near the base of the flow.

A1.2.3: Unit mtp

The final summit-capping eruption from the main South Sister summit vent complex is unit *mtp,* which mantles the underlying unit *aeg*. Unit mtp forms a thin, draping layer of agglutinated scoria and overlying airfall deposits around the ~700 m-wide summit crater, and dips to the southwest in a thin, tapering lobe that extends down to about 2800 m. The unit measures up to 20 m at its thickest points, exposed where erosion has reduced the edge of the deposit into cliff faces directly up to the crater rim on the northern and eastern sides, which grade from densely welded, rheomorphic deposits up to tack welded agglutinates, finally to loosely accumulated airfall at the surface and more distal reaches (Hildreth et al. 2012). Due to hiker traffic, altitude, and exposure, samples TSO-080 and TSO-081 were discretely collected from steeply sloping airfall fields above the mapped contact with *aeg*, amidst a variety of material including solid ejecta weathered to a clayey pink, beige breadcrust bombs, and highly vesicular rust-colored scoria. Lacking safely accessible in-place rock, a representative variety of loose material present was collected to ensure correct identification and collection of true *mtp* airfall.

A1.3: Sample Descriptions

A1.3.1: TSO-070 (mnf) [44.147564, -121.736494; elev. 1930 m]

TSO-070 was sampled from the blocky, jointed midlayer of the mnf upper flow, with a dusty beige exterior and rich, dark grey fresh faces. Scant small vesicles comprise 1-3% of the sample, ranging from 0.5–4 mm, although these increase in size and abundance closer to the top of the flow. The internal material of the sample is well preserved and minimally weathered, with a finely microcrystalline groundmass, internally consistent and coarsely porphyritic, containing ~10% visible phenocrysts. Visible plagioclase makes up roughly 9% of the sample, appearing as either large (1–3 mm), boxy phenocrysts or distinct small (<1 millimeter) elongate laths. Larger phenocrysts are occasionally found in clots up to 3 mm, with rare (<1%), granular olivine and orthopyroxene (≤1%) less than 1 mm. Scant, miniscule oxide flecks occur throughout the sample.

Figure A1.3.1: Representative TSO-070 hand sample.

A1.3.2: TSO-054.1 (mnh) [44.155585, -121.776906; elev. 2599 m]

The lowest flow of the mnh upper exposure yielded dense samples. The in-place rock of the outcrop is very strong, with minimal fracturing and seemingly unweathered interiors. Exterior faces show a slight reddish-brown discoloration, but any weathering rind is minimal. Vesicles are no greater than 2 mm, found clustered together in small bands, making up ~1% of the sample. Otherwise, TSO-054.1 is internally consistent and moderately porphyritic, with a bluish grey, finely microcrystalline ground mass enclosing ~12% visible phenocrysts. Plagioclase is most abundant (~10%), with a few large, boxy phenocrysts and clots as large as 2 mm, and the majority being finer, elongate laths. Occasional equant, granular olivine (~2%) range as large as 1 mm and are found in several large (up to 6 millimeter) olivine-dominated clots. Pyroxenes are not observed in hand sample, and oxides are too small to identify under hand lens.

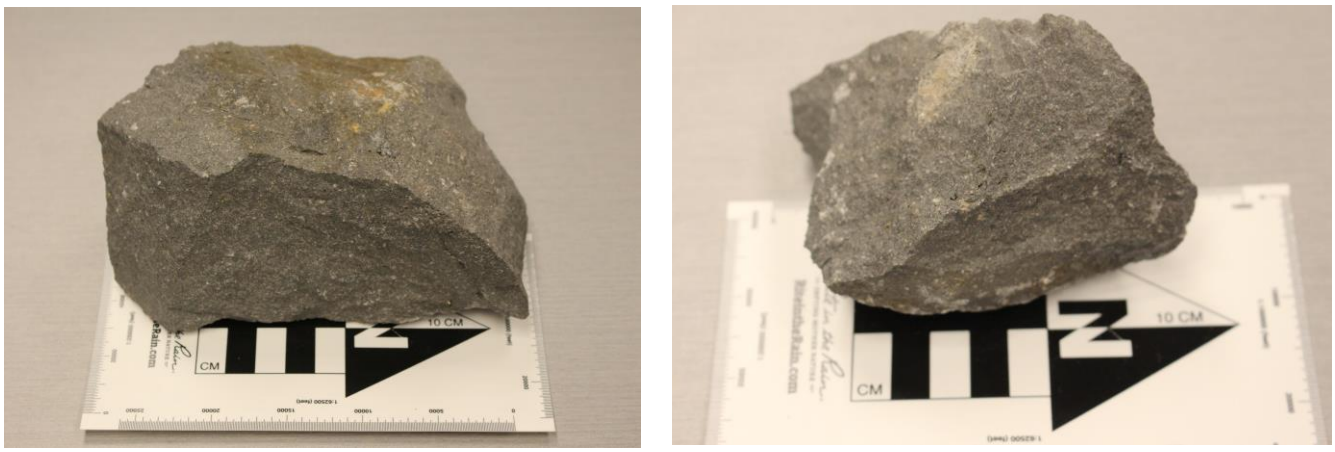

Figure A1.3.2: Representative TSO-054.1 hand sample.

A1.3.3: TSO-054.2 (mnh) [44.155565, -121.776952; elev. 2603 m]

TSO-054.2 is altogether similar to TSO-054.1, with slightly poorer preservation and a higher proportion of vesicles. It has an olive drab to dusty beige color on weathered faces, and a slightly paler medium bluish grey on the interior. Occasional larger vesicles range from 0.5 mm spheres to 8 mm irregular voids (~6%), unevenly distributed throughout the sample. It is moderately porphyritic, with up to 10% phenocrysts. Mineral distributions are similar to TSO-054.1, although olivine clots are rarer and tend to be no larger than 3 mm. Some chunks bear round, swirled inclusions of dark burgundy-black, foamy or spongy scoria, resembling the tephra of the underlying agglutinate, which has been mixed into the flow. These bear ~60% vesicles up to 4 mm and only 6% phenocrysts.

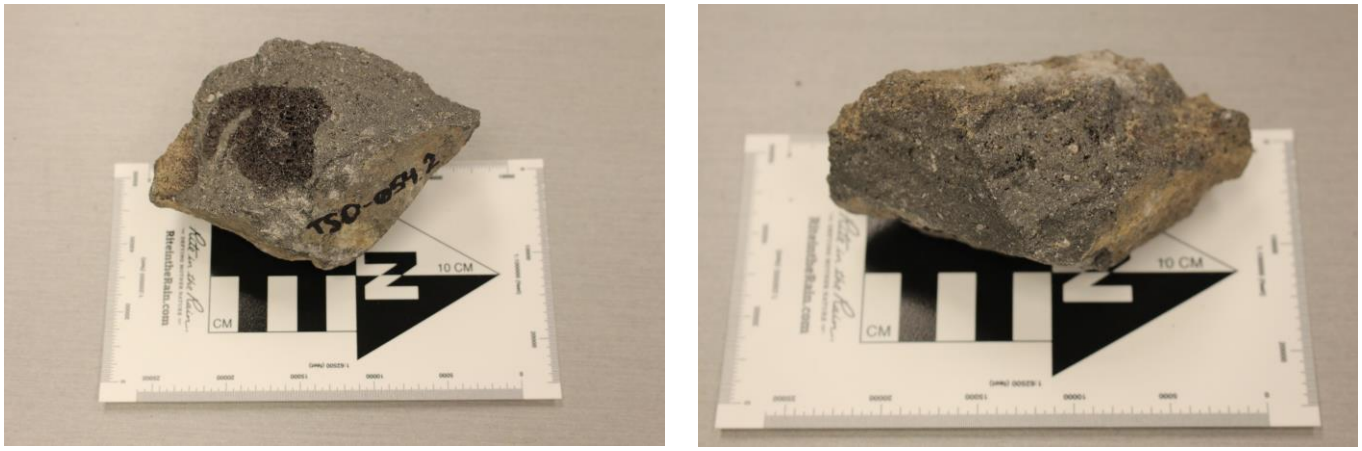

Figure A1.3.3: Representative TSO-054.2 hand sample.

A1.3.4: TSO-054.3 (mnh) [44.155549, -121.777007; elev. 2608 m]

Glacial polish on the rounded upper surface of the outcrop made sampling this uppermost flow difficult. The entire flow is pervasively weathered to a dull clayey rust-red inside and out, with irregular, thin (3–20 mm) "zebra-stripe" bands and lenses of dark grey, unaltered rock (comprising ~35% total) bearing an exceptionally fine ground mass. This fine-grained component contains ~5% plagioclase phenocrysts no larger than 1 millimeter, as well as 3% spherical vesicles up to 2 mm. The weathered, rust-red regions are vug-riddled and contain occasional, porous clusters of vesicles ranging from 2 to 16 mm in diameter. Occasional lithic inclusions are observed as pale grey, angular, and more coarsely microcrystalline regions enclosed within the host rock, containing plagioclase and <<0.5 mm fragmental olivine.

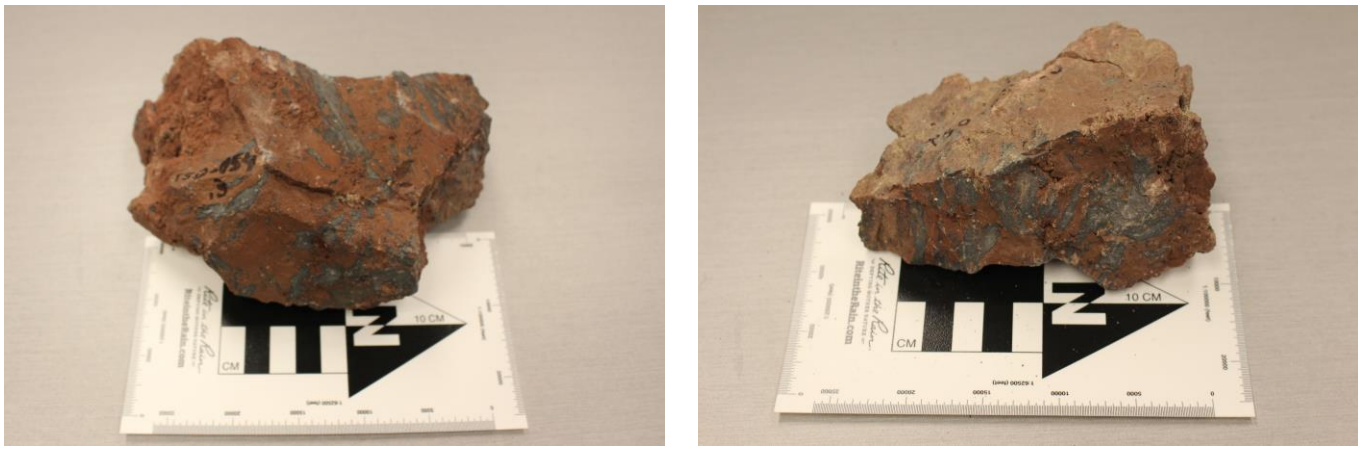

Figure A1.3.4: Representative TSO-054.3 hand sample.

A1.3.5: TSO-056 (mnh) [44.155488, -121.775135; elev. 2546 m]

TSO-056 was collected from the fourth flow of the lower mnh exposure, where rounded, elongated vesicles are common, ranging up to 3 cm in length (~5% at sampling location). The sample is a deep bluish grey on fresh faces, with weathered faces ranging from dirty beige to a rusty burgundy red. The rock is coarsely hypocrystalline with an intersertal porphyritic texture, as nearly the entire sample is composed of plagioclase crystals larger than 0.1 mm, with small amounts of opaque, oxide-rich interstitial glass. Equant, euhedral to subhedral olivine ranging up to 1 mm in diameter make up ~3%. Plagioclase phenocrysts visible to the naked eye average roughly 2 mm, making up ~10% of the sample. The rock is dense, with well preserved and minimally weathered material within.

Figure A1.3.5: Representative TSO-056 hand sample.

A1.3.6: TSO-080 (mtp) [44.096455, -121.772013; elev. 2899 m]

Sampled upslope from the aeg contact, TSO-080 represents scoriaceous airfall typical of the unwelded south-dipping lobe of mtp. The sample was chosen as the densest, least weathered piece found in a broad, loose slope of vesicular, rust-red debris ranging up to ~30 cm. It is highly vesicular (30–45%) with irregular, rounded voids ranging up to 9 mm, averaging roughly 1.5 mm. The interior is minimally weathered, blackish grey, and finely microcrystalline, forming a network of vesicle walls entrapping roughly 17% phenocrysts– predominantly elongate to chunky plagioclase ranging up to 3 mm, as well as minor (~2%) olivine and pyroxenes, indistinct in hand sample but prevalent in thin section. A weathering rind roughly 1 cm thick extends from the reddish-orange exterior of the sample.

Figure A1.3.6: Representative TSO-080 hand sample.

A1.3.7: TSO-081 (mtp) [44.096923, -121.772117; elev. 2924 m]

Taken from loose material further upslope along the lower *mtp* airfall lobe, this sample represents the denser lava bombs found alongside the scoriaceous ejecta littered downslope of the summit crater. Solid and almost entirely avesicular, the rock is finely microcrystalline with roughly 5% plagioclase phenocrysts, mostly needle-like laths ≤1 mm in length, plus occasional (1%) highly degraded, granular olivine. Although denser than TSO-080, its rusty salmon-pink weathering rind extends farther into the sample, with apparent alteration as well as lichen growth penetrating along deep-running cracks throughout the sample.

Figure A1.3.7: Representative TSO-081 hand sample.

A1.4: Petrographic Variation Between mnh Samples

Mineralogically speaking, samples TSO-054.1, TSO-054.2, and TSO-056 all carry similar mineral cargoes. In thin section, similar distributions of minerals are found in each, with all three samples sharing comparable suites of plagioclase textures, proportionally subordinate olivine, and a similar scarcity of pyroxenes. Singular crystals of orthopyroxene and clinopyroxene were observed in a small subset of the thin sections prepared from these samples, although these are so scarce as to make meaningful chemical analysis impossible. Texturally speaking, TSO-056 is substantially more coarsely crystalline than the others and is the only sample with significant proportions of interstitial glass, alongside more abundant vesicles.

Sample TSO-054.3, on the other hand, does differ significantly. Aside from its extensive rust-red weathering, jagged-edged lithic inclusions, and uniquely fine-grained groundmass, it exhibits unfamiliar mineralogy in thin section; clinopyroxene is observed more commonly in clots, and plagioclase is only observed as subhedral, unsieved, and faintly oscillatory-zoned laths, with little textural variation. It is possible that this uppermost flow of the *mnh* upper outcrop represents a separate eruptive event, although it is not described by Hildreth et al. (2012) and is likely too heavily altered to study in depth.

Appendix 2: EMPA Standards Calibration

See Supplementary Data

Appendix 3: Bulk Chemical Data

See Supplementary Data

Appendix 4: Major Element Geochemistry

See Supplementary Data

Appendix 5: Crystals Analyzed

BSE images of all crystals analyzed for this investigation follow, organized by population as indicated in headings. Black circles indicate EMPA sampling locations (spot sizes not to scale), with the accompanying number indicating anorthite contents for plagioclase, forsterite contents for olivine, and magnesium number for pyroxene. See Supplementary Data for accessible source data for each crystal.

A5.1: Unit mnf

A5.1.1: mnf-PL1

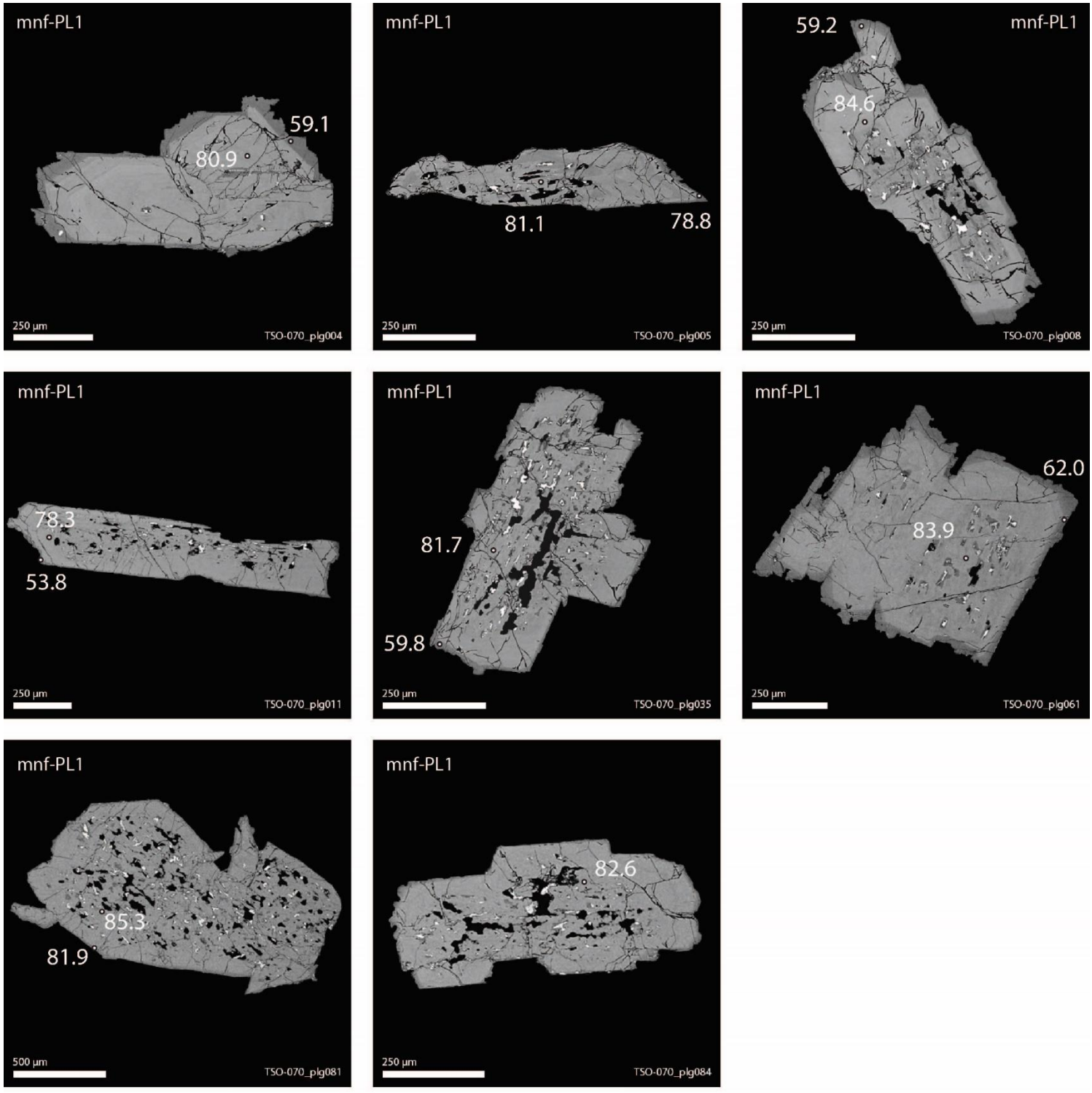

A5.1.2: mnf-PL2A

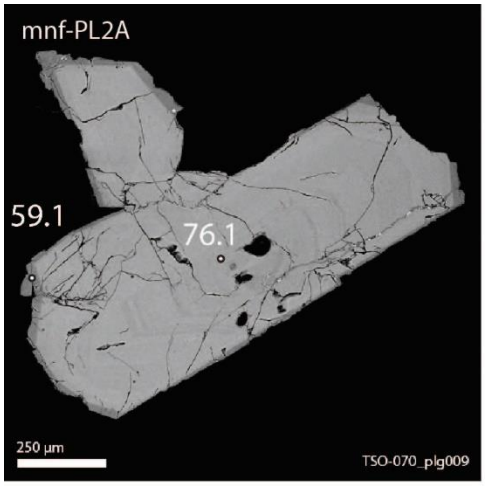

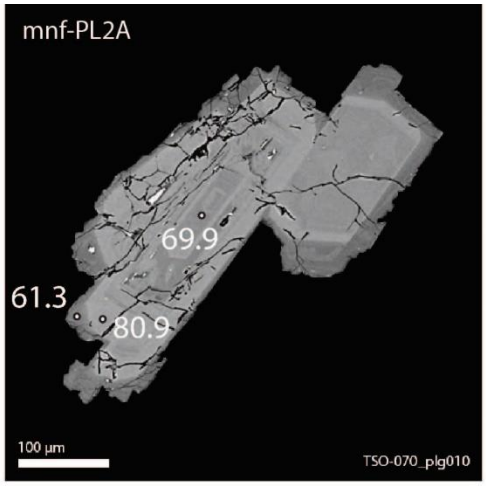

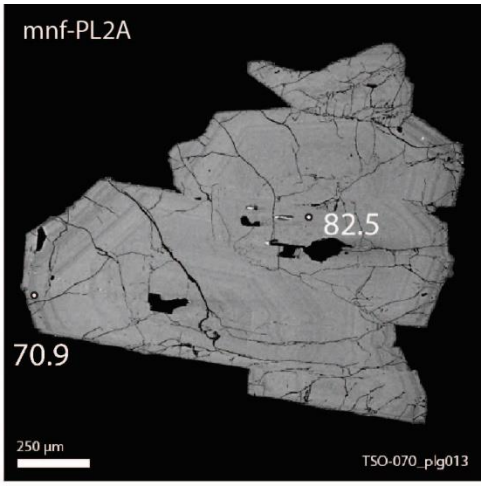

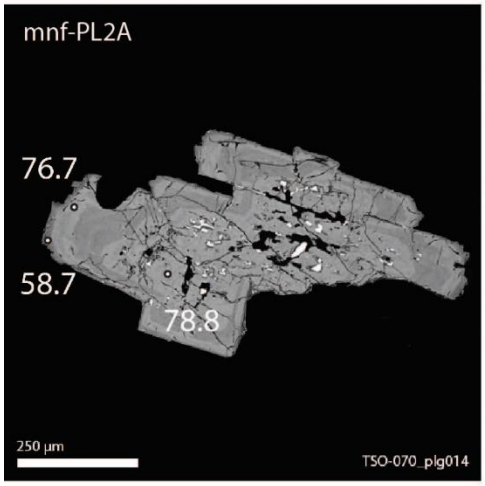

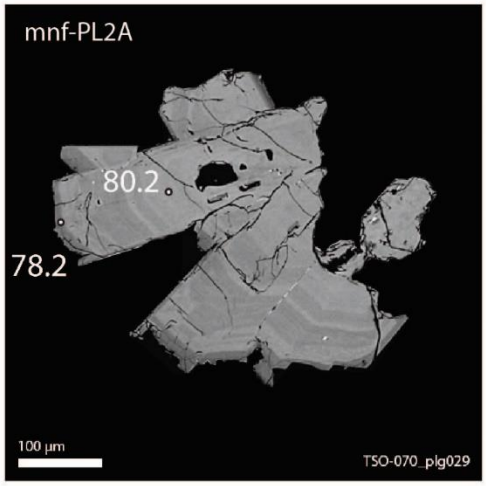

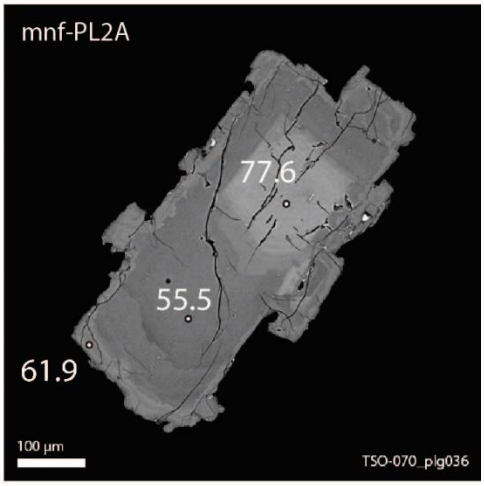

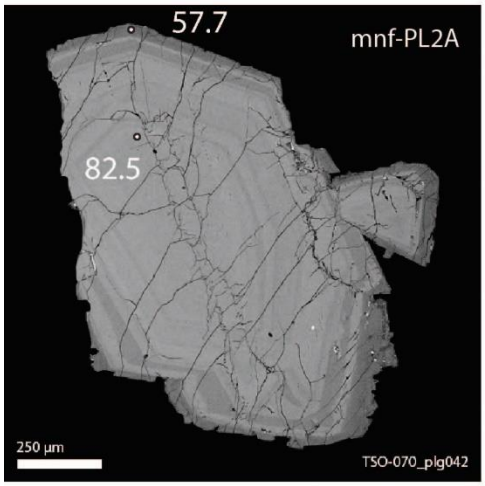

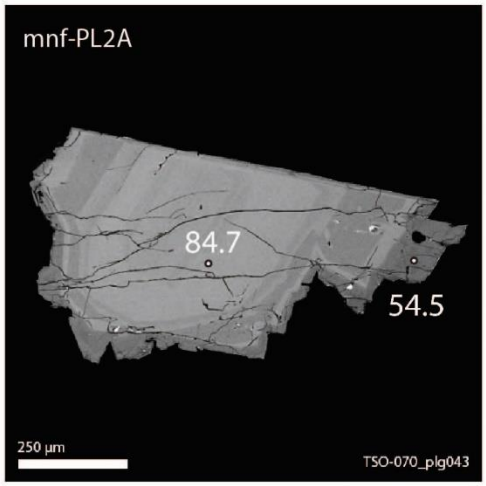

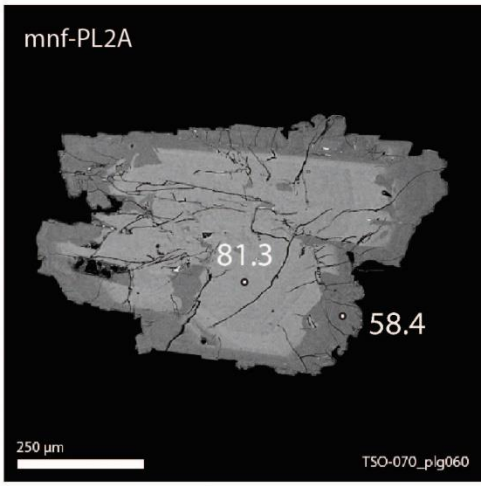

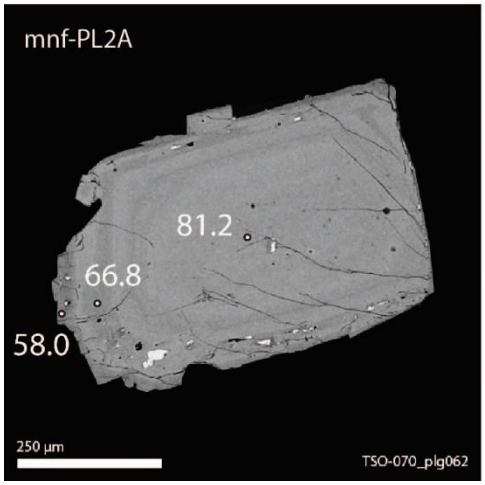
mnf-PL2A
81.2
66.8
58.0
250 µm
TSO-070_plg062

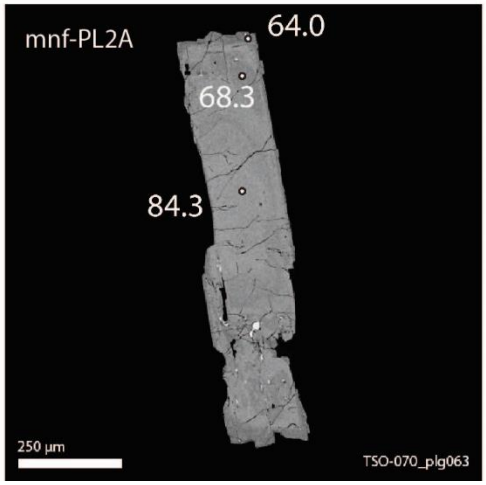
mnf-PL2A
64.0
68.3
84.3
250 µm
TSO-070_plg063

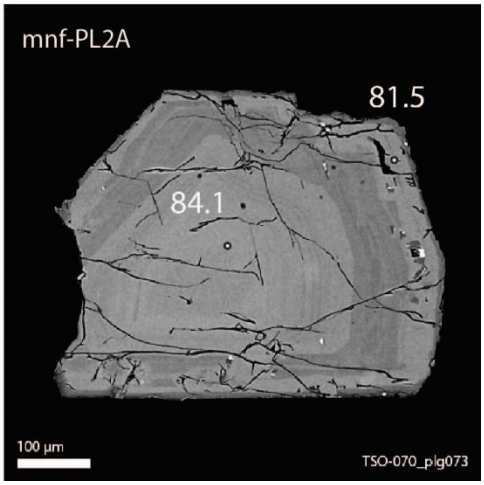
mnf-PL2A
81.5
84.1
100 µm
TSO-070_plg073

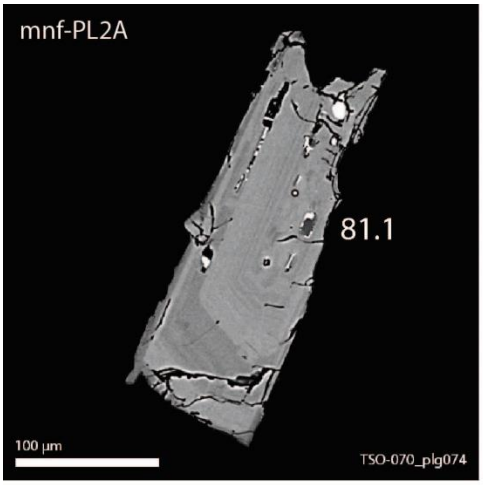
mnf-PL2A
81.1
100 µm
TSO-070_plg074

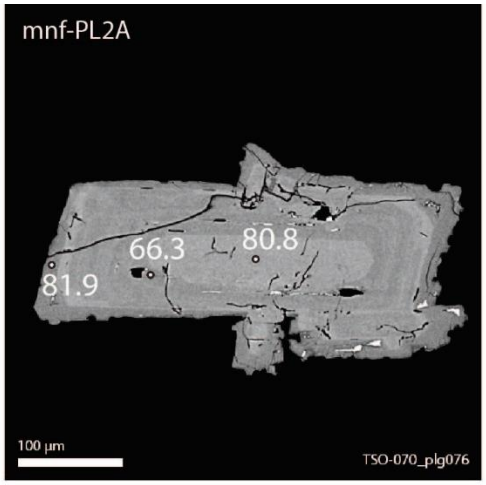
mnf-PL2A
66.3
80.8
81.9
100 µm
TSO-070_plg076

A5.1.3: mnf-PL2B

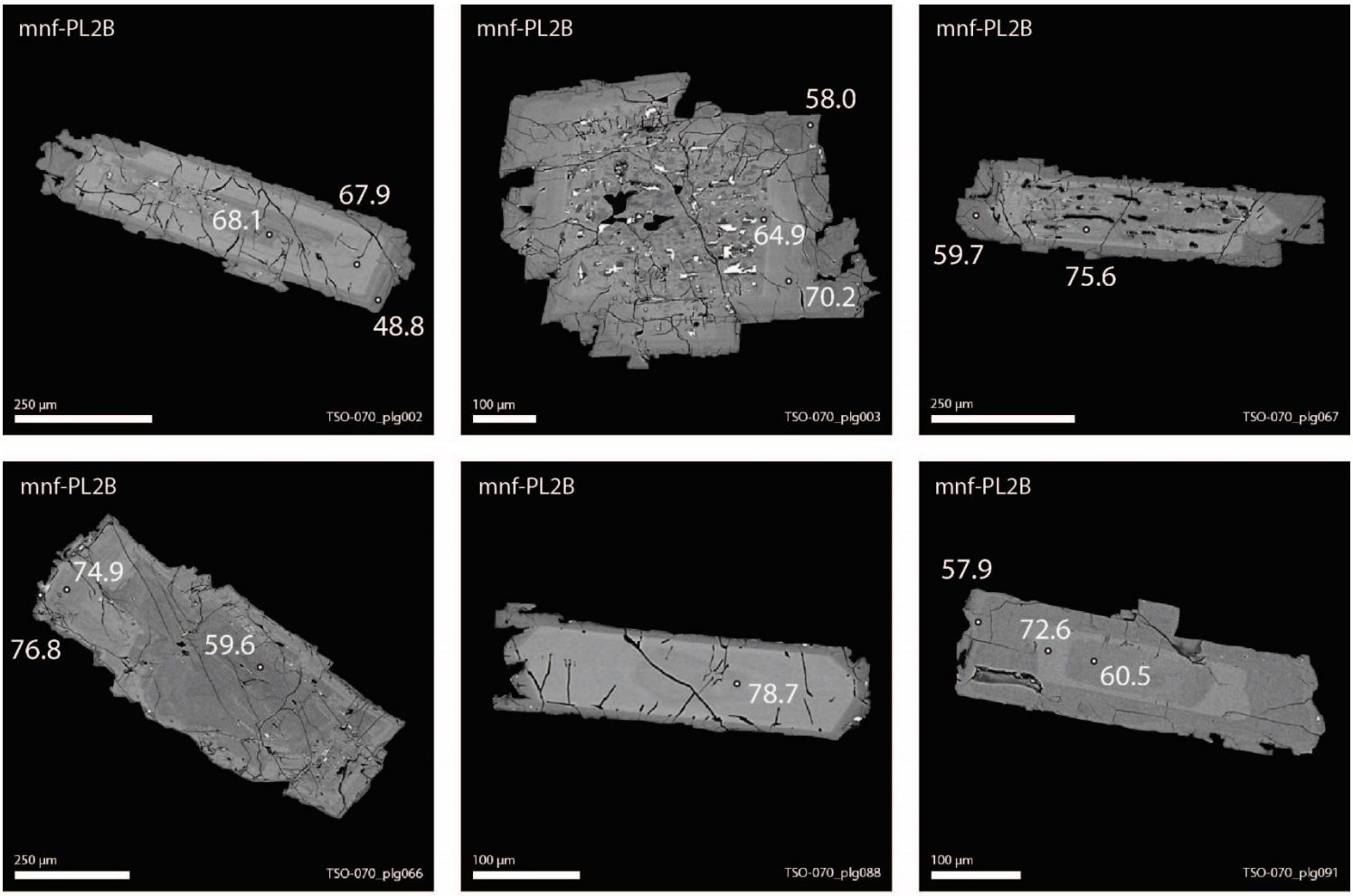

A5.1.4: mnf-OLV1

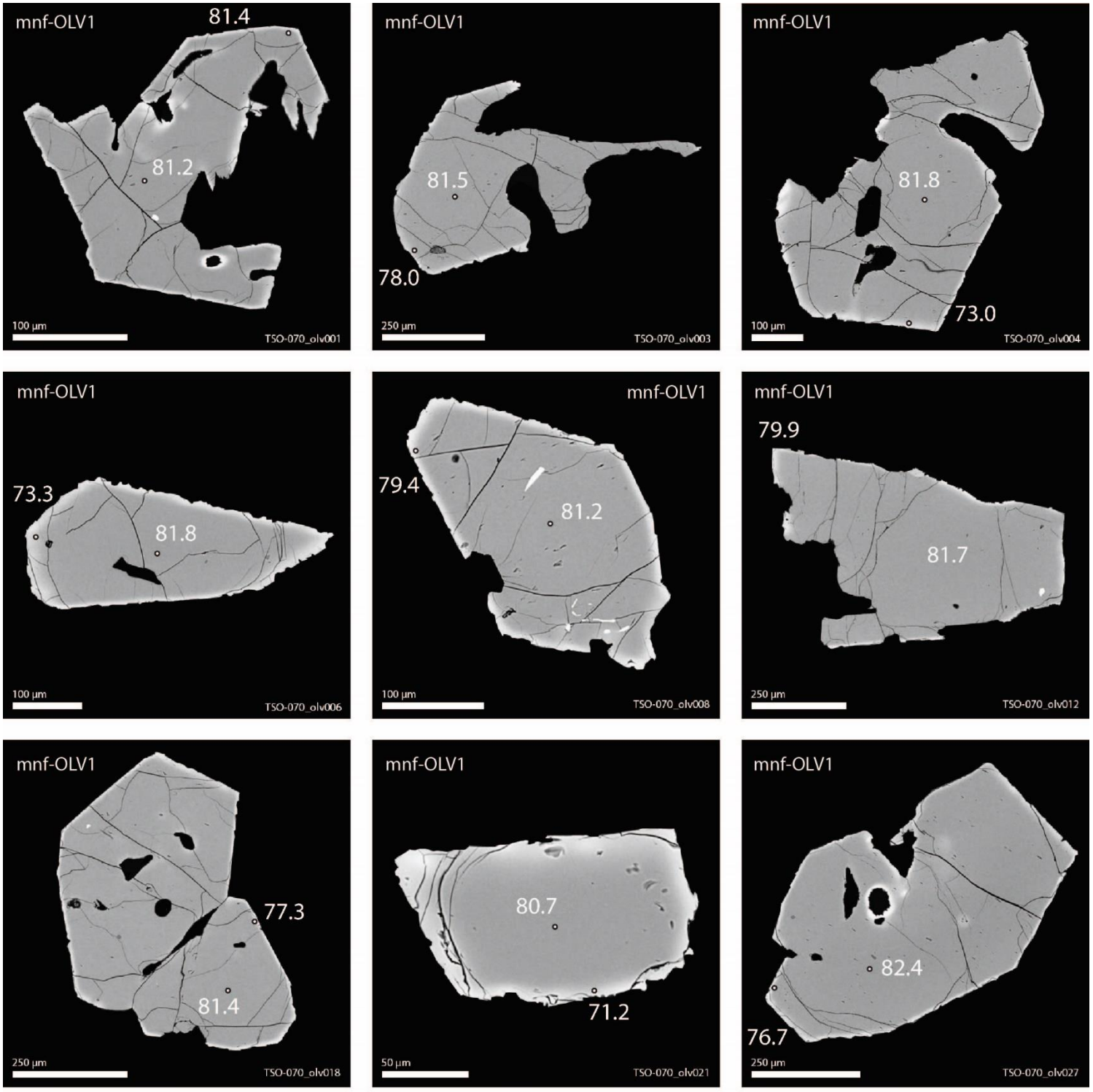

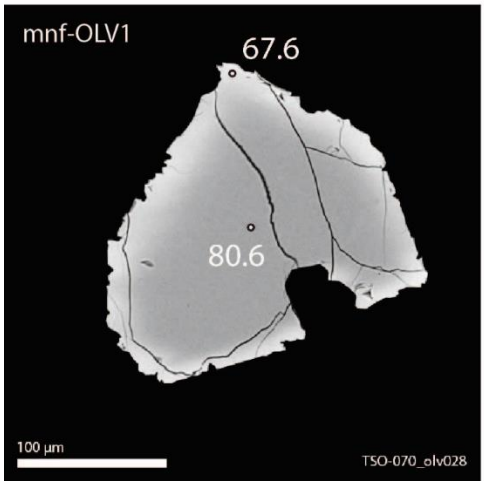
mnf-OLV1
67.6
80.6
100 µm
TSO-070_olv028

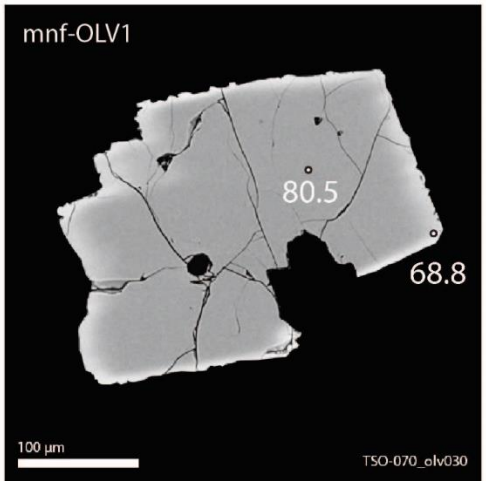
mnf-OLV1
80.5
68.8
100 µm
TSO-070_olv030

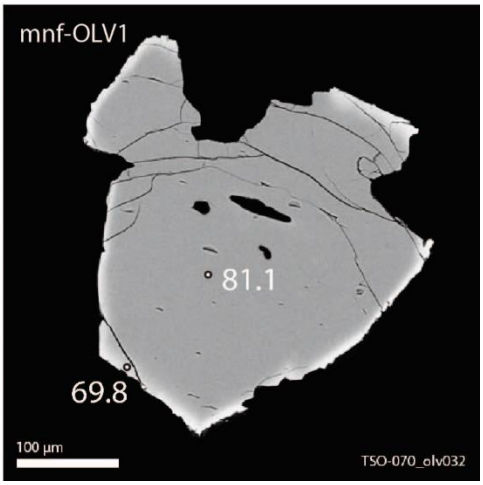
mnf-OLV1
81.1
69.8
100 µm
TSO-070_olv032

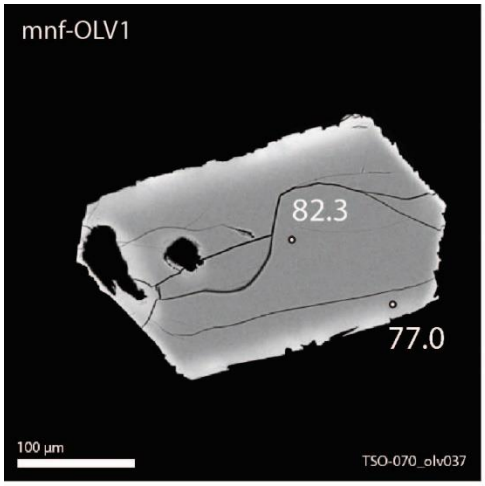
mnf-OLV1
82.3
77.0
100 µm
TSO-070_olv037

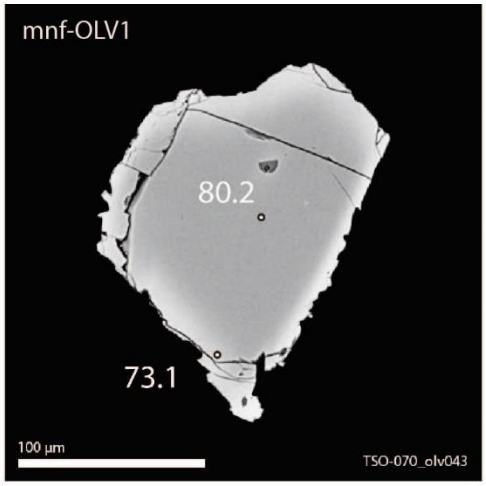
mnf-OLV1
80.2
73.1
100 µm
TSO-070_olv043

A5.1.4: mnf-OLV2

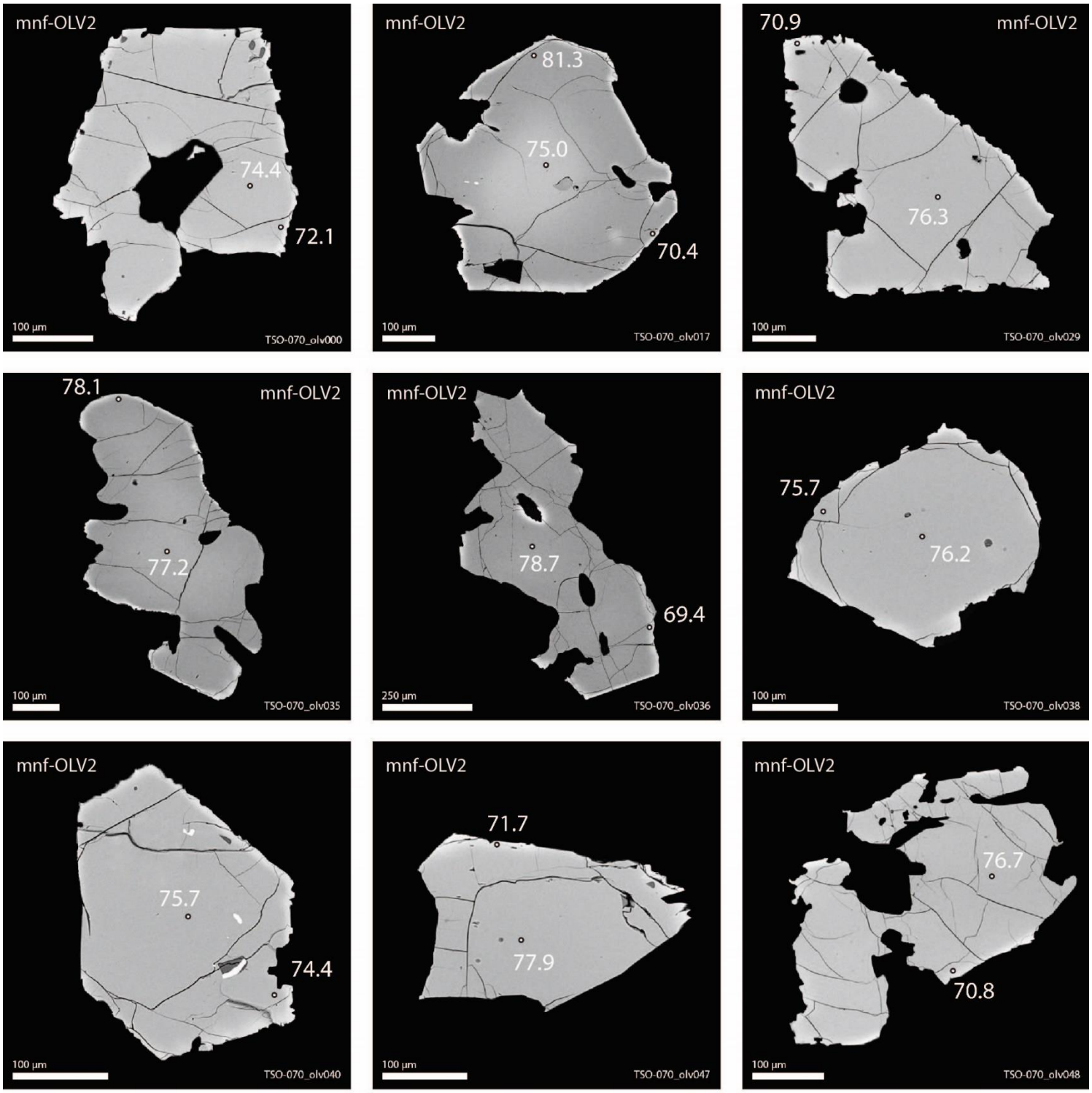

A5.1.5: mnf-OLV/PLG-MISC

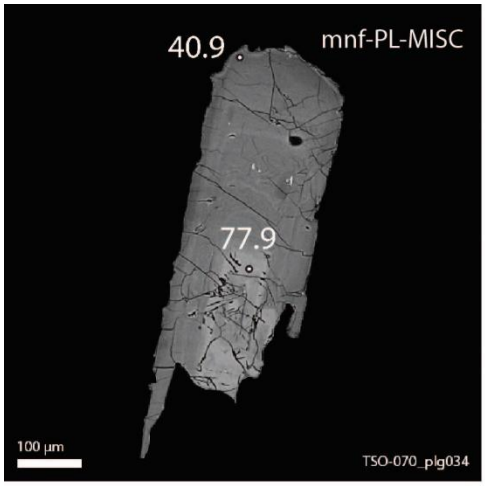

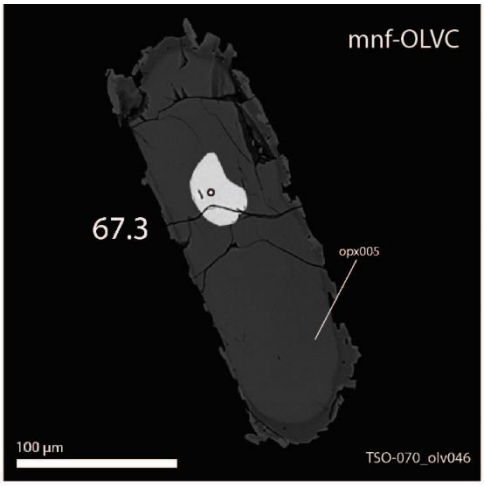

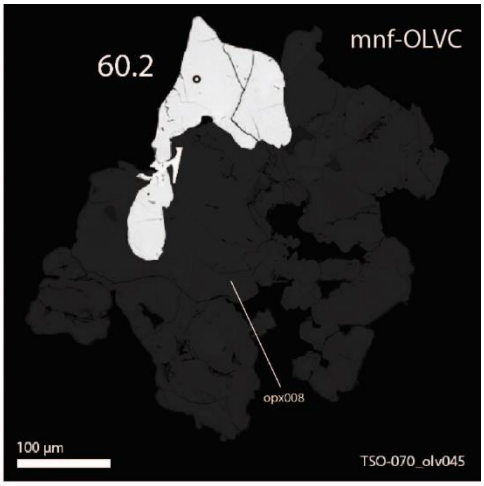

A5.1.6: mnf-OPX1A

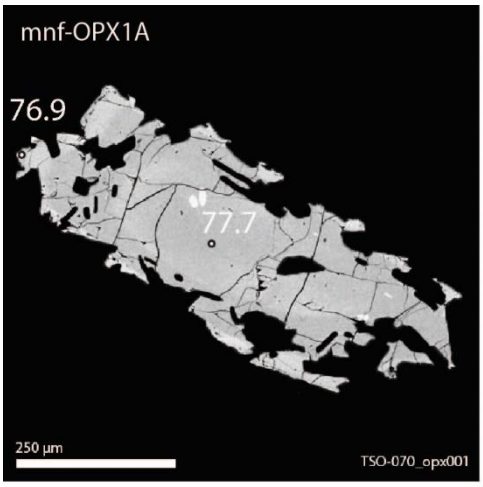

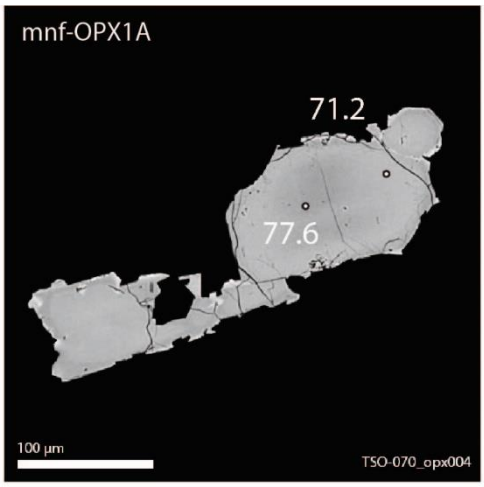

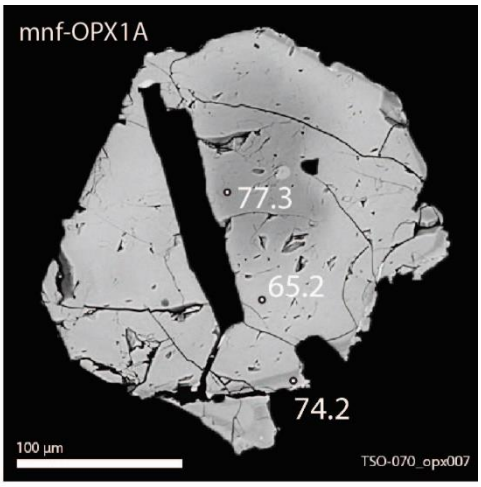

A5.1.7: mnf-OPX1B

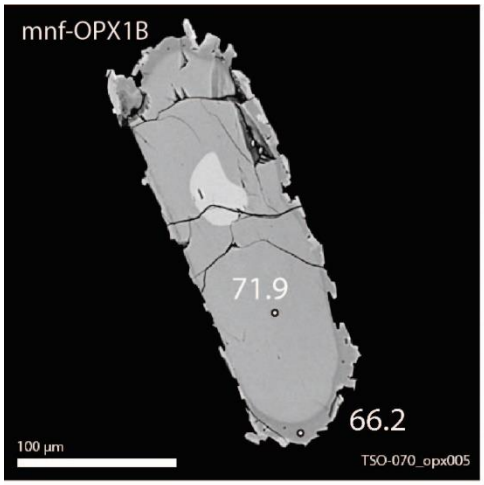

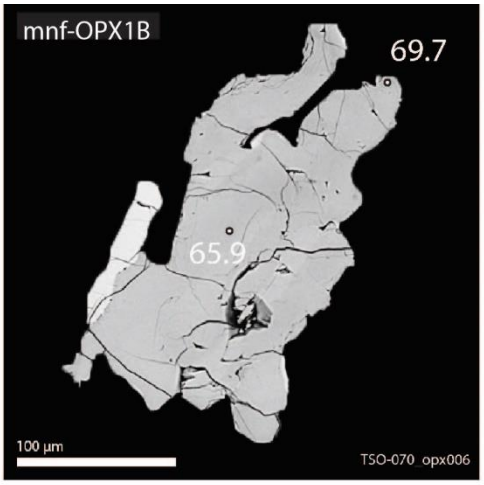

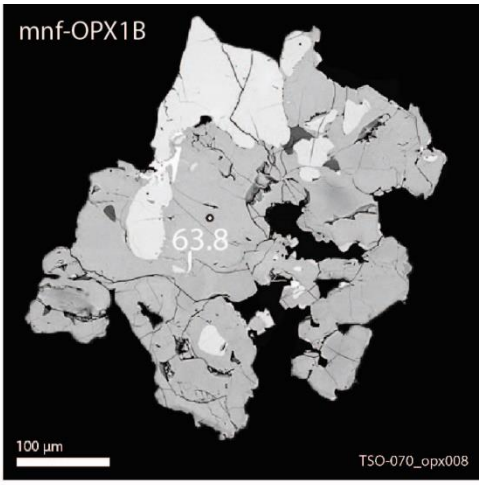

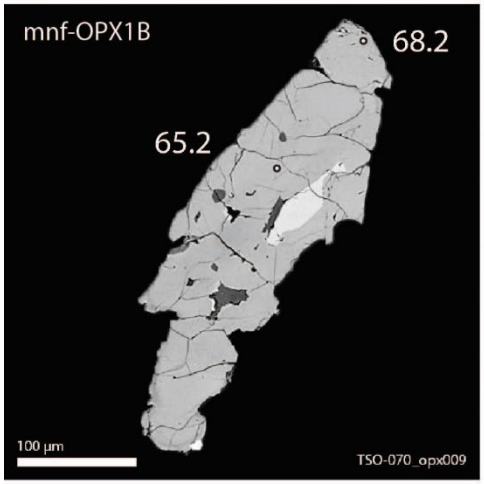

A5.2: Unit mnh

A5.2.1: mnh-PL1A

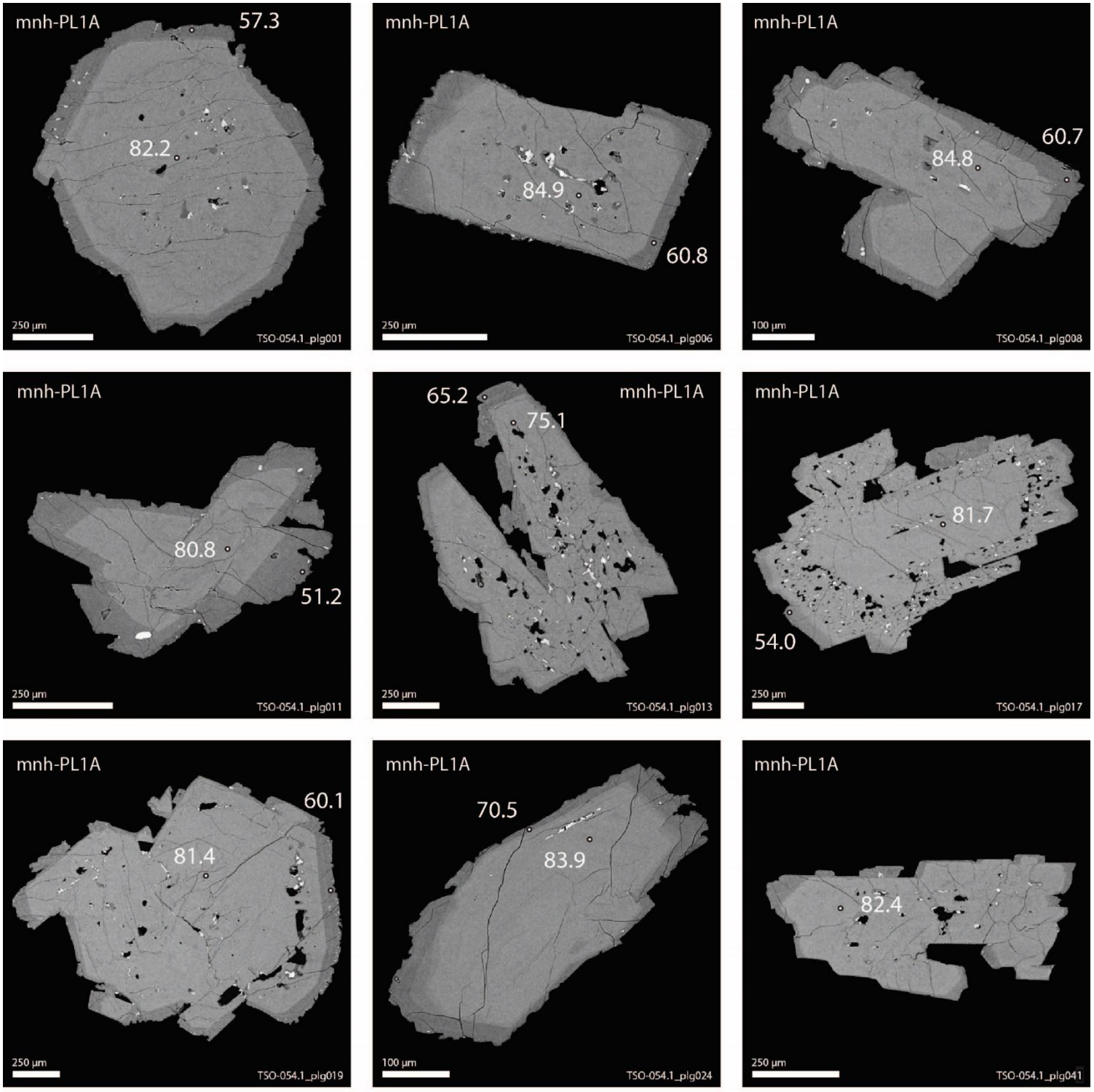

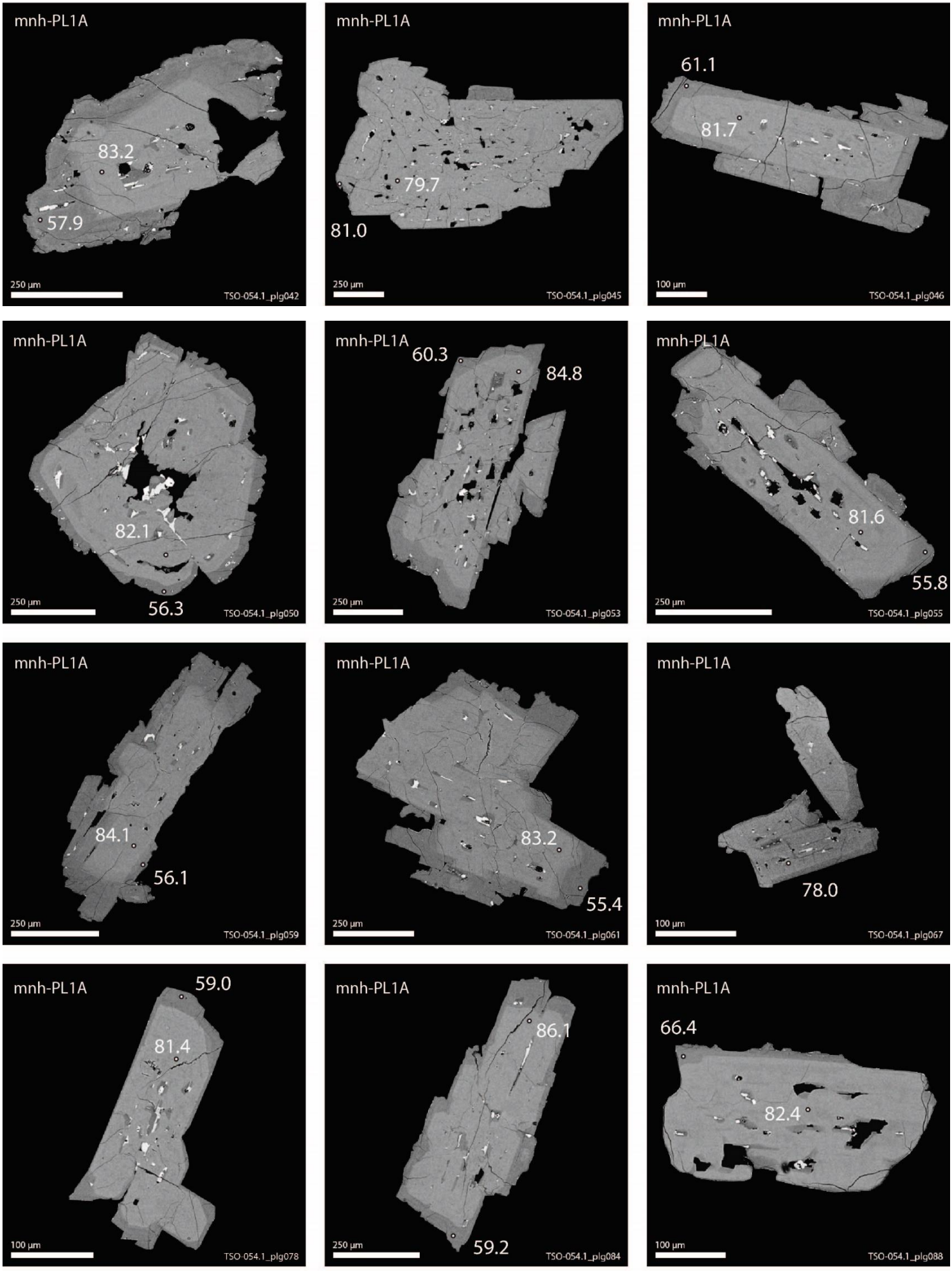
mnh-PL1A
83.2
57.9
250 µm
TSO-054.1_plg042
mnh-PL1A
79.7
81.0
250 µm
TSO-054.1_plg045
mnh-PL1A
61.1
81.7
100 µm
TSO-054.1_plg046
mnh-PL1A
82.1
56.3
250 µm
TSO-054.1_plg050
mnh-PL1A
60.3
84.8
250 µm
TSO-054.1_plg053
mnh-PL1A
81.6
55.8
250 µm
TSO-054.1_plg055
mnh-PL1A
84.1
56.1
250 µm
TSO-054.1_plg059
mnh-PL1A
83.2
55.4
250 µm
TSO-054.1_plg061
mnh-PL1A
78.0
100 µm
TSO-054.1_plg067
mnh-PL1A
59.0
81.4
100 µm
TSO-054.1_plg078
mnh-PL1A
86.1
59.2
250 µm
TSO-054.1_plg084
mnh-PL1A
66.4
82.4
100 µm
TSO-054.1_plg088

A5.2.2: mnh-PL1B

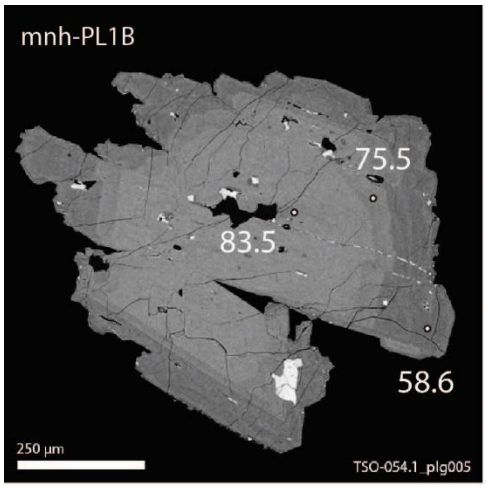

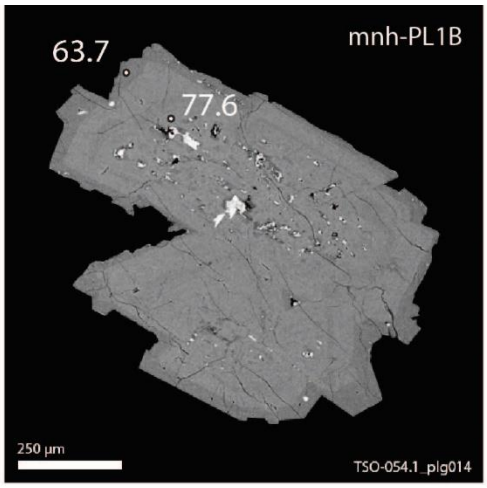

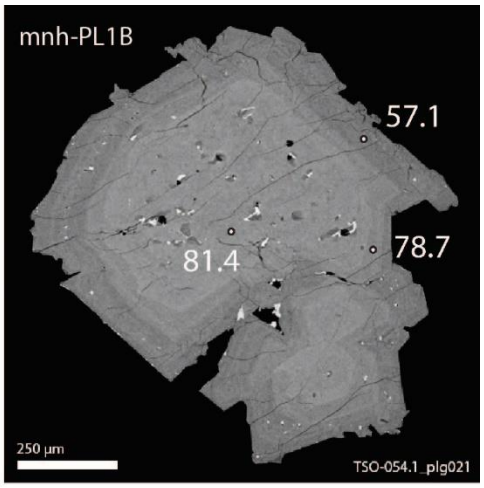

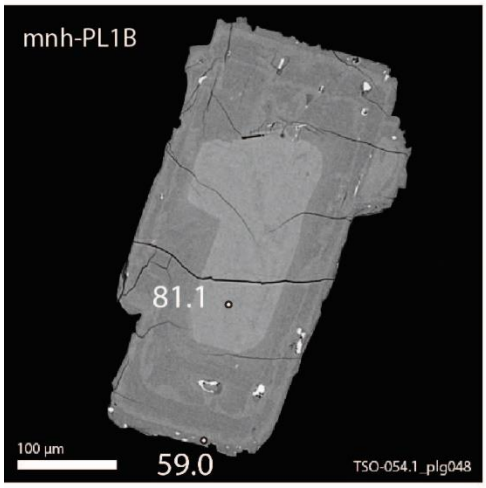

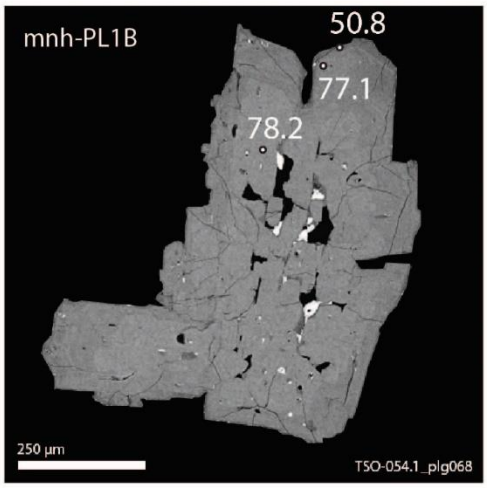

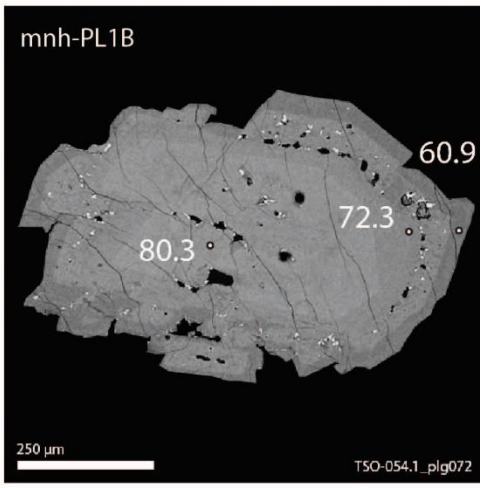

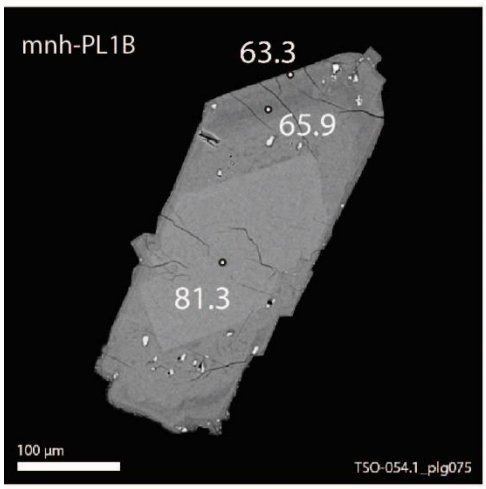

A5.2.3: mnh-OLV1

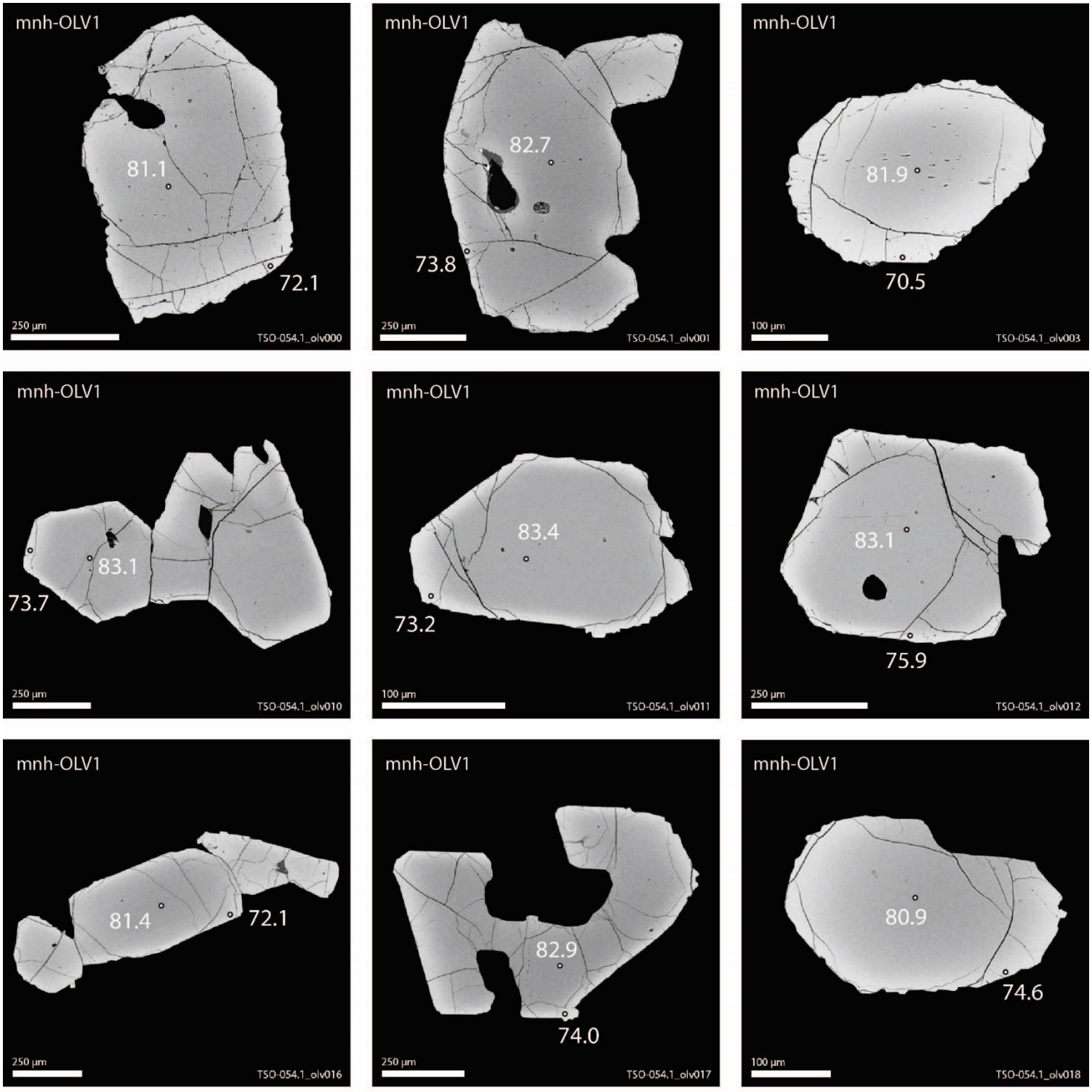

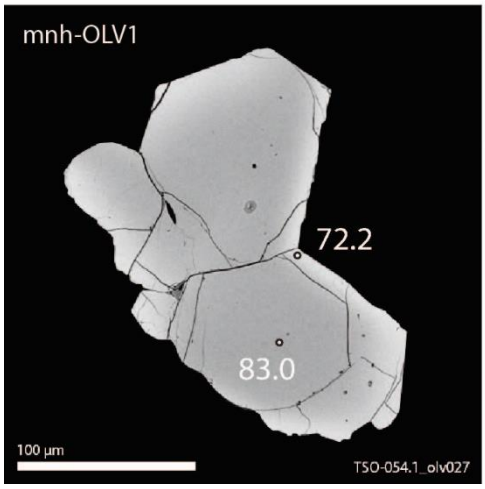
mnh-OLV1
72.2
83.0
100 µm
TSO-054.1_olv027

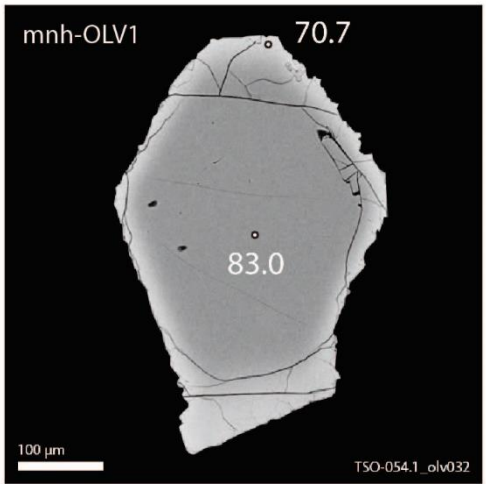
mnh-OLV1
70.7
83.0
100 µm
TSO-054.1_olv032

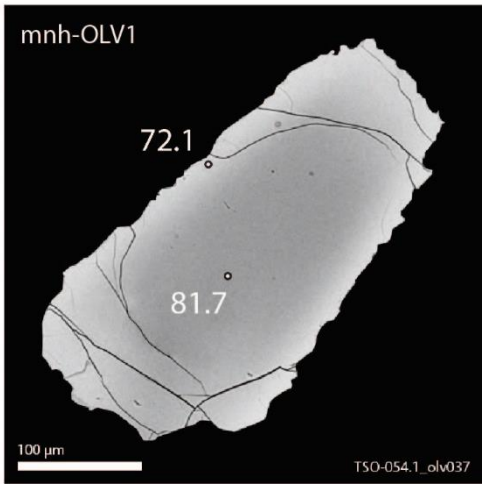
mnh-OLV1
72.1
81.7
100 µm
TSO-054.1_olv037

A5.2.4: mnh-OLV2

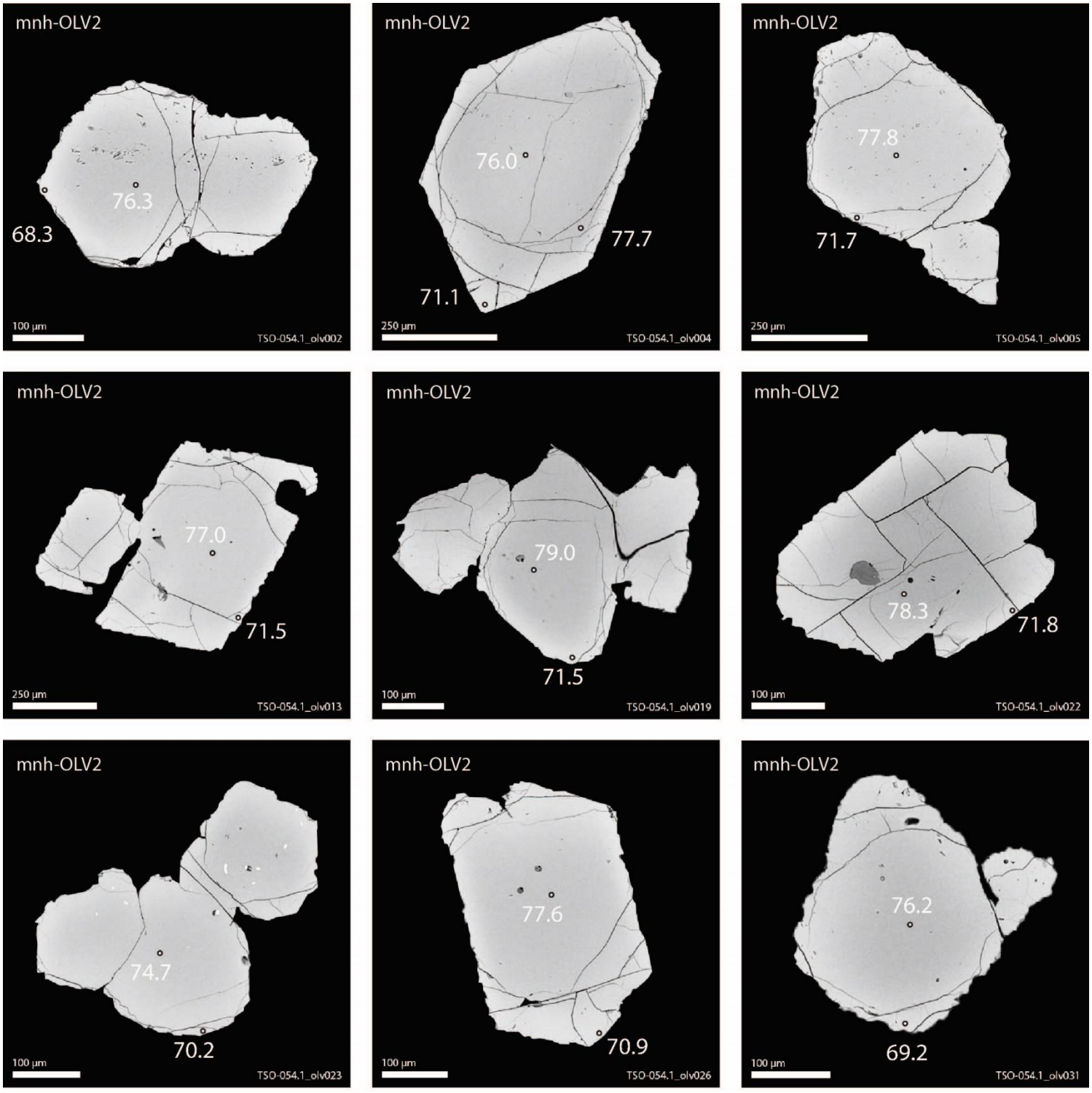

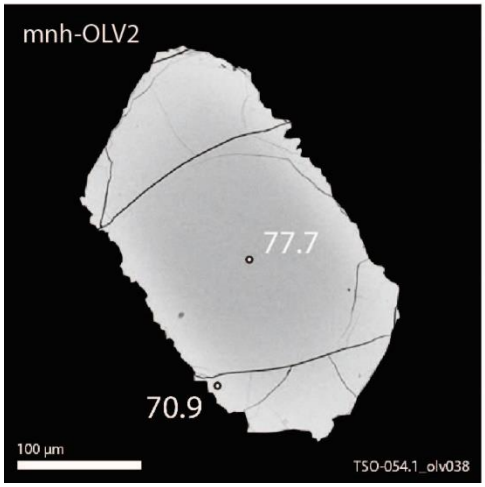
mnh-OLV2
77.7
70.9
100 µm
TSO-054.1_olv038

A5.3: Unit mtp

A5.3.1: mtp-PL1

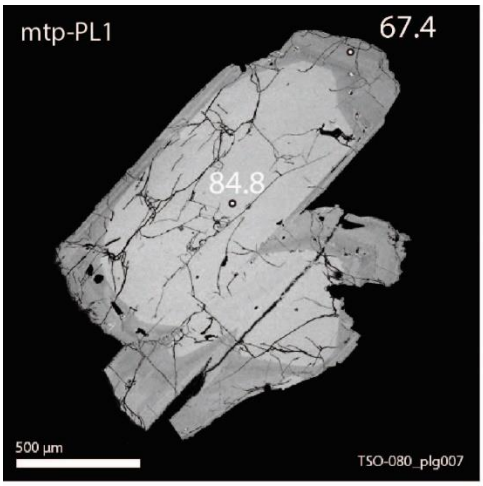

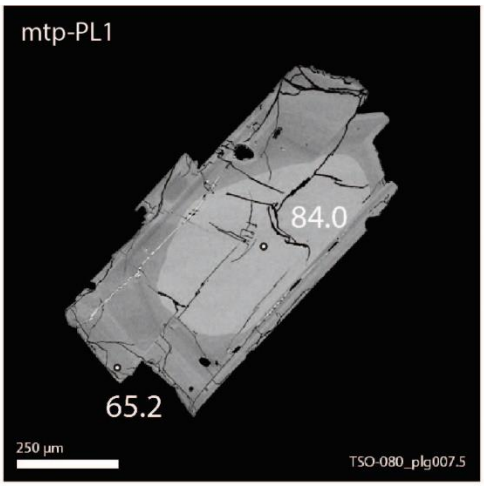

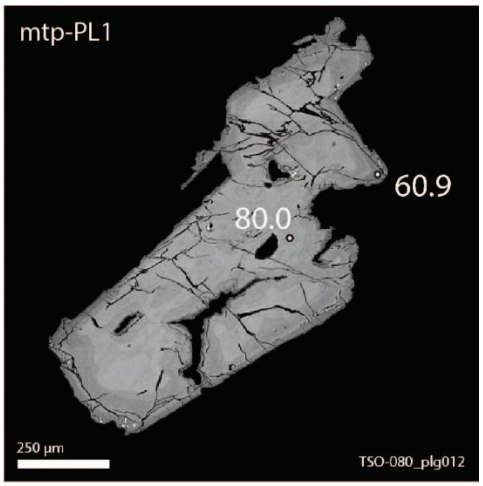

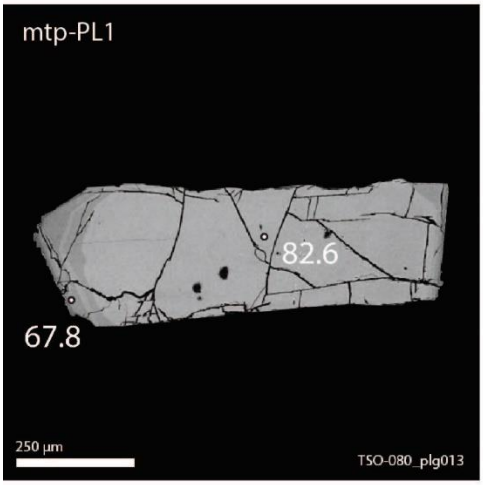

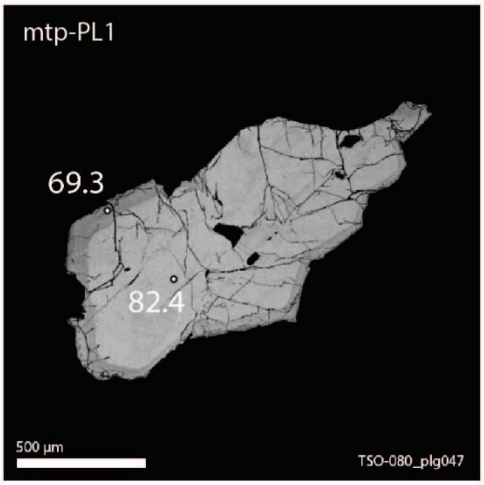

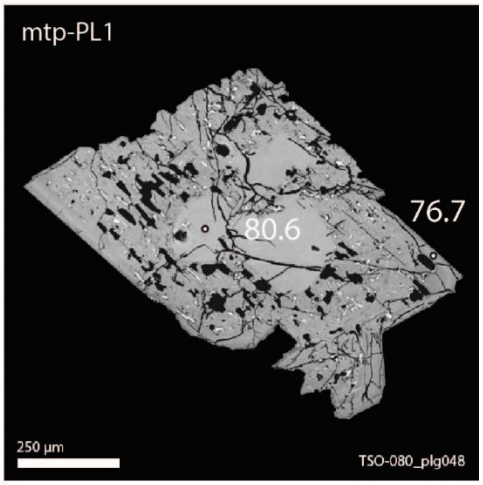

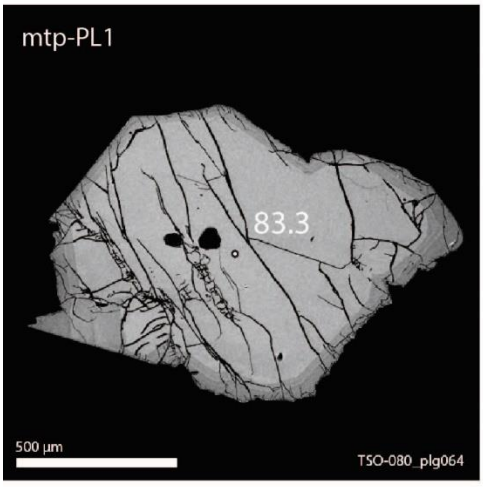

A5.3.2: mtp-PL3

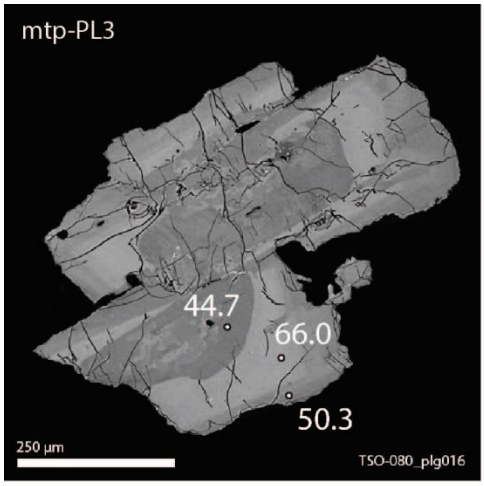
mtp-PL3
44.7
66.0
50.3
250 µm
TSO-080_plg016

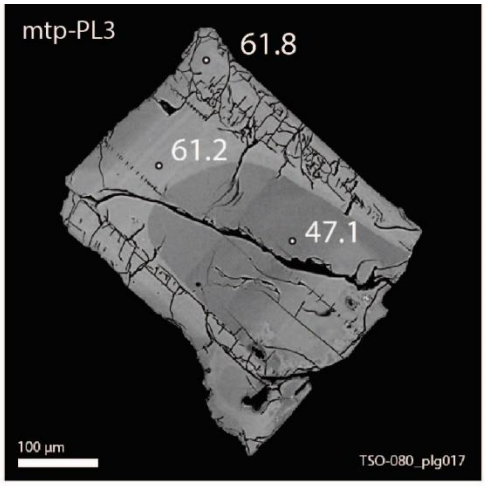
mtp-PL3
61.8
61.2
47.1
100 µm
TSO-080_plg017

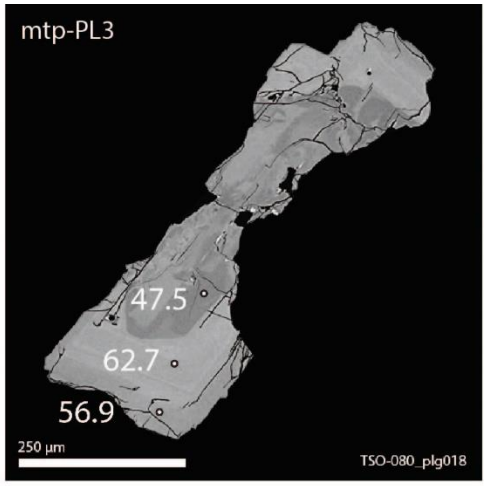
mtp-PL3
47.5
62.7
56.9
250 µm
TSO-080_plg018

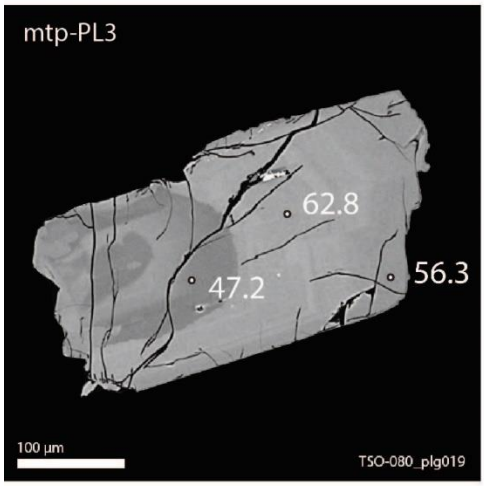
mtp-PL3
62.8
47.2
56.3
100 µm
TSO-080_plg019

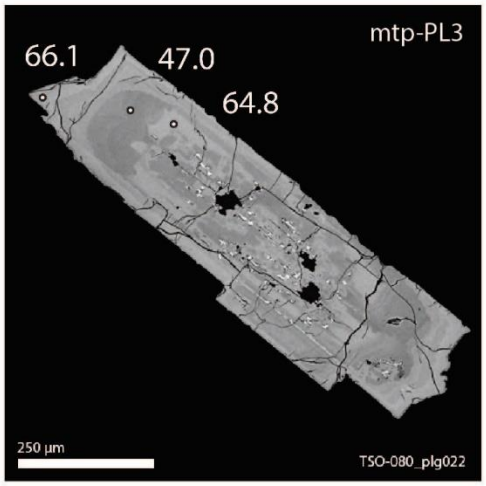
mtp-PL3
66.1
47.0
64.8
250 µm
TSO-080_plg022

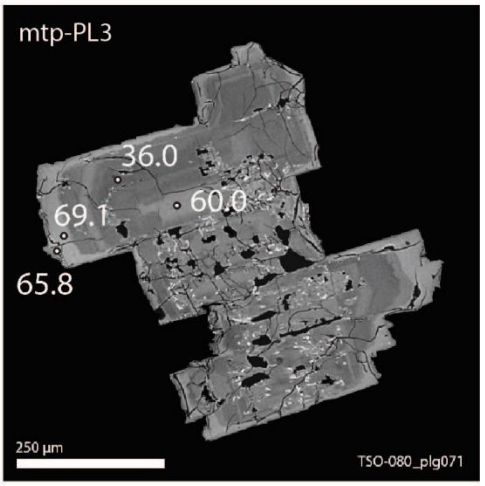
mtp-PL3
36.0
69.1
60.0
65.8
250 µm
TSO-080_plg071

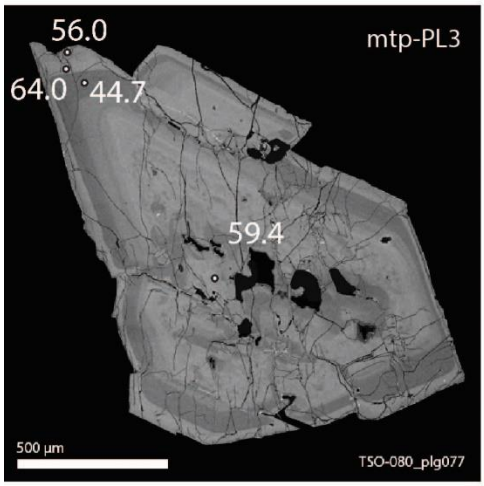
56.0
mtp-PL3
64.0
44.7
59.4
500 µm
TSO-080_plg077

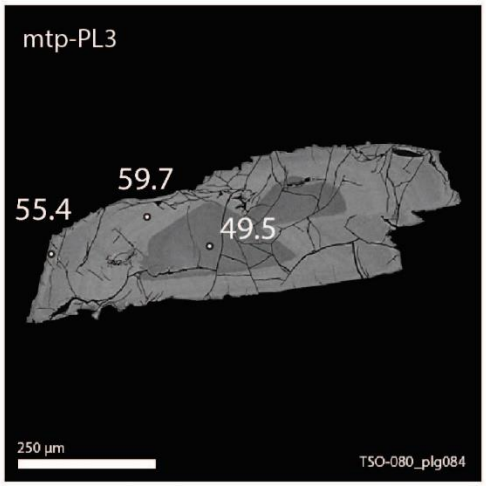
mtp-PL3
59.7
55.4
49.5
250 µm
TSO-080_plg084

A5.3.3: mtp-PL4

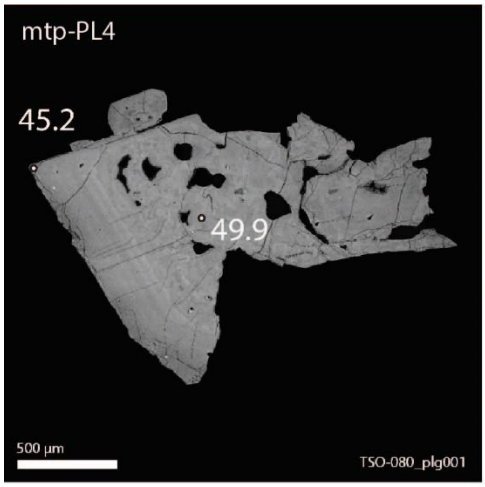
mtp-PL4
45.2
49.9
500 µm
TSO-080_plg001

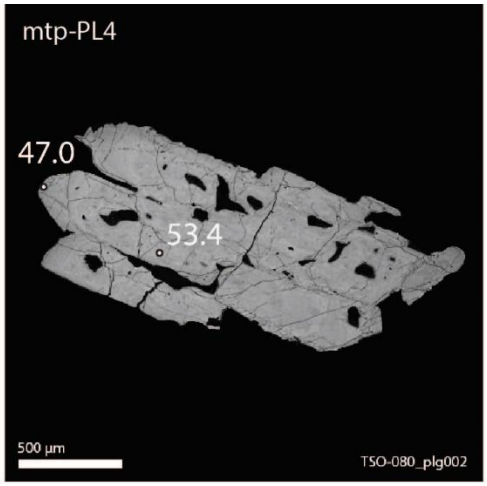
mtp-PL4
47.0
53.4
500 µm
TSO-080_plg002

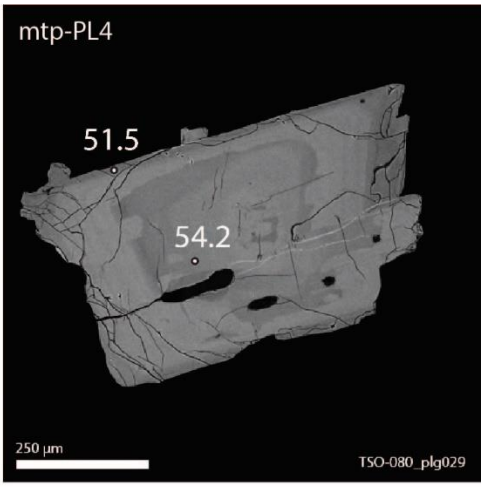
mtp-PL4
51.5
54.2
250 µm
TSO-080_plg029

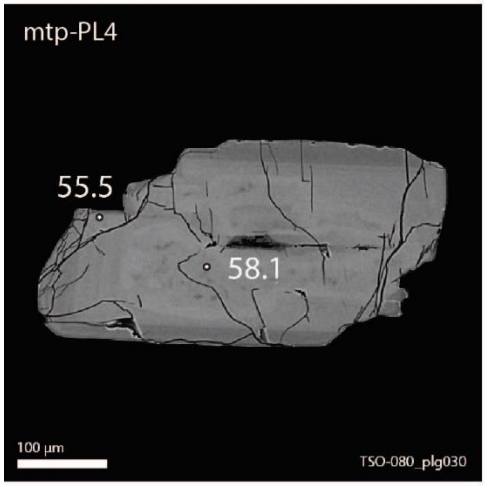
mtp-PL4
55.5
58.1
100 µm
TSO-080_plg030

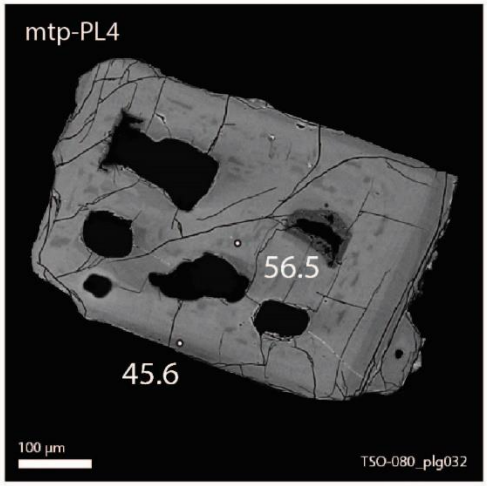
mtp-PL4
56.5
45.6
100 µm
TSO-080_plg032

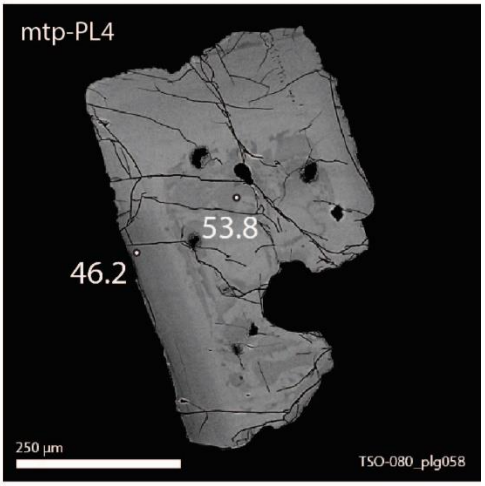
mtp-PL4
53.8
46.2
250 µm
TSO-080_plg058

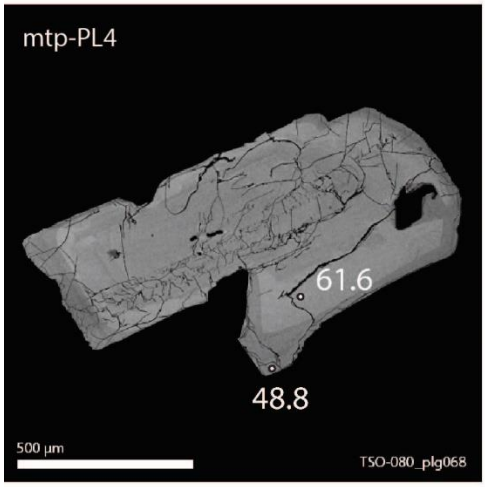
mtp-PL4
61.6
48.8
500 µm
TSO-080_plg068

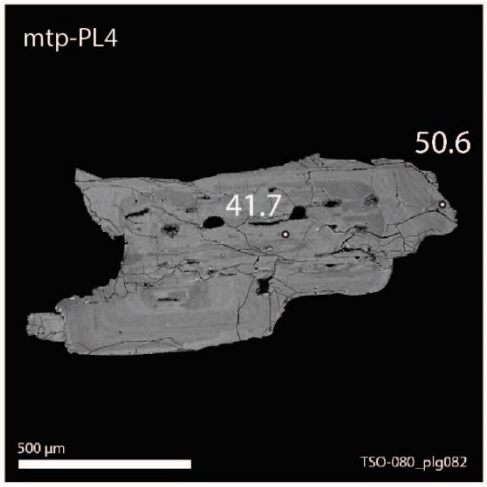
mtp-PL4
50.6
41.7
500 µm
TSO-080_plg082

A5.3.4: mtp-PL5

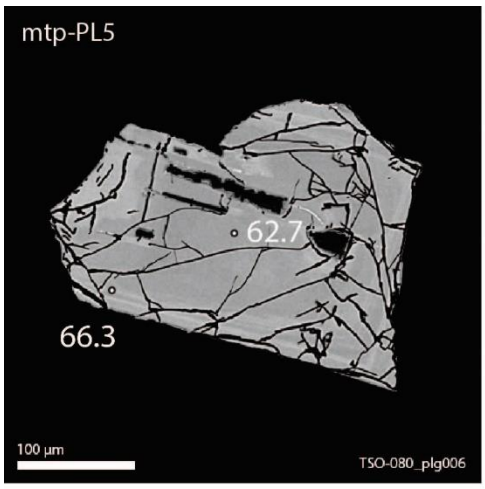
mtp-PL5
62.7
66.3
100 µm
TSO-080_plg006

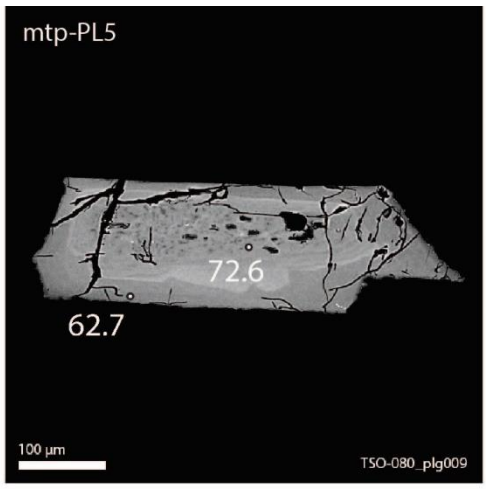
mtp-PL5
72.6
62.7
100 µm
TSO-080_plg009

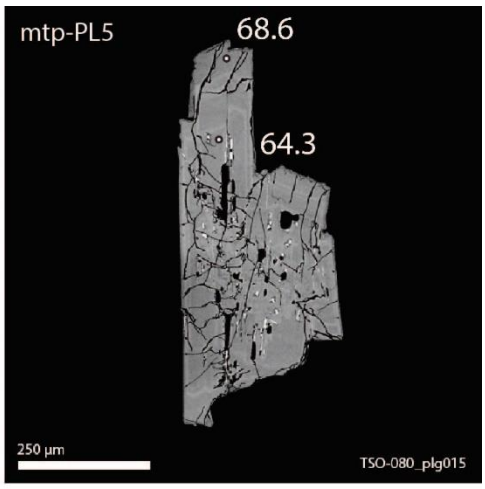
mtp-PL5
68.6
64.3
250 µm
TSO-080_plg015

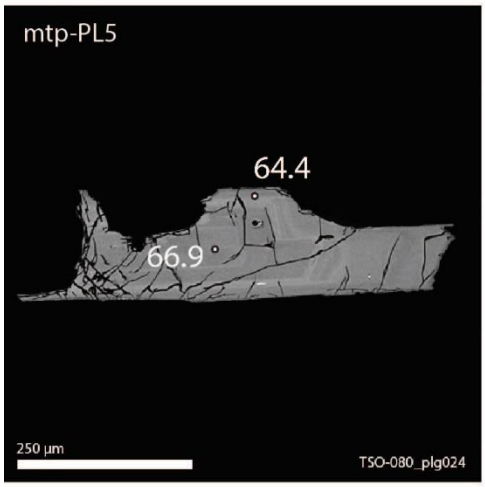
mtp-PL5
64.4
66.9
250 µm
TSO-080_plg024

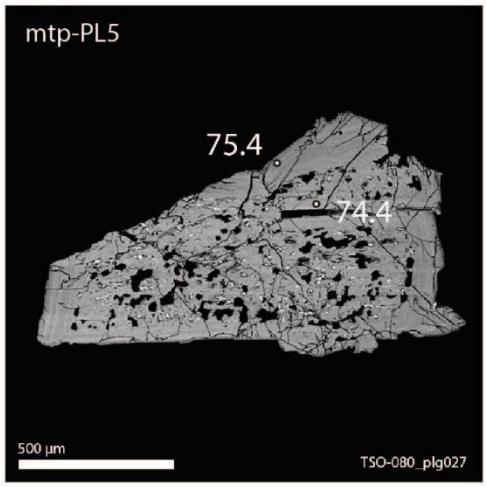
mtp-PL5
75.4
74.4
500 µm
TSO-080_plg027

A5.3.5: mtp-OLV3

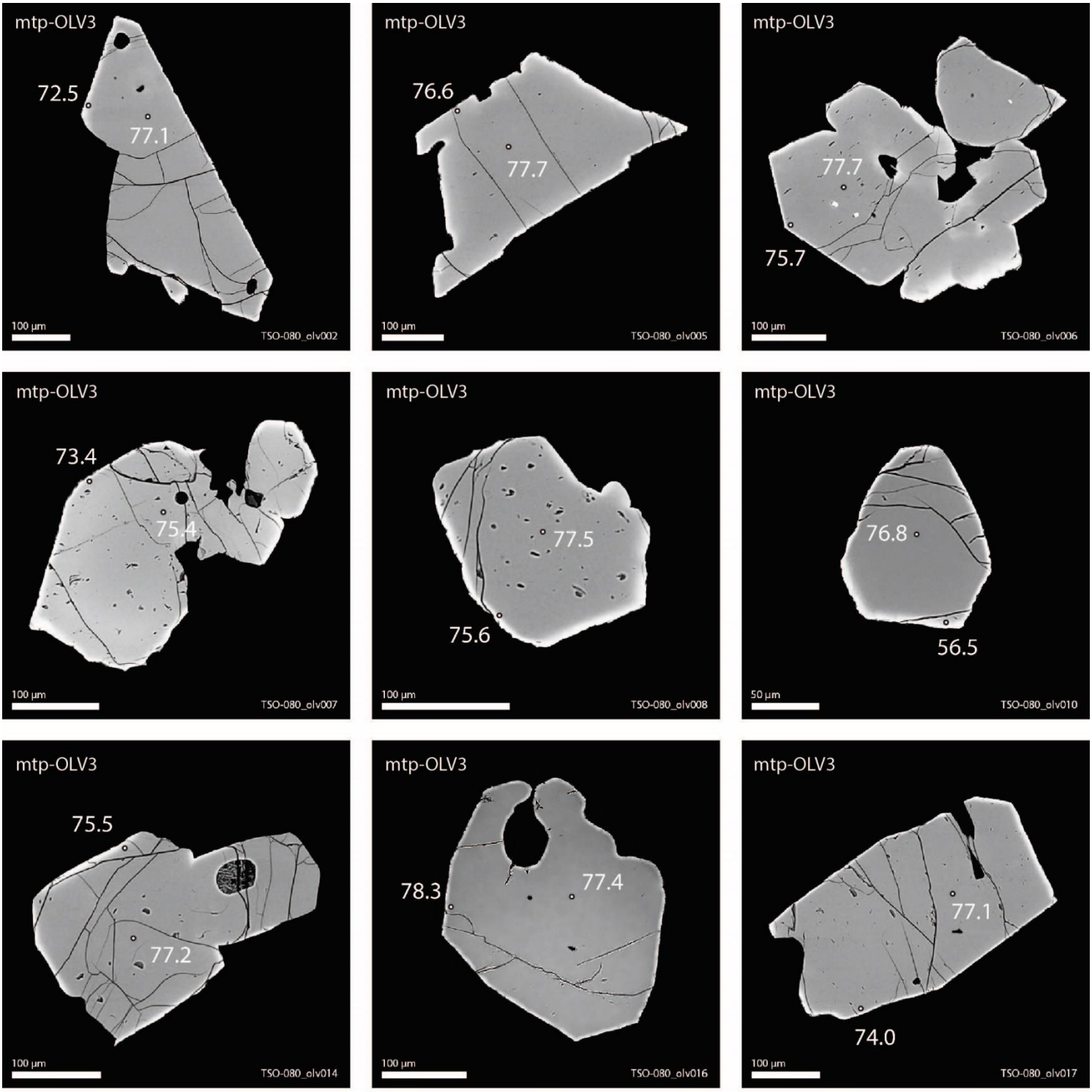

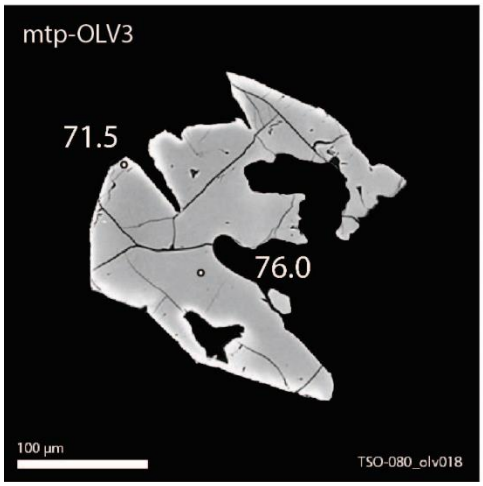
mtp-OLV3
71.5
76.0
100 µm
TSO-080_olv018

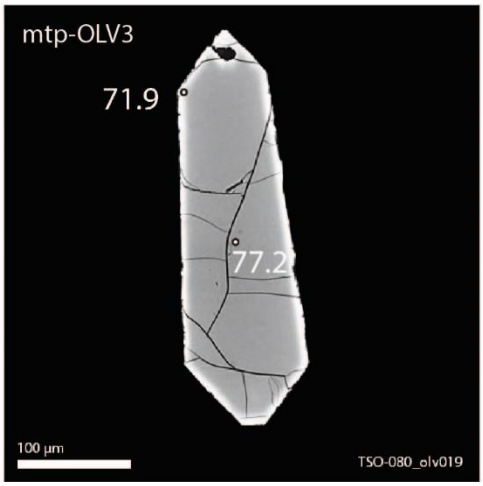
mtp-OLV3
71.9
77.2
100 µm
TSO-080_olv019

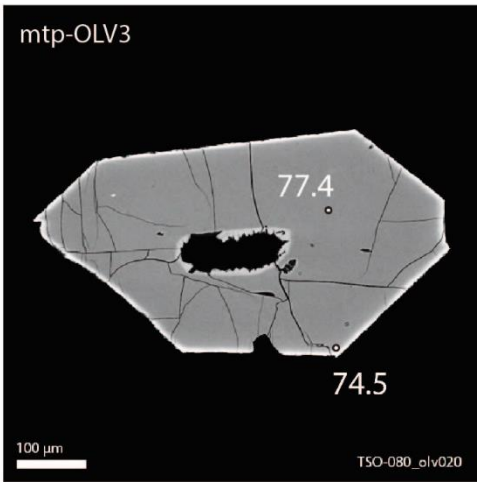
mtp-OLV3
77.4
74.5
100 µm
TSO-080_olv020

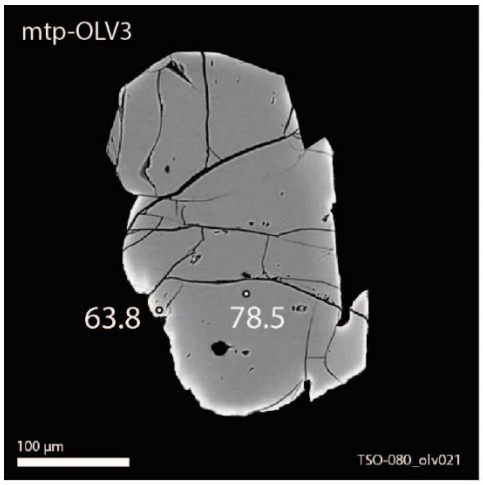
mtp-OLV3
63.8
78.5
100 µm
TSO-080_olv021

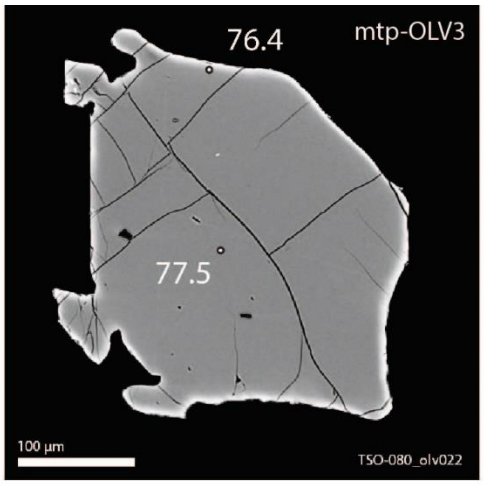
mtp-OLV3
76.4
77.5
100 µm
TSO-080_olv022

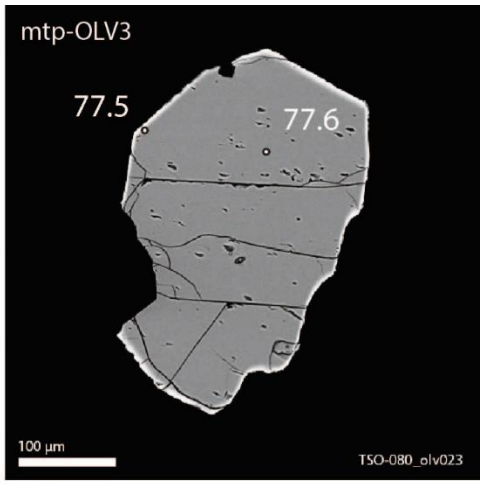
mtp-OLV3
77.5
77.6
100 µm
TSO-080_olv023

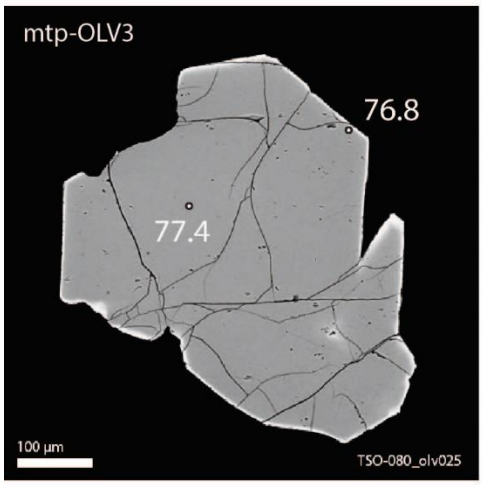
mtp-OLV3
76.8
77.4
100 µm
TSO-080_olv025

A5.3.6: mtp-OLV-MISC

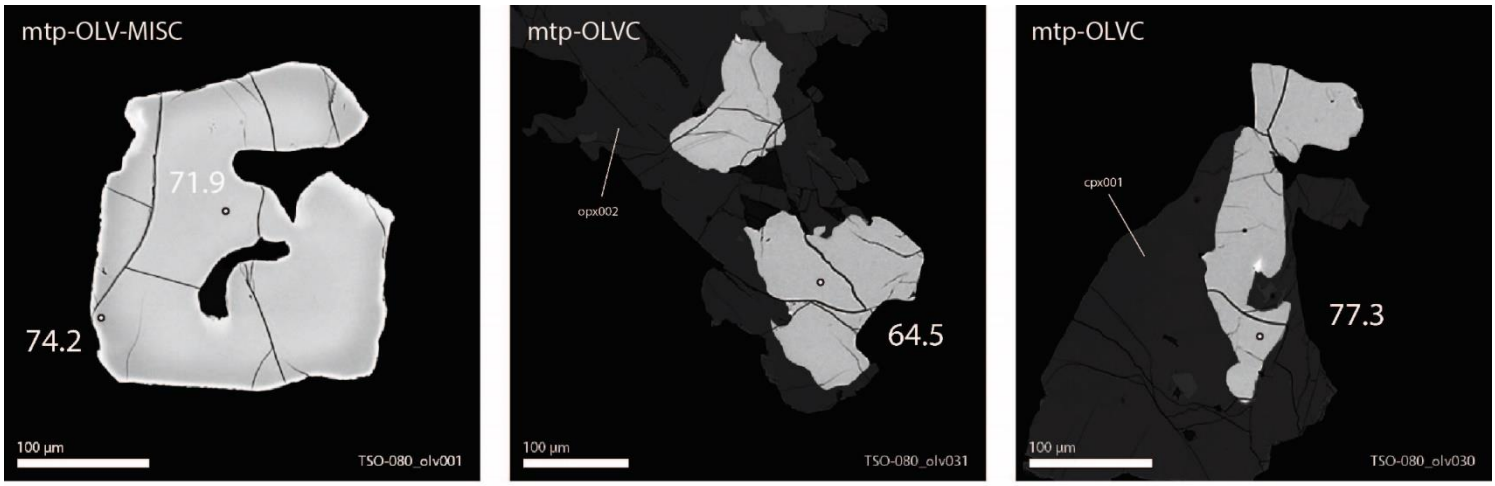

A5.3.7: mtp-OPX2

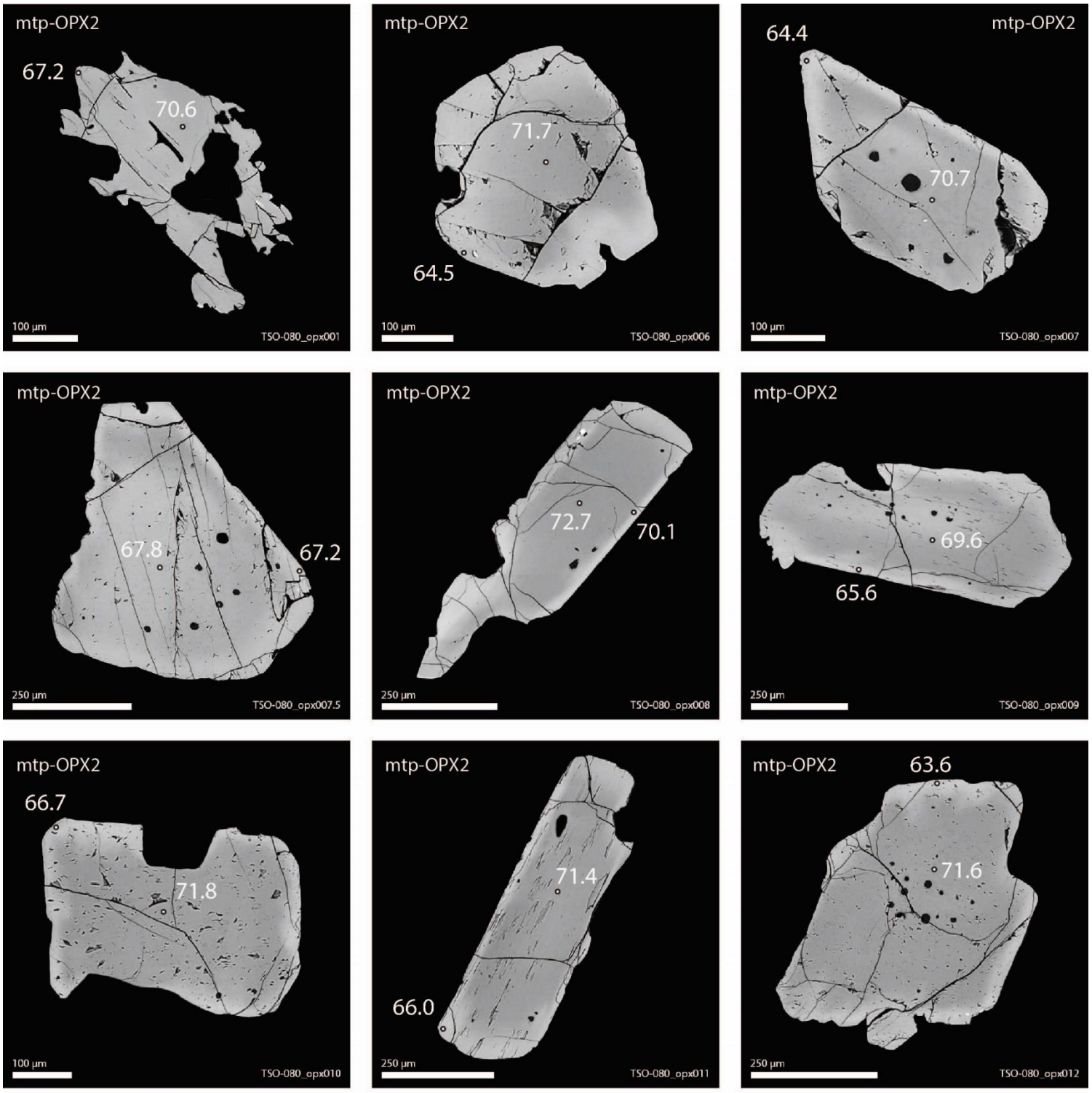

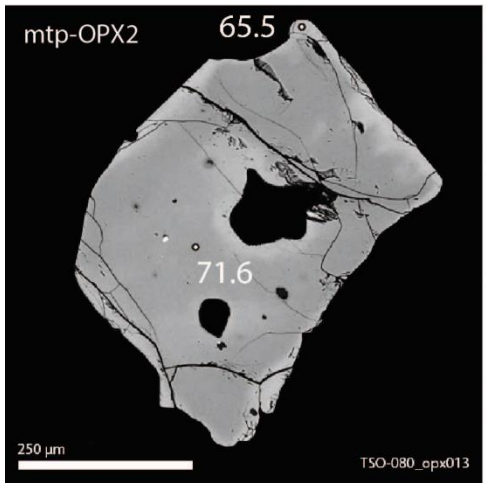
mtp-OPX2
65.5
71.6
250 µm
TSO-080_opx013

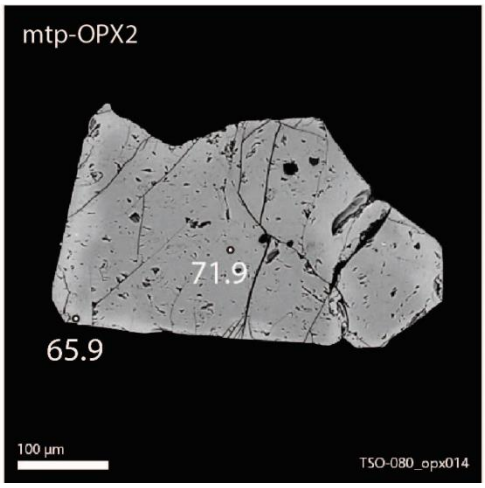
mtp-OPX2
71.9
65.9
100 µm
TSO-080_opx014

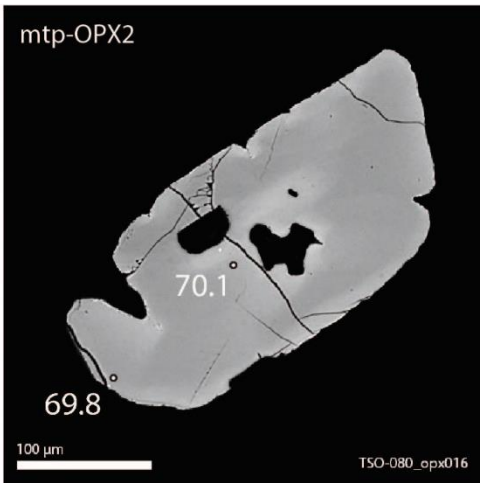
mtp-OPX2
70.1
69.8
100 µm
TSO-080_opx016

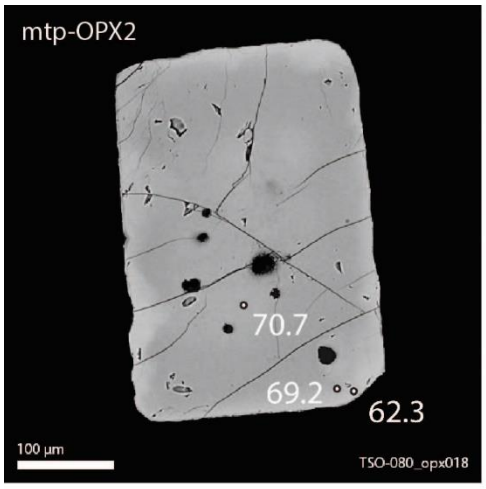
mtp-OPX2
70.7
69.2
62.3
100 µm
TSO-080_opx018

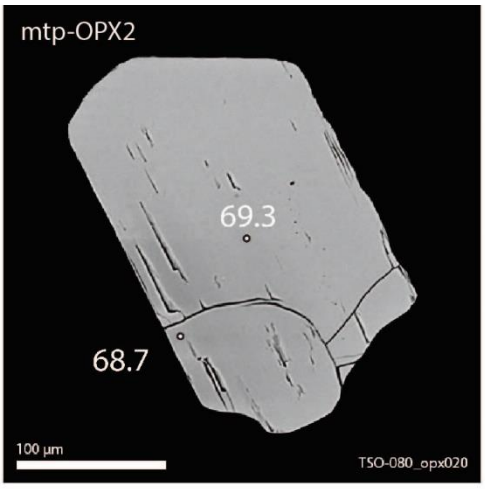
mtp-OPX2
69.3
68.7
100 µm
TSO-080_opx020

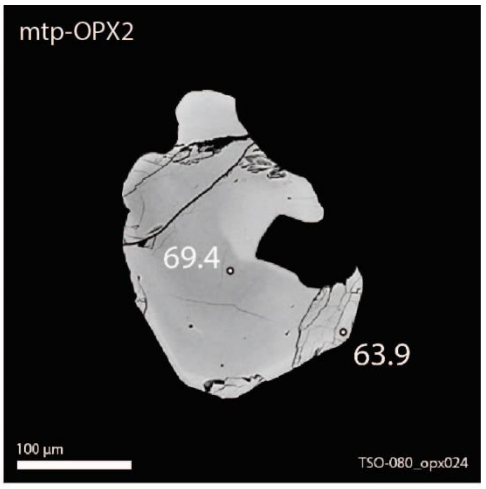
mtp-OPX2
69.4
63.9
100 µm
TSO-080_opx024

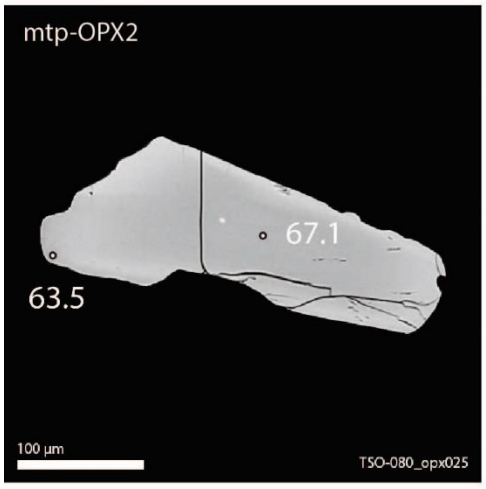
mtp-OPX2
67.1
63.5
100 µm
TSO-080_opx025

A5.3.8: mtp-OPX3

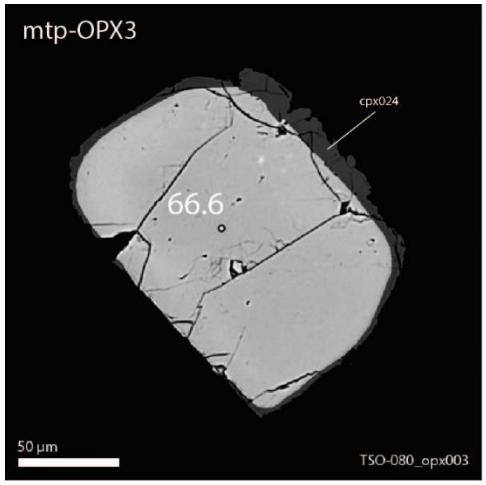

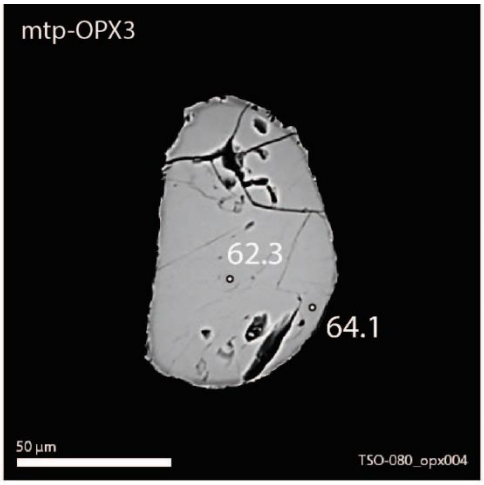

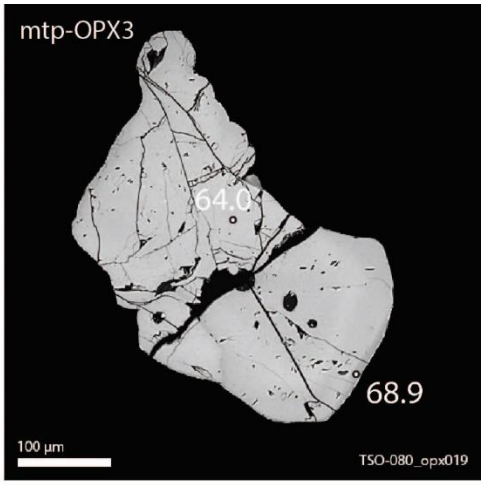

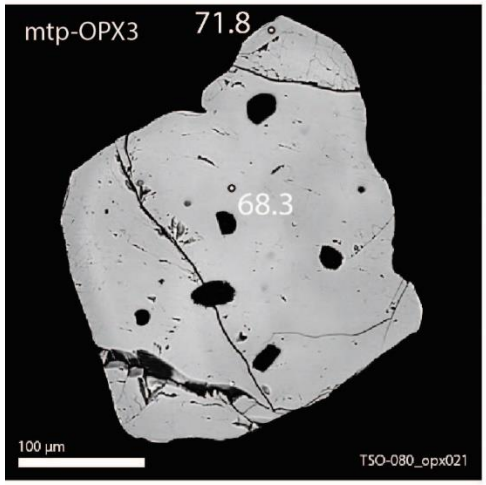

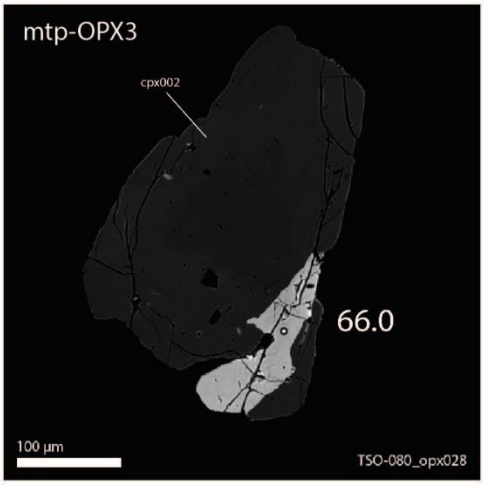

A5.3.9: mtp-CPX1

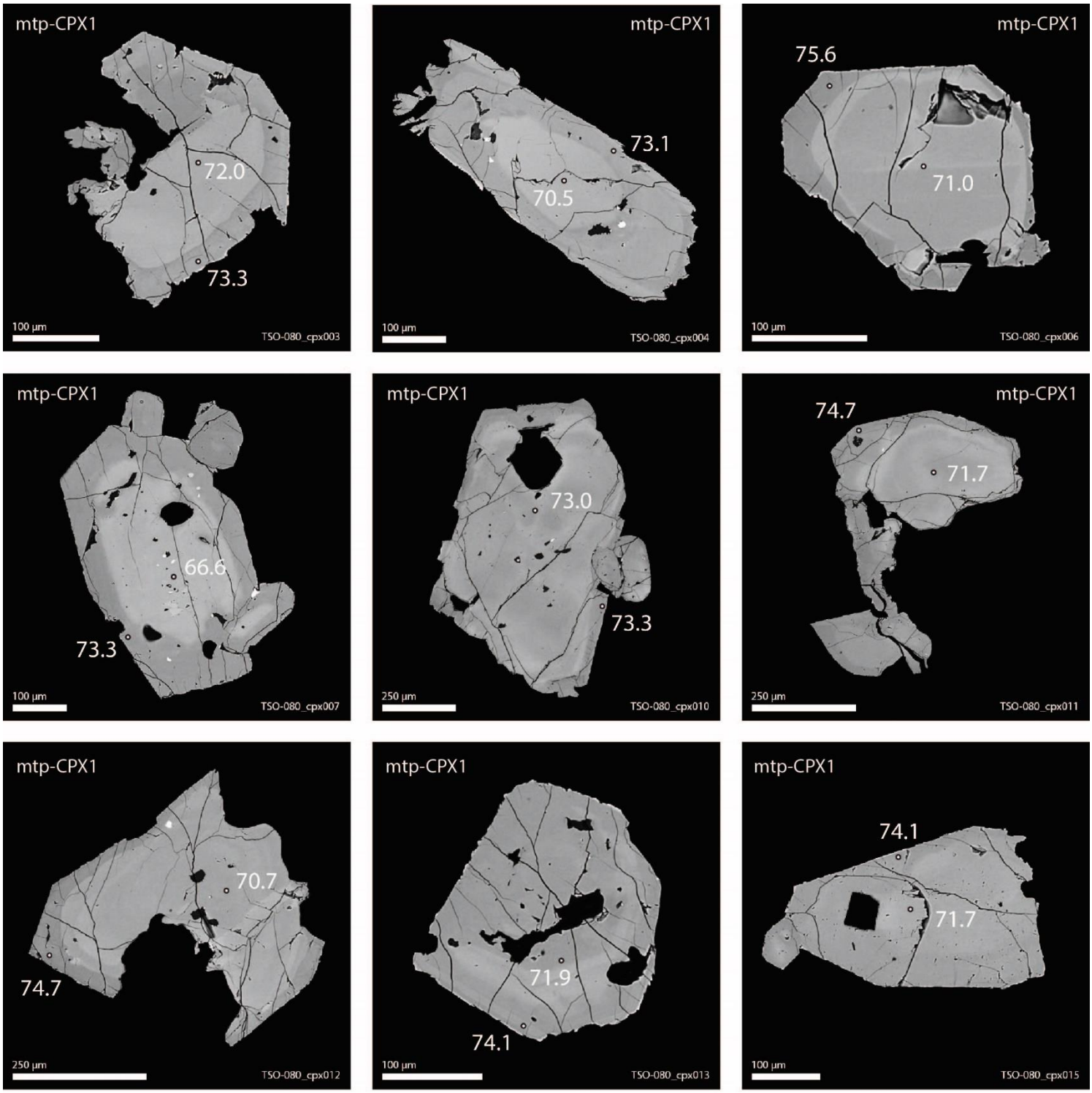

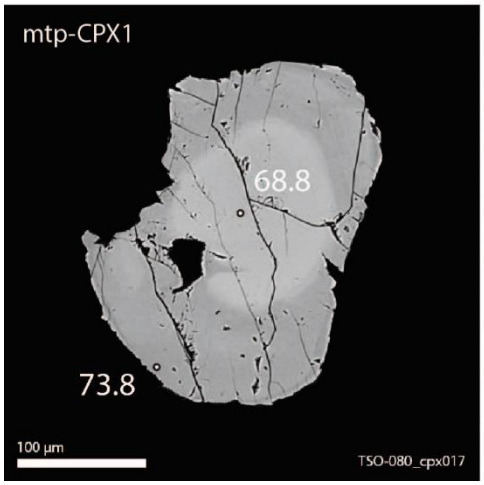
mtp-CPX1
68.8
73.8
100 µm
TSO-080_cpx017

A5.3.10: mtp-CPX2

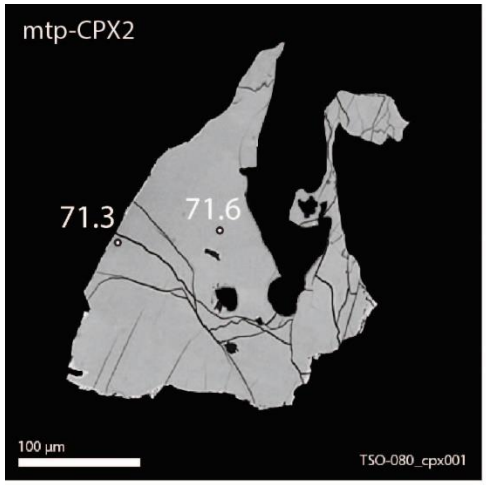

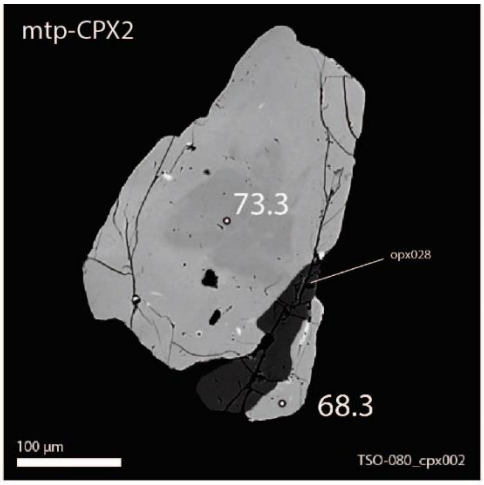

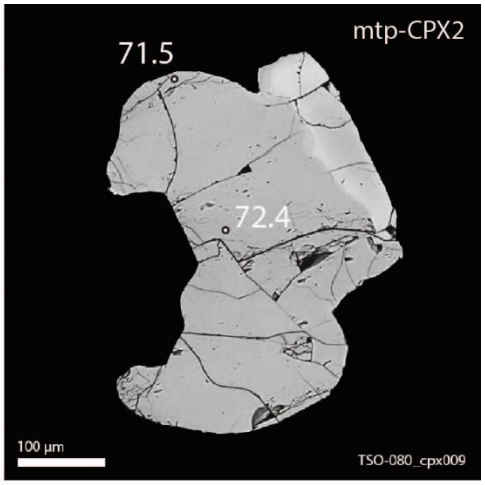

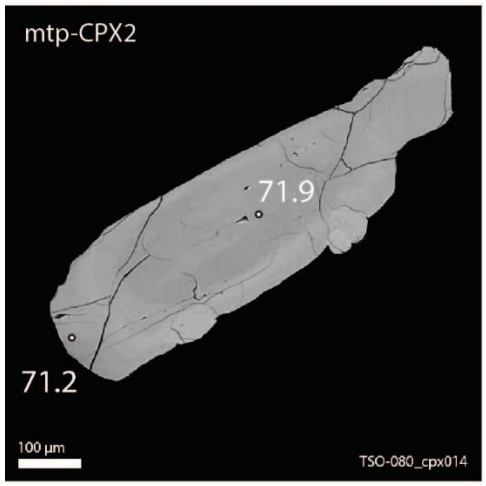

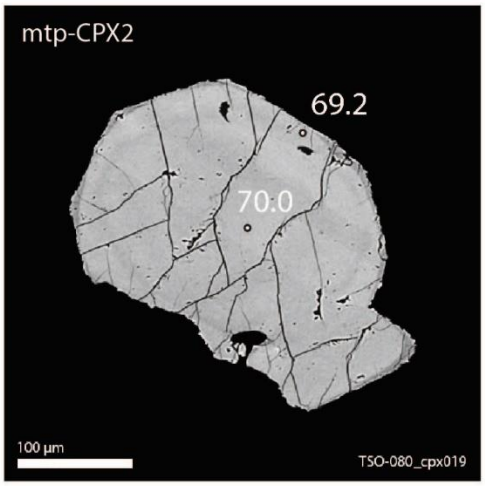

A5.3.11: mtp-CPX-MISC